Universiteit Antwerpen

Faculteit Wetenschappen

Bose-Einstein Correlations in W pair production and multi-jet Z^0 decays at LEP

Proefschrift voorgelegd tot het behalen van de graad van
Doctor in de Wetenschappen
aan de Universitaire Instelling Antwerpen
te verdedigen door

Nick van Remortel

Promotor: Prof. dr. F. Verbeure
Co-Promotor: Prof. dr. E. De Wolf

Antwerpen, 2003

Design Cover: A. Muys, Photo taken from the CERN press office database

Contents

Introduction

Since the ancient Greek philosophers, mankind has believed that all matter consists of fundamental building blocks. It was the philosopher Democritos who devised the word ‘atom’ for the smallest part of matter, derived from the word ‘atomos’, meaning undividable. He believed that the universe consisted of these atoms, travelling through infinite space, which he called the ’void’. In fact, his ideas were not very different from our current understandings. However, the notion of what these fundamental building blocks must be, has changed drastically.

A major breakthrough in this quest was achieved by D. Mendeleev in 1869 when he arranged 63 chemical elements in his periodic table, indicating that some underlying principle or symmetry should be on the basis of his classification. A few decades later it was discovered that all chemical elements consist of an atomic nucleus surrounded by electrons orbiting around it. From then on, the study of atomic nuclei and their interactions, led to the discovery of a whole new zoo of so called ‘fundamental’ particles.

Our current understanding is summarised in the impressive construct known as the Standard Model. It states that all matter is made of leptons and quarks, arranged in three families, of which the first generation builds up all stable matter. The well known electron, together with its heavier brothers, the muon and the tau, belong to the family of leptons. They are joined by the almost undetectable neutrino’s. The proton and neutron, building up the atomic nuclei are composed of quarks. All interactions between these fundamental particles are mediated by means of the so-called gauge bosons, acting as messengers of the fundamental interactions.

The electroweak interactions, unifying the electromagnetic and weak nuclear force, are mediated by four gauge bosons, the photon, the Z boson and two oppositely charged W bosons. The strong nuclear force, keeping the proton, the neutron and the nuclei together, is mediated by eight gluons.

In 1989, the LEP (Large Electron Positron) collider, a 27 km long accelerator built at the CERN laboratory in Geneva, became operational. Colliding electrons and their antimatter counterparts known as positrons, the machine was designed to test the predictions of the Standard Model to very high precision, to search for the up to now undetected Higgs boson and to study possible occurrence of phenomena ‘beyond’ the Standard Model. Along its circumference four experiments are positioned. They are known under the names ALEPH, DELPHI, L3 and OPAL.

The data collected by the DELPHI experiment was used for the work described in this thesis. In its first stage of operation, LEP was running at a centre-of-mass energy equal to the mass of the Z boson, measuring its properties precisely. From 1996 till 2000 the centre-of-mass energy was doubled, and steadily increased in order to measure the properties of the W bosons and continue the hunt for the Higgs and supersymmetric particles. Although a small indication of a Standard Model Higgs boson may have been observed, no solid proof of its existence, neither for that of supersymmetric particles was found. However, the direct searches, in combination with the precision measurement of all the essential Standard Model parameters, narrowed down the discovery domain for new experiments.

Besides the electroweak theory (and its possible extensions) much remains to be learned about the interactions between quarks and gluons, described by Quantum ChromoDynamics or QCD. In contrast with electroweak theory, QCD is not always able to provide precise predictions, especially when it comes to the understanding of how quarks, produced by the decay of either a Z or a W boson, combine themselves into stable hadrons, the particles we observe in our detectors.

The measurement of Bose-Einstein Correlations (BEC) at LEP, the subject of this work, is relevant to both the electroweak and to the QCD aspect of particle production. A fundamental property of particles known as spin (intuitively understandable as the intrinsic angular momentum) tells us how we should count the number of particles being in a given state. Being a pure quantum-mechanical effect, bosons (particles with integer spin) tend to accumulate together in the same state, while Fermions (particles with half integer spin) can not. In high energy collisions this translates in an alignment of bosons in energy-momentum space.

The measurement of particle coincidence spectra by means of correlation functions, a technique borrowed from astronomy, can probe the space-time structure of the production region of hadrons. Hence, phenomenological models describing the mechanism behind hadron production can be tested. This is the first, QCD based, interest of studying Bose-Einstein correlations in high energy interactions.

Bose-Einstein correlation effects are also relevant to electroweak physics for the following reason. Due to the short life-time of the W boson, compared to the time needed to combine quarks into hadrons, it is possible that the decay products of different W's in the reaction $e^+e^- \rightarrow W^+W^-$ are subjected to Bose-Einstein symmetrisation. Hence, the assumption that the two W bosons decay independently could be wrong. This leads to a systematic uncertainty in the direct reconstruction of the W mass, if the assumption of independent decay is made. The measurement of Bose-Einstein correlations between decay products from the two fragmenting W bosons inside fully hadronic WW decays, will help us to evaluate the size of the systematic uncertainty on the W mass measurement. Evidence for inter-W BEC would contradict many hadronisation models, in which it is normally assumed that “cross-talk” between two decaying W's is absent.

The structure of this thesis is as follows. In chapter 1 the use of Bose-Einstein statistics as an interferometric technique is explained, by means of semi-classical and quantum mechanical arguments. An overview of correlation function measurements in various interactions and for various particle species is given.

Since the recombination of quarks into hadrons cannot be calculated using perturbative QCD, phenomenological models are used to describe this phenomenon, generally in the framework of Monte Carlo programs. The general ideas behind these models, and more precisely the Lund string model, are explained in chapter 2. It will be shown here that, paradoxically, nearly all of these hadronisation models consider particle production as a coherent mechanism, which would, according to chapter 1, not allow for Bose-Einstein correlations.

The experimental setup, describing the various sub-detectors of the DELPHI experiment is discussed in chapter 3.

The measurement of inter-W Bose-Einstein correlations is explained in detail in chapter 4. The technique is based on the comparison of fully hadronic WW decays with an artificially constructed "reference" sample, combining two hadronic W decays from different events.

Chapter 5 presents a study of another system where, according to the Lund model, two systems decay quasi independently. It concerns decays of the Z boson into two quarks, where one of the quarks radiates a hard gluon, thus resulting in an event topology characterised by three jets. We end with a summary and interpretation of all obtained results.

Chapter 1

Bose-Einstein Correlations

In this chapter, some basic aspects of interferometry are discussed. After a brief section, defining particle densities and correlation functions, the coincidence measurement of detecting two particles is explained using both semi-classical arguments and quantum optics. It will be demonstrated in both cases that an intensity interference pattern will only arise if the particle source is chaotic. A discussion of the so-called reference sample problem is given, together with a brief review of correlation function measurements in various interactions and for various boson species.

1.1 Quantum statistics

The counting procedures of classical statistical mechanics need modifications when quantum effects are important. Since 1926 we know that there are actually two new ways of counting, Bose-Einstein statistics and Fermi-Dirac statistics [1]. The key to this lies in permutation symmetries of many-particle wave functions. In 1924 Bose was able to prove Planck's blackbody radiation law, assuming that light-quanta are indistinguishable. Later that year, Einstein applied Bose's methods on an ideal mono-atomic gas and found deviations from the classical ideal gas law, thus leading to the origin of the term Bose-Einstein statistics. Yet, both were not aware at that time of a Schrödinger wave function, which was only introduced a year later. Fermi was the first to connect the indistinguishability of particles with Pauli's exclusion principle when treating a gas of helium atoms. Later in 1926 Dirac and Heisenberg concluded that symmetric eigenfunctions must be connected with light quanta, while antisymmetric eigenfunctions are related to electrons.

Although the relationship between Bose-Einstein (Fermi-Dirac) statistics and symmetric (anti-symmetric) wave functions is quite simple, the link between spin and the symmetry of the wave functions is not. This is explained by the spin-statistics or CPT theorem, proved by Pauli in 1940 [2] and generalised by Burgoyne and Jost [3, 4] in the late 1950's. The CPT theorem (nature's invariance under particle-antiparticle, right-left and past-future applied simultaneously) is one of the most profound bases of Quantum Mechanics. It is the minimal sufficient ground for the existence of anti-particles to particles and for the equalities of masses and lifetimes for these pairs of objects. Therefore let us assume further that, as a rule, wave functions for bosons (particles with integer spin) and fermions (particles with half-integer spin) must be symmetric, respectively anti-symmetric under particle permutations.

1.1.1 Inclusive particle densities and correlation functions

The study of particle correlations finds its origin in statistical physics, describing the behaviour of non-ideal gases and liquids. The formalism developed in this field was adopted by particle physics in order to describe interactions leading to a many-particle final state [5].

In this work we will consider collisions between two particles[1], an electron and a positron (e^+e^-), yielding n particles in a sub-volume Ω of the total phase space. The distribution of points in this sub-domain Ω can be characterised by the so-called exclusive particle densities $P_n(y_1, ..., y_n)$, where $n = 1, 2, ..., n_{tot}$ with n_{tot} the total number of particles produced in the reaction. The symbol y denotes the set of kinematical variables needed to specify the position of each particle in the phase space. These densities are called *exclusive* because they correspond to the distribution of particles in Ω, where the total multiplicity n_{tot} is exactly n.

Inclusive densities describe the distribution of n points in Ω, irrespective of the presence of any further points. They are related to the exclusive densities by the following relation:

$$\rho_n(y_1, ...y_n) = P_n(y_1, ...y_n) + \sum_{m=1}^{\infty} \frac{1}{m!} \int_{\Omega} P_{n+m}(y_1, ..., y_n, y'_1, ...y'_m) \prod_{i=1}^{m} dy'_i. \tag{1.1}$$

In most experimental studies, the properties of inclusive particle densities are investigated. The n-particle inclusive density $\rho_n(y_1, ..., y_n)$ is defined as

$$\rho_n(y_1, ..., y_n) = \frac{1}{\sigma_t} \frac{d^n\sigma}{dy_1...dy_n}, \tag{1.2}$$

with σ_t the total cross-section of the considered reaction. Experimentally, this quantity is approximated by

$$\rho_n(y_1, ..., y_n) = \frac{1}{n!N_{evt}} \frac{dN^{n-tuples}}{dy_1...dy_n}, \tag{1.3}$$

with N_{evt} the total number of events in the collected sample and $dN^{n-tuples}$ the number of n-tuples of particles (a particle, a pair of particles, a triplet of particles, etc.) counted in a phase space domain $(y_1 + dy_1, ..., y_n + dy_n)$. Integration over the phase space interval Ω yields

$$\int_{\Omega} \rho_1(y)dy = \langle n \rangle, \tag{1.4}$$

$$\int_{\Omega} \int_{\Omega} \rho_2(y_1, y_2)dy_1dy_2 = \langle n(n - \delta_{12}) \rangle, \tag{1.5}$$

where $\delta_{12} = 0$ for different hadrons and $\delta_{12} = 1$ for identical hadrons coming from the same event. The integral in Eq. 1.4 is nothing more than the average number of produced particles, or the average multiplicity, while Eq. 1.5 defines the second-order factorial moment of the multiplicity distribution. It is straightforward to extend the definitions up to arbitrary orders.

At this point we introduce the concept of correlation functions, a very useful quantity in the study of stochastic processes of interacting particles.

[1] In particle physics, these are often called "events".

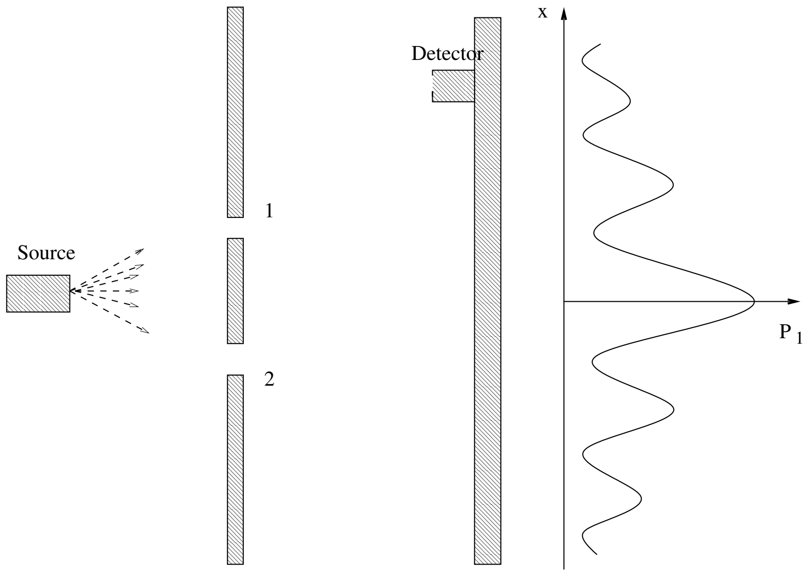

Figure 1.1: Young's two slit experiment, resulting in an interference pattern.

Correlation functions

Inclusive n-particle densities contain in general trivial contributions from lower-order densities. It is therefore more advantageous to define a new set of functions $C_n(y_1, ..., y_n)$ as those quantities which vanish whenever one of the arguments becomes statistically independent of the others. These new functions are called factorial cumulant correlation functions and are defined as

$$C_1(y) = \rho_1(y); \tag{1.6}$$

$$C_2(y_1, y_2) = \rho_2(y_1, y_2) - \rho_1(y_1)\rho_1(y_2); \tag{1.7}$$

$$C_3(y_1, y_2, y_3) = \rho_3(y_1, y_2, y_3) - \sum_{(3)} \rho_1(y_1)\rho_2(y_2, y_3) + 2\rho_1(y_1)\rho_1(y_2)\rho_1(y_3). \tag{1.8}$$

The work in this thesis studies Bose-Einstein correlations between two particles only. Therefore we will restrict ourselves further to correlation functions of order two.

The second-order correlation functions can be normalised by dividing them with the single-particle inclusive densities at y_1 and y_2, respectively:

$$\frac{C_2(y_1, y_2)}{\rho_1(y_1)\rho_1(y_2)} = \frac{\rho_2(y_1, y_2)}{\rho_1(y_1)\rho_1(y_2)} - 1 = R_2(y_1, y_2) - 1. \tag{1.9}$$

This defines the two-particle normalised density $R_2(y_1, y_2)$, or normalised density for short.

Most studies of two-particle correlations consist in analysing $R_2(y_1, y_2)$ where the key issue of any analysis lies in the choice of the normalisation factor $\rho_1(y_1)\rho_1(y_2)$. For a short overview we refer to Sect. 1.2.

In what follows, Bose-Einstein correlations between two identical bosons (pions, in practice) will be discussed. It will be shown that it originates form pure quantum mechanical

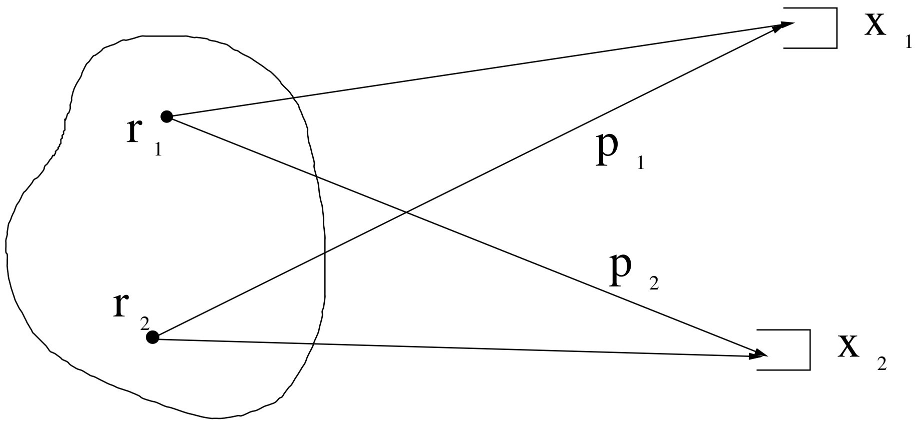

Figure 1.2: Coincidence of detection of two indistinguishable particles.

considerations and that it is used as a tool to investigate the space-time properties of the particle production source.

1.1.2 Quantum interference

The well known two slit experiment by Young (see Fig. 1.1) shows that one obtains an interference pattern when one calculates the probability of observing one particle in a detector when it was either produced in a point r_1 or in a point r_2 in space. Let us denote the particle wave when it is produced in r_1 by

$$\psi_{r_1} = f_1 e^{ipr_1}, \tag{1.10}$$

and the wave when it is produced in point r_2 by

$$\psi_{r_1} = f_2 e^{ipr_2}. \tag{1.11}$$

In both equations f_1 and f_2 represent two real amplitudes. The probability of observing a particle at point x is then given by

$$P(x) = |f_1 e^{ipr_1} + f_2 e^{ipr_1}|^2 = f_1^2 + f_2^2 + 2 f_1 f_2 \cos\left(p(r_1 - r_2)\right) \neq |\psi_{r_1}|^2 + |\psi_{r_2}|^2. \tag{1.12}$$

This is valid independently of the particle type, and bears no relationship with Bose-Einstein or Fermi-Dirac statistics (it is valid for a beam of light or an electron gun).

One can go one step further and ask for the probability of observing two particles of the same species, coming from 2 production points r_1, r_2 in space, in 2 detectors at position x_1 and x_2 [6]. This is sketched in Fig. 1.2. At this stage it is useful to consider the two-particle normalised density:

$$R_2 = \frac{P(p_1, p_2)}{P(p_1)P(p_2)}, \tag{1.13}$$

where in the case of bosons $P(p_1, p_2)$ is the two-particle density[2], subject to Bose-Einstein symmetrisation and $P(p_i)$ is the corresponding single particle density for a particle with four-momentum p_i. In practice $P(p_1)P(p_2)$ is often replaced by $P_0(p_1, p_2)$, which is constructed in such a way as to represent $P(p_1, p_2)$ in all respects, except for the Bose-Einstein symmetrisation. As such, R_2 quantifies the enhanced probability for emission of two identical bosons when these are close in momentum-space.

In the case where bosons are distributed in space according to a given space-time density [3], $\rho(r)$, the two-particle densities are given by:

$$P(p_1, p_2) = \int |\Psi_{12}^{BE}(x_1x_2; r_1r_2)|^2 \rho(r_1)\rho(r_2) d^4r_1 d^4r_2, \tag{1.14}$$

$$P_0(p_1, p_2) = \int |\Psi_{12}^{noBE}(x_1x_2; r_1r_2)|^2 \rho(r_1)\rho(r_2) d^4r_1 d^4r_2, \tag{1.15}$$

where the integral extends over the full emission volume. Assuming completely incoherent emission of two identical bosons, $\Psi_{12}^{BE}(x_1x_2; r_1r_2)$ is given by

$$\Psi_{12}^{BE}(x_1x_2; r_1r_2) = \frac{1}{\sqrt{2}}(e^{ip_1(x_1-r_1)}e^{ip_2(x_2-r_2)} + e^{ip_1(x_1-r_2)}e^{ip_2(x_2-r_1)}), \tag{1.16}$$

while the squared amplitude in the absence of Bose-Einstein symmetrisation is given by:

$$|\Psi_{12}^{noBE}(x_1x_2; r_1r_2)|^2 = 1/2(|e^{ip_1(x_1-r_1)}e^{ip_2(x_2-r_2)}|^2 + |e^{ip_1(x_1-r_2)}e^{ip_2(x_2-r_1)}|^2). \tag{1.17}$$

This results in a normalised density of the form:

$$R_2 = 1 + |G_{12}|^2, \tag{1.18}$$

where G_{12} is the Fourier transform of $\rho(r)$:

$$G_{12} = \int e^{iQr}\rho(r) \quad d^4r, \tag{1.19}$$

and $Q = p_1 - p_2$, the difference in four-momentum of the particles 1 and 2. If one assumes a Gaussian space-time density for the particle production points

$$\rho(r) = \frac{1}{4\pi^2 R^4} e^{-r^2/2R^2}, \tag{1.20}$$

where R denotes the radius of the source, one obtains

$$R_2 = 1 + e^{-Q^2R^2}, \tag{1.21}$$

which is independent of the positions x_1 and x_2 of the detectors.

It is very important to notice that as soon as we have a completely coherent source, the enhancement will disappear. Let us introduce two complex amplitudes f_1 and f_2 for the two

[2]In this simple case, the inclusive and exclusive two-particle densities coincide.

[3], not to be confused with the inclusive phase-space densities defined in the previous section.

superimposed waves. The most general symmetric wave function for the two particles will have the form:

$$\Psi_{12}^{BE} \sim (f_1 e^{ip_1(x-r_1)} + f_2 e^{ip_1(x-r_2)})(f_1 e^{ip_2(x-r_1)} + f_2 e^{ip_2(x-r_2)}). \tag{1.22}$$

If the two sources are coherent, then the average over the phases $\langle f_1 f_2^* \rangle \neq 0$ and the average squared amplitude becomes identical to the squared amplitude of the reference sample:

$$\langle |\Psi_{12}^{BE}|^2 \rangle = \langle |\Psi(1)|^2 \rangle \langle |\Psi(2)|^2 \rangle, \tag{1.23}$$

resulting in a constant R_2. For a purely chaotic source, f_1 and f_2 fluctuate randomly such that $\langle f_1 f_2^* \rangle = 0$, resulting in

$$\langle |\Psi_{12}^{BE}|^2 \rangle \sim (\langle f_1^2 \rangle + \langle f_2^2 \rangle)^2 + 2\langle f_1^2 \rangle \langle f_2^2 \rangle \cos(Q\Delta R), \tag{1.24}$$

with $\Delta R = |r_1 - r_2|$, whereas

$$\langle |\Psi(1)|^2 \rangle \cdot \langle |\Psi(2)|^2 \rangle = (\langle f_1^2 \rangle + \langle f_2^2 \rangle)^2. \tag{1.25}$$

In reality , the source can have any degree of coherence. It is, therefore, common practice to add a multiplicative factor λ in Eq. 1.18

$$R_2 = 1 + \lambda |G_{12}|^2, \tag{1.26}$$

where a value $\lambda = 0$ indicates a completely coherent source, and a value $\lambda = 1$ a completely chaotic source [4]. In experimental situations the value of λ is further decreased due to misidentification of particles, secondaries, etc.

It should be clear for the reader that Young's experiment was showing an amplitude interference. A two-particle correlation function tells us something about intensity correlations. The whole formalism [7] can be generalised to any arbitrary order, but is further of no relevance to this thesis.

1.1.3 Quantum interferometry

The formalism of second order interference described above can in practice be applied to concrete experimental situations, both on a macroscopic and a microscopic level. It was introduced as a successful tool in astronomy in the 1950's by Hanbury Brown and Twiss (HBT) [8] in order to measure stellar diameters, with short baseline telescopes.

In particle physics, the effect was first observed in 1959 when Goldhaber et al. [9] studied low energy proton-antiproton collisions in search of the ρ-meson. In their study of angular differences between pion pairs, they observed that like-sign charge pairs were having a higher probability to be closer together than unlike-sign pairs. The explanation was only given a year later [10] by Goldhaber, Goldhaber, Lee and Pais, using the formalism (with some small modifications) as described in previous section. The semi-classical plane wave interpretation of the Bose-Einstein effect in multi-particle production is therefore known as

[4] For only two sources, the maximim value of λ is 1/2, which saturates to unity for infinite amount of source points.

either the HBT or GGLP effect. The GGLP formalism has been extensively studied and improved. Although the GGLP interpretation is very illustrative and used by many experimental groups, it has some limitations and several shortcomings when applied to high-energy particle production [11]:

- The GGLP description is quasi-classical, i.e. one introduces a pion with a definite momentum p created at a definite point r, which is not in accordance with quantum mechanics. The correlation function in this formalism depends only on the difference of four-momenta $Q = p_1 - p_2$ and not on the sum $p_1 + p_2$. Both limitations disappear in the quantum statistical field theoretical approach (see below). The dependence on the momentum sum can already be obtained by abandoning spherical symmetry in the source density.

- The GGLP description assumes that two and only two bosons are produced. However in high energy collisions one usually measures inclusive spectra. This means that one would have to construct a two pion wave function in the presence of all other produced particles. In order to do this, one would have to solve the Schrödinger equation of a many-body, strongly interacting system, which is in practice impossible.

- The normalised density, R_2, is independent of isospin and thus the same for charged and neutral particles. In a more correct quantum field theory approach this is not the case. In addition, differences in the two-particle correlation function for charged and neutral pions have been experimentally observed [12].

- In the GGLP picture, the production of all the particles was assumed to be instantaneous. A priori one can always choose a zero-time t_0 after all particles are produced and have interacted and before the time they were detected. Whether particles existed before this time t_0 is therefore irrelevant. However, guessing the initial conditions at this time t_0 is far from trivial.

- Final state interactions are neglected in the naive models. They all assume that, after hadronisation, the particles propagate as free particles. We know, however, that the majority of pions are created from resonance decays and, in addition, non-resonant strong and electromagnetic interactions are present. Strong non-resonant interactions are usually not taken into account, while Coulomb effects can be easily accommodated for by the so–called Gamow correction factor. It has been shown [13] that the Gamow factor generally leads to very small corrections. The latter become significant if the four-momentum difference, Q, is smaller than 40 MeV. In e^+e^- interactions, the statistical uncertainty at such small values of Q is so large that this correction can be ignored.

- The last and probably the most fundamental restriction is that most models which use the optical analogy, assume that the momentum of the produced particles does not depend on the position of their production point. This assumption contradicts special relativity, in particular the effect of time dilatation. When momentum-position correlations are introduced ad-hoc, the width of the normalised two-particle density does not correspond to the GGLP radius parameter, R.

It is not the aim of this thesis to discuss the complete development and refining of the GGLP approach. Especially in heavy ion collisions, the theoretical approach to BEC becomes more and more sophisticated, including all possible aspects of quantum mechanical field theory and hydrodynamics. It might be useful, however, to discuss a simple quantum field theoretical formulation of R_2, showing that the interpretation is in the end not very different from the quasi-classical approach.

Quantum Field formulation of R_2

For the quantum field description of two-particle correlations due to Bose-Einstein symmetrisation, the formalism described by [11] and [14] is used. The most general definition of a two-particle normalised density is as follows:

$$R_2(\mathbf{p_1}, \mathbf{p_2}) = \frac{P_2(\mathbf{p_1}, \mathbf{p_2})}{P_1(\mathbf{p_1})P_2(\mathbf{p_2})}, \tag{1.27}$$

where

$$P_1(\mathbf{p}) = E\langle a^\dagger(\mathbf{p})a(\mathbf{p})\rangle, \tag{1.28}$$

and

$$P_2(\mathbf{p_1}, \mathbf{p_2}) = E_1E_2\langle a^\dagger(\mathbf{p_1})a^\dagger(\mathbf{p_2})a(\mathbf{p_2})a(\mathbf{p_1})\rangle. \tag{1.29}$$

Here, N denotes the total number of identical bosons. The expectation values of the creation and annihilation operators ($a^\dagger(\mathbf{p})$, $a(\mathbf{p})$) for a particle with momentum $\mathbf{p}$, and energy E, can be expressed in terms of the density matrix ρ as

$$\begin{aligned} \langle a^\dagger(\mathbf{p})a(\mathbf{p})\rangle &= \mathrm{Tr}(\rho_f a^\dagger(\mathbf{p})a(\mathbf{p})) && (1.30)\\ \langle a^\dagger(\mathbf{p_1})a^\dagger(\mathbf{p_2})a(\mathbf{p_2})a(\mathbf{p_1})\rangle &= \mathrm{Tr}(\rho_f a^\dagger(\mathbf{p_1})a^\dagger(\mathbf{p_2})a(\mathbf{p_2})a(\mathbf{p_1})), && (1.31) \end{aligned}$$

where ρ_f refers to the final state where measurements take place. We usually know or guess the density matrix only in the initial state. The relationship between the initial and final state is given by the scattering matrix S. The definition for ρ_f then becomes

$$\rho_f = S\rho_i S^\dagger. \tag{1.32}$$

The scattering matrix is given by

$$S = \mathcal{T}\exp\left(i\int d^4x\mathcal{L}_{int}(x)\right), \tag{1.33}$$

where $\mathcal{L}_{int}$ represents the interaction Lagrangian as function of the fields ϕ and $\mathcal{T}$ the chronological time-ordering operator. One can consider a scalar field produced by a current J:

$$\mathcal{L}_{int}(x) = J(x)\phi(x). \tag{1.34}$$

If $J(x)$ is a complex number and not an operator, this approach is known as the classical current approach. Consider now the case where no particles exist in the initial state. The initial state corresponds then to the vacuum $|0\rangle$ and the density matrix is given by

$$\rho = |J\rangle\langle J|, \tag{1.35}$$

Using the fact that the states $|J\rangle$ are eigenstates of the annihilation operator $a(p)$:

$$a(\mathbf{p})|J\rangle = iJ(\mathbf{p})|J\rangle, \tag{1.36}$$

where,

$$J(\mathbf{p}) = \int \frac{d^4x}{\sqrt{(2\pi)^3 2E_p}} e^{i(E_p t - \mathbf{p}\cdot\mathbf{x})} J(x) \tag{1.37}$$

the two-particle inclusive spectrum becomes

$$\begin{aligned} P_2(\mathbf{p_1}, \mathbf{p_2}) &= P_1(\mathbf{p_1}) P_2(\mathbf{p_2}), \\ P_1(\mathbf{p}) &= |J(\mathbf{p})|^2, \end{aligned} \tag{1.38}$$

i.e., there are no correlations. This is understandable since the removal of one particle does not change the total state of the system. This formalism corresponds identically to the coherent situation as described in the plane wave description of GGLP.

In [15], Gyulassy, Kauffmann and Wilson described a particle source as a superposition of N classical currents centred around space-time points x_i with momenta p_i,

$$J(x) = \sum_{i=1}^{N} f_i e^{-ip_i\cdot(x-x_i)} J_0(x - x_i), \tag{1.39}$$

where $f_i = \exp(i\xi_i)$ is a random phase factor. The momenta p_i do not need to be on the boson mass-shell. The on-shell Fourier transform of $J(x)$ is

$$J(\mathbf{p}) = \sum_{i=1}^{N} f_i e^{ip_i\cdot x_i} J_0(p - p_i), \tag{1.40}$$

where

$$J_0(p - p_i) = \int \frac{d^4x}{\sqrt{(2\pi)^3 2E_p}} e^{i(p-p_i)\cdot x} J_0(x) \tag{1.41}$$

is the Fourier transform of $J_0(x)$, and p is on-shell while p_i can be off-shell.

They choose a density operator such that for any operator $\mathcal{O}$

$$Tr(\rho\mathcal{O}) = \sum_{N=0}^{\infty} P_N \prod_{i=1}^{N} \int d^4x_i d^4p_i \rho(x_i, p_i) \times \int_0^{2\pi} d\xi_i/2\pi \langle J|\mathcal{O}|J\rangle, \tag{1.42}$$

where $\rho(x_i, p_i)$ is the covariant probability density of the source points (x_i, p_i) in phase space and P_N the probability distribution for the number of sources in the reaction. Both probabilities are normalised to unity. Using Eq. 1.36 and Eq. 1.42, Eq. 1.28 becomes

$$\begin{aligned} P_1(\mathbf{p}) &= E_p \langle |J(\mathbf{p})|^2 \rangle & (1.43)\\ &= \langle N \rangle E_p \int d^4x_1 d^4p_1 \rho(x_1, p_1) |J_0(p-p_1)|^2 & (1.44)\\ &= \langle N \rangle E_p \int d^4p_1 \tilde{\rho}(p_1) |J_0(p-p_1)|^2. & (1.45)\end{aligned}$$

Similarly, if one neglects cases where two particles are emitted from the same point one obtains for Eq. 1.29

$$\begin{aligned} P_2(\mathbf{p_1}, \mathbf{p_2}) = E_1 E_2 \Big(&\langle |J(\mathbf{p_1})|^2 \rangle \langle |J(\mathbf{p_2})|^2 \rangle \\ &+ \langle J^*(\mathbf{p_1}) J(\mathbf{p_2}) \rangle \langle J^*(\mathbf{p_2}) J(\mathbf{p_1}) \rangle \Big) \end{aligned} \tag{1.46}$$

Using Eq. 1.37 one finds:

$$J^*(\mathbf{p_1}) J(\mathbf{p_2}) = \int \frac{d^4x d^4y}{(2\pi)^3 2\sqrt{E_1 E_2}} e^{-iq\cdot x - iK\cdot y} J^*(x + \frac{1}{2}y) J(x - \frac{1}{2}y), \tag{1.47}$$

where $x = \frac{1}{2}(x_1 + x_2)$ and $y = x_1 - x_2$. Expression 1.46 can then be rewritten as

$$P_2(\mathbf{p_1}, \mathbf{p_2}) = (P_1(\mathbf{p_1}) P_1(\mathbf{p_2}) + |\bar{S}(q, K)|^2), \tag{1.48}$$

where $K = \frac{1}{2}(p_1 + p_2)$ and $q = p_1 - p_2$ are off-shell 4-vectors. The $\bar{S}$ function can be identified as the Fourier transform of a pseudo-Wigner function:

$$\bar{S}(q, K) = \int d^4x e^{-iq\cdot x} S(x, K), \tag{1.49}$$

with $S(x, K)$ identified by means of Eq. 1.37 and 1.47:

$$S(x, K) = \int \frac{d^4y}{2(2\pi)^3} e^{-iK\cdot y} \langle J^*(x + \frac{1}{2}y) J(x - \frac{1}{2}y) \rangle. \tag{1.50}$$

In the special case where $p_1 = p_2$, one has

$$\bar{S}(q, K) = \bar{S}(0, K) = P_1(p_1), \tag{1.51}$$

and we find for Eq. 1.27 an expression very similar to that obtained in the quasi-classical approach

$$R_2(\mathbf{p_1}, \mathbf{p_2}) = 1 + \frac{|\bar{S}(q, K)|^2}{\bar{S}(0, \mathbf{p_1}) \bar{S}(0, \mathbf{p_2})}. \tag{1.52}$$

The correlation term in the last expression is a ratio of Fourier transforms of Wigner functions. A Wigner function can be seen as the quantum mechanical analogue of the density of particles with momentum p at space-time point x.
The above description of the Bose-Einstein phenomenon shows how BEC could in principle be described on the basis of quantum mechanical field theory. The physical significance of the correlation function and normalised particle density can then be related to the space-time properties of the particle production source. However, when it comes to detailed predictions of experimental results reality is more complex.

In practice it is impossible to model BEC from first principles, since the strong nuclear interactions between quarks and gluons can not be calculated perturbatively when the relative energy-momentum between them becomes small. Therefore, the wave function of the system of particles created from a high-energy collision is not known. This is a well-known problem in the domain of particle physics and much effort has been spent over the years to develop phenomenological models. These hadronisation models describe the combination of coloured quarks into stable, observable particles. Due to their probabilistic nature, they are usually implemented in Monte Carlo programs. The Lund string model [16, 17] is one of the most successful approaches in this field. The general features of this model will be explained in the next chapter.

All of the known hadronisation models have a severe interpretational problem when it comes to the understanding of the Bose-Einstein mechanism. Quantum optics tells us that Bose-Einstein correlations can only arise when the particle production source is chaotic, or at least partly chaotic. Nearly all hadronisation models are known to produce particles in a coherent way, which would not allow for Bose-Einstein correlations. This is of course in contradiction with many measurements. It was even argued by B. Andersson [18] that the experimental observation of long wavelength photons ($0.2 \leq \lambda \leq 2$ fm) from a hadronic source is in perfect agreement with Low's theorem [19], which deals with completely coherent radiation.

The Lund string model allows for an elegant, quantum-mechanical implementation of the Bose-Einstein symmetrisation, based on the Area Law [20, 21]. It will be described in Sect. 2.2.3. Its interpretation is quite different from the quantum optical description given before, and does not need to produce particles incoherently. However, it can not allow interference between two independent fragmenting systems, such as two W bosons in fully hadronic W decays observed at LEP.

A way out of this paradox [22] could be that, in reality, two mechanisms are at play. Inside a single fragmenting system (e.g. $q\bar{q}$), the Lund Area law provides a coherent quantum-mechanical mechanism for Bose-Einstein symmetrisation, while the correlations between identical bosons originating from two independent fragmenting systems, if observed, can be seen as the analogue of the Hanbury Brown Twiss effect as used in astronomy.

1.2 Correlation function measurements

In what follows, a brief review of experimental techniques used in two-particle correlation analyses is given. For an extensive reading, references [23, 24] can be consulted. This section

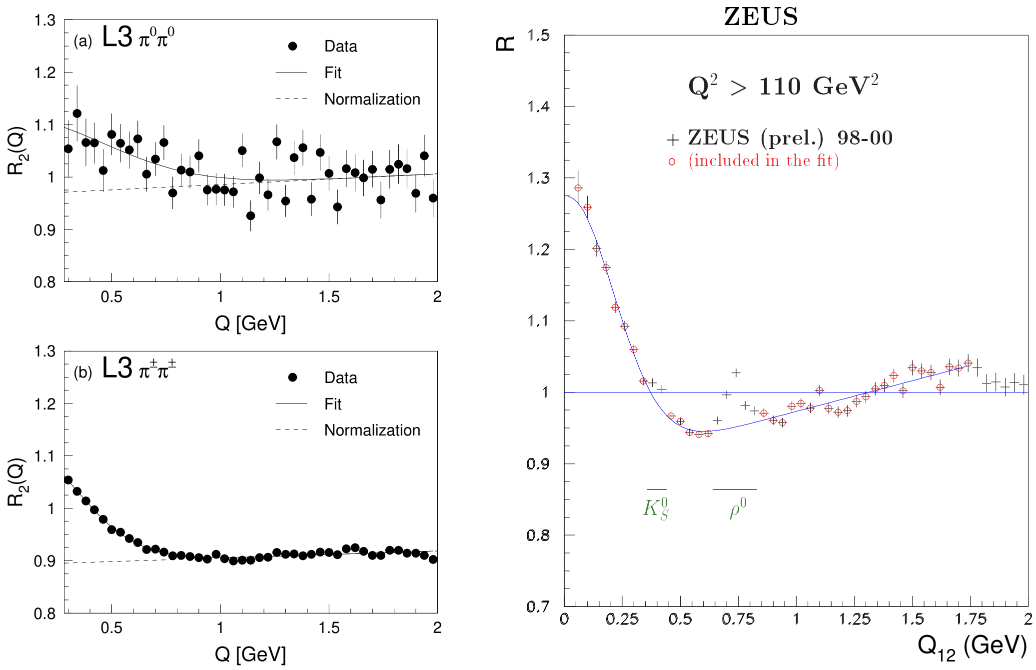

Figure 1.3: An example of a two-particle normalised density for $\pi^0\pi^0$ and equally charged pions [12] in e^+e^- interactions, using a MC reference sample (left) and using unlike-sign particles in Deep Inelastic Scattering at HERA [25] (right).

is not meant to be a complete review of all activities in Bose-Einstein correlation research. The references are therefore only a selection out of a very large literature.

In Sect. 1.1 it was discussed that in the case of chaotic sources, an enhancement in the two-particle normalised density for identical bosons

$$R_2(p_1, p_2) = \frac{P(p_1, p_2)}{P(p_1)P(p_2)}, \tag{1.53}$$

is expected.

A common parametrisation of R_2 is that used in the original GGLP papers:

$$R_2 = 1 + \lambda e^{-Q^2 R^2}. \tag{1.54}$$

Within the semi-classical picture, this approach corresponds to the case of a spherical symmetric Gaussian density of particle emitters, where the R parameter can be simply defined as the source radius. Replacing the Gaussian density by an exponential density is also possible, leading to a Breit Wigner shape of the emitters.

Another parametrisation was proposed by Kopylov and Podogretskii [26, 27, 28]. The assumption that particles are emitted from a spherical surface with incoherent point-like oscillators of lifetime τ, results in a correlation function of the form

$$C_2 = 1 + \lambda \exp(-R^2 q_t^2 - q_0^2 \tau^2), \tag{1.55}$$

$\pi^\pm\pi^\pm$ BEC analyses		Parameter	
Reaction	E_{CM} [GeV]	R [fm]	λ
$e^+e^- \to h$ [29]	29	0.97 ± 0.11	0.27 ± 0.04
$e^+e^- \to h$ [30]	34	0.82 ± 0.07	0.35 ± 0.03
$e^+e^- \to h$ [31]	91	0.83 ± 0.03	0.31 ± 0.02
$\mu p \to h$ [32]	23	0.65 ± 0.03	0.80 ± 0.07
$\pi^+ p \to h$ [33]	21.7	0.83 ± 0.06	0.33 ± 0.02
$\overline{p}p \to h$ [34]	200 - 900	0.73 ± 0.03	0.25 ± 0.02
$e\,p \to e\,h$ [35]	$110 < Q^2_\gamma$ [GeV^2]	0.67 ± 0.04	0.43 ± 0.09
Other hadron species BEC analyses in $e^+e^- \to h$		Parameter	
hadron species	E_{CM} [GeV]	R [fm]	λ
$K^\pm\, K^\pm$ [36]	91	$0.48 \pm 0.04 \pm 0.07$	$0.82 \pm 0.11 \pm 0.25$
$K^0_S\, K^0_S$ [37]	91	$0.65 \pm 0.07 \pm 0.15$	$0.96 \pm 0.21 \pm 0.40$

Table 1.1: An overview of the measured λ and R parameters, in the parametrisation of Eq. 1.54, fitted to correlation functions obtained from various reactions, at various centre-of-mass energies and for different particle species. The data selection and reference samples, as well as the applied corrections, differ from experiment to experiment. In most cases the errors given are only the statistical ones. The systematic errors are typically of the order of 10 to 20% of the measured parameter values. Adapted from [23].

where q_0 is the absolute value of the energy difference $|E_1 - E_2|$ and $q_t = |\mathbf{q} \times \mathbf{k}|/|\mathbf{k}|$, with $\mathbf{k} = \mathbf{p_1} + \mathbf{p_2}$ and $\mathbf{q} = \mathbf{p_1} - \mathbf{p_2}$. This parametrisation has the disadvantage that it is two-dimensional and that the variables are not Lorenz invariant. It is, therefore, less frequently used.

Two experimental difficulties can be identified, when considering Eq. 1.53. The first is that, in principle, the two-particle correlation function should be calculated in an six dimensional space (2× 3 momentum components). Up to now, the amount of collected data by a single experiment is not sufficient for a statistical meaningful analysis in eight dimensions. The common practice is, therefore, to project the correlation function into a lower dimension. In the simplest case one uses a one-dimensional variable, where most commonly, the Lorentz invariant variable Q^2 is chosen. It is defined as

$$Q^2 = -(p_1 - p_2)^2 = M_2^2 - 4m^2, \tag{1.56}$$

where M_2 denotes the invariant mass of the two-particle system and m is the mass of the individual particles.

The second, more important difficulty is the choice of reference sample, denoted by $P(p_1)P(p_2)$. It is generally replaced by a two-particle density, equal to the analysed data set, except for the Bose-Einstein effects. It is clear that such an ideal reference sample does not exist.

Two classes of reference samples are in common use. Either a sample without BEC is created using real data itself, or Monte Carlo generated samples are used which do not include the Bose-Einstein effect. These samples are subjected to a full simulation of the experimental setup. For the latter, one has to rely on a correct description of the detector acceptances and resolutions. The results are, therefore, dependent on the modelling and tuning of the fragmentation used in the generator.

When the data itself are used for comparison, several methods exist, each with different drawbacks:

- The most straightforward reference sample is the two-particle density of unlike-sign boson pairs. Since the charge of these pairs are opposite, they do not obey Bose-Einstein statistics. The drawback of this method is that the bulk of oppositely charged pairs originate directly from resonance decays, whereas like-sign pairs are only indirectly affected. The regions dominated by resonances are usually omitted in the fits.

- Another method uses pairs coming from different events in order to construct a "mixed" reference sample. Here one has the disadvantage that many correlations, e.g. those due to conservation laws and kinematics are eliminated as well. Therefore one tends to overestimate the Bose-Einstein correlations.

- A third method can be applied for events which are strongly aligned along a given axis, typically two jet Z^0 decays. There one can divide the event into two hemispheres perpendicular to the event axis and mix particles from different hemispheres, provided that the particles from opposite hemispheres are folded along the event axis.

Examples of two particle correlation functions measured in e^+e^- annihilation and deep inelastic scattering, using different reference samples are shown in Fig. 1.3. An overview of measured correlation strengths and source sizes is given in Table 1.1 for various reactions and particle species. From Table 1.1 one can observe that the values for the source radius R are all below 1 fm and that no clear dependence on the centre-of-mass energy is found. The difference in the values of λ and R between different experiments can be attributed to the different analysis procedures, such as data selection, the choice of reference sample, etc.

The measured correlation strength is generally lower than the true strength. This is due to experimental resolutions, misidentification of particles, particles coming from long lived resonances, Coulomb- and strong interactions between the particles, etc. When measuring pion correlations in multi-hadron final states at high energies, many experiments assume that all charged particles in the final state are pions, which is a good approximation, since they are most abundantly produced in these reactions.

Besides the measurement of correlations among identical bosons, one can also measure correlations among identical fermions, such as protons [38] or Λ particles [39]. In this case, one observes a depletion at low energy-momentum differences, compared to the case when Fermi-Dirac statistics are not included. Also correlations of higher orders have been measured [40, 41]. These can give an indication about the degree of coherence of the emitting source. However, the results for several types of interactions are quite contradictory.

Several experiments have gone beyond measurements of BEC in the one-dimensional Q-distribution, and performed more differential, multi-dimensional analyses [42, 43], which are sensitive to the shape of the production volume and the duration of particle emission. This leads to the conclusion that, at least in e^+e^- annihilation and in hadron-hadron collisions, the particle production source is not spherical, but elongated along the event axis.

It has also been measured that, if strong Bose-Einstein correlations between like-sign pion pairs are observed, a considerable amount of correlations is seen in unlike-sign pion pairs as well. It is not believed that this is due to the Bose-Einstein effect itself, but mainly a reflection of the correlations between like-sign pairs. The distortion of the ρ resonance mass spectrum is a good example of this feature [44].

Finally it should be mentioned that in ultra-relativistic heavy ion collisions, the BE effect is used extensively to measure dimensions, shapes of the interaction region and the expansion of the production volume. The main difference with what is shown in Table. 1.1 is that in heavy ion collisions, the source sizes are typically of the order of several fermi and correlated with the geometrical sizes of the nuclei, see for example [45].

Chapter 2

QCD and Monte Carlo generators

In high energy physics, many theoretical model predictions for collisions leading to multi-particle final states, are implemented in the framework of Monte-Carlo programs. These programs try to describe the consequences of any theoretical input as accurately as possible, keeping in mind that a sufficient amount of simulated data is necessary to test predictions up to a given accuracy.

The modelling of a high energy e^+e^- interaction is usually subdivided into several steps, as illustrated in Fig. 2.1. At LEP the first stage is described by the interaction of an electron with a positron, resulting into the production of two or more fermions, depending on the energy. These processes can be described by electroweak theory, usually to very high precision. If quarks occur in this electroweak process, their evolution is described by perturbative QCD up to a point where the strong coupling constant, α_s, becomes too large to use perturbation theory. The point at which this stage is stopped is usually a free parameter of the Monte Carlo program. After this one enters in the non-perturbative regime of QCD where coloured quarks are combined into colourless hadrons. This stage relies on phenomenological models such as the successful Lund model, described in Sect. 2.2. Finally, unstable hadrons are allowed to decay into stable, experimentally observable particles. These decays are usually well-known. The quantum-mechanical implementation of Bose-Einstein correlations is described in Sect. 2.2.3. It will be shown that, despite its rigorous treatment, it fails to implement the Bose-Einstein effect in complex systems such as multi-jet events and hadronic WW decays. An alternative way of implementing Bose-Einstein correlations in Monte Carlo programs is discussed in Sect. 2.3.

2.1 Parton Shower

After the generation of an electroweak process, final-state QCD radiation has to be added in order to give predictions about a stable hadronic final state. Instead of aiming for an exact analytical prediction up to some fixed order in perturbation theory, one can opt for an approximate result, which takes into account higher-order contributions. This leads to the so called *parton shower* formalism [46]. It lends itself to a very natural and efficient Monte Carlo implementation.

The parton shower in the leading-order approximation of perturbative QCD, as it is imple-

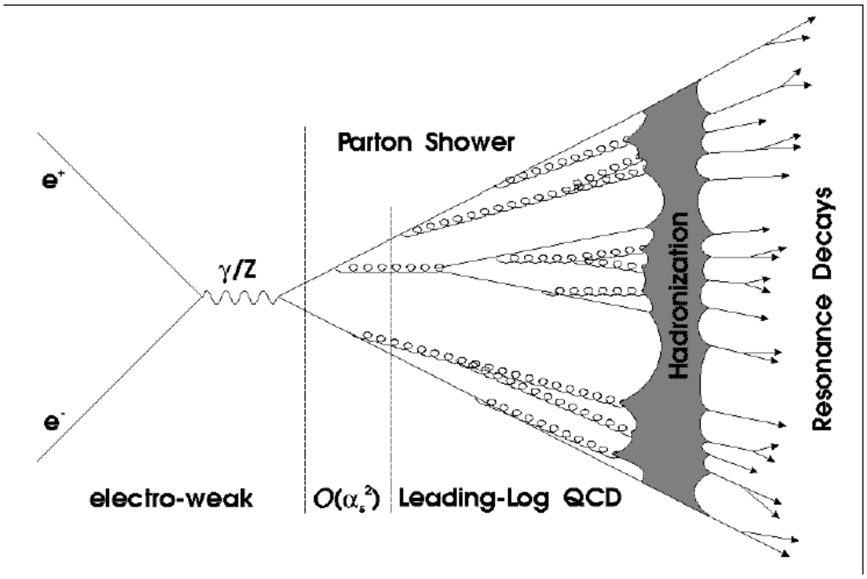

Figure 2.1: The four phases leading to the production of stable hadrons which are observed in our detectors.

mented in the JETSET Monte Carlo model [47], can be viewed as a sequence of branchings of the type $\mathrm{a} \to \mathrm{bc}$, where a mother particle, being a quark (q) or a gluon (g), branches into two daughters. Each daughter can subsequently branch further, so that effectively a shower-like structure evolves. The hadronic branchings include the splittings $\mathrm{q} \to \mathrm{qg}$, $\mathrm{g} \to \mathrm{gg}$ and $\mathrm{g} \to \mathrm{q\bar{q}}$.

The kinematics are expressed in terms of two variables[1], Q^2 and z. These variables can have different interpretations, depending on the implementation. In the parton shower picture, Q^2, has the dimensions of squared mass, while z represents the energy fraction taken by parton b from a, thus giving c an energy fraction $1 - z$.

The probability for a parton to branch is given by the Altarelli-Parisi evolution equation [46]:

$$\frac{d\mathcal{P}_a(z)}{dt} = \sum_{b,c} \frac{\alpha_s}{2\pi} P_{a\to bc}(z) dz, \tag{2.1}$$

where a new variable $t = \ln(Q^2/\Lambda^2_{QCD})$ is introduced, with Λ_{QCD} the scale at which $\alpha_s(Q^2)$, the strong coupling, becomes strong. The sum is running over all of the above mentioned possible branchings. The so-called splitting kernels, $P_{a\to bc}(z)$, are known for all possible branchings. They are used to generate the energy fractions z and $1-z$ carried by the daughter partons in the centre-of-mass frame of the event. The t variable is acting as a kind of time parameter of the shower evolution, gradually decreasing away from the hard scattering in final-state showers.

The probability that no branching occurs during a small interval $\delta \mathrm{t}$ is given by $1 -$

[1]The four-momentum transfer, Q, between the mother and daughter particles should not be confused with the four-momentum difference, Q, used in the description of Bose-Einstein correlations.

$\sum_{b,c} \mathcal{I}_{a\to bc}(t)\delta(t)$, with

$$\mathcal{I}_{a\to bc}(t) = \sum_{bc} \int_{z_-(t)}^{z_+(t)} dz \frac{\alpha_s}{2\pi} P_{a\to bc}(z). \tag{2.2}$$

If a branching starts at time t_0, the probability that the parton has not branched at a later time $\mathrm{t} > \mathrm{t}_0$ is then given by exponentiating the former expression:

$$\mathcal{P}_{\text{no branching}}(t_0, t) = exp\left(-\int_{t_0}^{t} dt' \sum_{b,c} \mathcal{I}_{a\to bc}(t')\right) = S_a(t), \tag{2.3}$$

which is known as the Sudakov form factor and very useful in Monte Carlo implementations. However, since we do not start from a t_0, but from an initial t_{max}, one calculates the no–branching factor as

$$\mathcal{P}_{\text{no branching}}(t_{max}, t) = S_a(t_{max})/S_a(t). \tag{2.4}$$

As t or Q^2 is decreasing during the shower evolution, one eventually reaches a value, Q_0, for which $\alpha_s(Q_0^2)$ becomes large and perturbation theory no longer applies. The parton shower evolution is stopped at this point. Q_0 is typically of the order of the masses of light hadrons ~ 1 GeV. The parameters Q_0 and Λ_{QCD} from Eq. 2.1 are two important free parameters in the JETSET model.

2.2 Hadronisation

In the QCD confinement regime, where the strong coupling constant is large and perturbation theory breaks down, coloured partons are transformed into colourless hadrons. This process is called hadronisation. At present this process can only be described with the help of phenomenological models. The mainstream of these models can be divided in three classes: string fragmentation, independent fragmentation models and cluster models. Relevant for the implementation of the Bose-Einstein effect is the string fragmentation, based on the Lund model [16, 17].

In the simplest case of a two jet (e.g. quark and anti-quark) system, where no hard gluon is emitted from one of the quarks, the string model can be understood as follows. The energy stored in the colour dipole field between a quark and anti-quark increases linearly with their separation. This is related to the confinement property of QCD. As the quark and anti-quark move apart from their common production vertex a thin colour flux tube is spanned between them, having a typical transverse size of ~ 1 fm. The dynamics of this tube can be described by that of a massless relativistic string with no transverse degrees of freedom. Inside the tube we have an energy density per unit length of $\kappa \sim 1\mathrm{GeV/fm}$. As the endpoints of the string move further apart, the potential energy stored inside the string increases and the string may at some point break to produce a new $q\bar{q}$ pair by means of quantum mechanical tunnelling. In this way, two new string pieces are created, which can break up further if their energy is sufficient to create new $q\bar{q}$ pairs. This break-up process continues until we finally end up with hadrons on their mass shell.

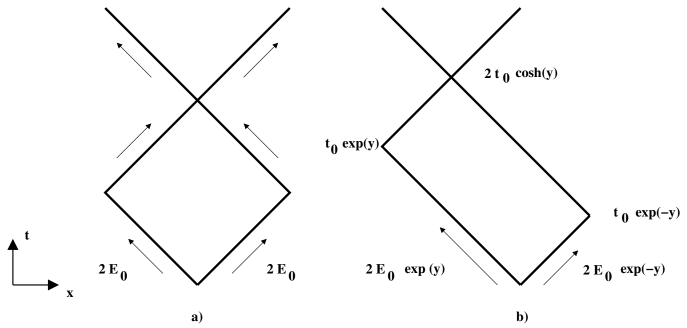

Figure 2.2: The space-time diagram of the motion of a $q\bar{q}$ system a) at rest, b) after a Lorenz boost along the positive direction.

The quantum mechanical tunnelling process implies the suppression of heavy quark production in the ratios: $\mathrm{u}:\mathrm{d}:\mathrm{s}:\mathrm{c} \approx 1:1:0.3:10^{-11}$. It also allows the newly created $q\bar{q}$ pair to acquire transverse momentum, p_t, provided that the p_t of the quark and anti-quark are opposite and equal in size.

A complete and detailed description of the impressive machinery behind the Lund model would lead us too far and is beyond the scope of this work. Let us suffice to briefly describe two basic mechanisms which characterise the Lund Model: the movement of a massless relativistic string and the production of quark-antiquark pairs due to quantum mechanical tunnelling.

2.2.1 Particle production in the Lund string model

Consider the motion of a massless quark (q) and antiquark ($\bar{q}$), interacting via a constant force in one space and one time dimension. The Hamiltonian of the system is given by

$$H = |p_1| + |p_2| + \kappa|x_1 - x_2|, \tag{2.5}$$

with p_1 and p_2 the momenta and x_1 and x_2 their positions. The particles move at the speed of light with the equation of motion for one of the particles

$$\begin{aligned} dp/dt &= -\kappa, &(2.6)\\ dx/dt &= dE/dp = p/E, \qquad E = \sqrt{p^2 + m^2}. &(2.7) \end{aligned}$$

This means that in the centre-of-mass frame, the two particles will oscillate back and forth in the so-called "yo-yo" mode, as shown on the left in Fig. 2.2. Solving the Eqs. 2.7 one obtains the relationship:

$$\begin{aligned} p &= p_0 - \kappa t = \kappa(t_0 - t), &(2.8)\\ E &= E_0 - \kappa x = \kappa(x_0 - x), &(2.9)\\ m^2 &= E^2 - p^2 = \kappa^2\Big((x_0 - x)^2 - (t_0 - t)^2\Big), &(2.10) \end{aligned}$$

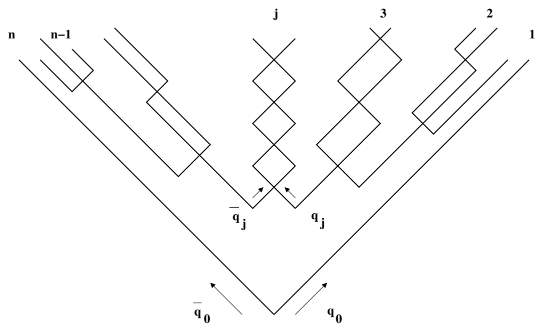

Figure 2.3: Break-up of a string stretched between a $q\bar{q}$ pair, according to the Lund string model.

where the last equation describes a hyperbola in space-time.

Expression 2.10 restricts the production of a hadron with mass m, composed of the $q\bar{q}$ pair, to a hyperbolic curve in space-time. This hyperbola can be re-parametrised as a function of the one-dimensional rapidity defined as $\cosh(y) = \frac{\kappa \Delta x}{m} = E/m$, $\sinh(y) = \frac{\kappa \Delta t}{m} = p/m$, so that Eq. 2.10 becomes

$$(x_0 - x, t_0 - t) = \frac{m}{\kappa}(\cosh y, \sinh y) \tag{2.11}$$

If the mass of the particles vanishes, the particles will move along the light cones $|\mathrm{t} - \mathrm{t_o}| = \mathrm{x_0} - \mathrm{x}$. Boosting the yo-yo system at rest results in a situation given on the right in Fig. 2.2.

This process can be continued iteratively to produce a multi-hadron final state. All produced hadrons will be bound to be produced on hyperbola, where the production point x_2, t_2 is known using the production point, x_1, t_1, of the previous hadron:

$$(x_2 - x_1, t_2 - t_1) = \frac{M_{had}}{\kappa}(\cosh y_{had}, \sinh y_{had}). \tag{2.12}$$

The geometrical, one-dimensional picture of particle production is sketched in Fig. 2.3, where several hadrons, denoted by the numbers 1 to n are produced. It can be seen from the figure that the hadrons containing the original q or $\bar{q}$ are produced last in the centre-of-mass frame, and that the total geometrical picture is symmetric with respect to the q and $\bar{q}$. At this point, and remembering the discussion in Sect. 1.1.3, it is important to note that , in a relativistically invariant model, such as the Lund model, the production point of a particle and its momentum are strongly correlated.

2.2.2 Mass and transverse momentum generation

Consider the relativistic string in its rest frame. The action principle governs its motion and does not forbid the system to break up. However it does not give any prediction about where and when the break-up will occur. Thus, one is free in the choice of a model, describing the break-ups, only with one main constraint: we want to produce detectable (on mass shell) final state particles. We saw already in Eq. 2.12 that as soon as one break-up has occurred, the

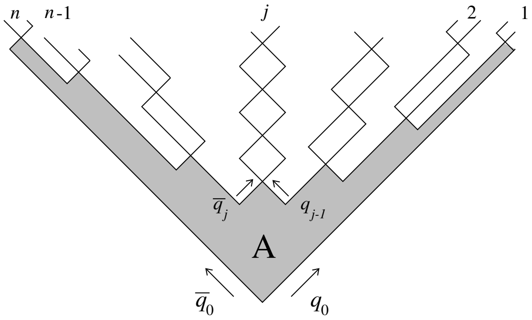

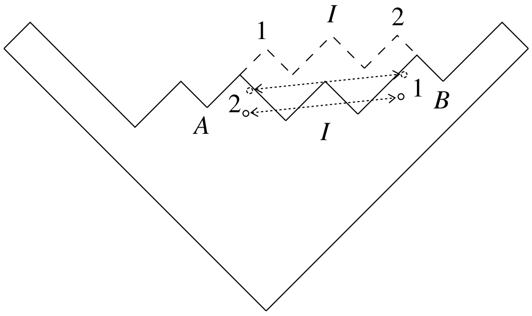

Figure 2.4: A decaying string (left): the area spanned by the string is indicated by the shaded surface, when two identical particles 1 and 2 are interchanged (right) the area under the string changes (dashed line).

next one is bound to be on a well-defined hyperbola. The break-up point on this hyperbola is chosen on the assumption that each space-time point along the string has equal probability of being this breaking point. This scheme is compatible with the so called inside-outside cascade formalism, implying that in any frame, the lowest-momentum particle is produced first.

In order to describe realistic situations, transverse momentum, p_t, and mass, m, have to be generated at every break-up. This is done by a quantum mechanical tunnelling mechanism à la Schwinger, according to the probability law

$$P(m_t) \sim \exp(-\frac{\pi}{\kappa}m^2)\exp(-\frac{\pi}{\kappa}p_t^2). \tag{2.13}$$

This formula allows the Lund model to generate the transverse momentum distribution of produced quarks according to a Gaussian with a width $\sigma_q = \sqrt{\kappa/2\pi} \equiv 0.3$ GeV and automatically introduces the suppression of heavy quark flavors due to the mass dependent term in Eq. 2.13. The probability distribution of the longitudinal momentum fraction, z, of a hadron is determined using the Lund symmetric fragmentation function:

$$f(z) = \frac{(1-z)^a}{z}\exp(-\frac{b \cdot m_t^2}{z}), \tag{2.14}$$

where $m_t^2 = m^2 + p_t^2$ is the transverse mass squared of the hadron. Here, a and b are two additional parameters of the JETSET model. In principle, b is universal, whereas a can depend on the quark flavor. For heavy quarks an alternative, the so called Peterson fragmentation [48] function, is used:

$$f(z) = \frac{1}{z(1-\frac{1}{z}-\frac{\epsilon_q}{1-z})^2}, \tag{2.15}$$

where ϵ_q is a parameter which depends on the flavour (c,b) of the fragmenting quark. Again, these parameters are to be determined from experiment.

2.2.3 The Lund interpretation of BEC

In Sect. 2.2.2 it was shown how, in the Lund model, particles are produced along a string by means of quantum-mechanical tunnelling. Expression 2.13 showed the production probability for the creation of a quark- or antiquark with transverse mass $m_t = \sqrt{m^2 + p_t^2}$. In the geometrical interpretation of the Lund model this probability can be identified with the space-time area spanned under the string, as is sketched in Fig. 2.4.

The probability, from Eq. 2.13 can be regarded as the square of a matrix element of the form

$$\mathcal{M} = \exp(i\kappa - b/2)A, \tag{2.16}$$

where the parameter b, related to the string tension κ, should not be confused with the fragmentation function parameter b from previous section.

Consider now a final state containing n identical bosons. There are $n!$ ways to produce such a state, corresponding to different permutations of the particles. When the transition matrix element is symmetrised with respect to the exchange of identical bosons the total production amplitude for n identical bosons reads

$$\mathcal{M} = \sum_{\mathcal{P}} \mathcal{M}_{\mathcal{P}}, \tag{2.17}$$

where the sum goes over all possible permutations $\mathcal{P}$. The cross-section will then contain the square of this symmetrised amplitude $\mathcal{M}$

$$|\mathcal{M}|^2 = \sum_{\mathcal{P}} (|\mathcal{M}_{\mathcal{P}}|^2 (1 + \sum_{\mathcal{P}' \neq \mathcal{P}} \frac{2\mathrm{Re}(\mathcal{M}_{\mathcal{P}} \mathcal{M}^*_{\mathcal{P}'})}{|\mathcal{M}_{\mathcal{P}}|^2 + |\mathcal{M}_{\mathcal{P}'}|^2})). \tag{2.18}$$

One can observe from this expression that an extra interference term is introduced. In a Monte Carlo program it can be introduced by weighing each event with a factor

$$w = 1 + \sum_{\mathcal{P}' \neq \mathcal{P}} \frac{2\mathrm{Re}(\mathcal{M}_{\mathcal{P}} \mathcal{M}^*_{\mathcal{P}'})}{|\mathcal{M}_{\mathcal{P}}|^2 + |\mathcal{M}_{\mathcal{P}'}|^2}. \tag{2.19}$$

The outer sum in Eq. 2.18 is taken care of by generating many events. The permutation of two particles corresponds to a change in area under the string as can be seen from Fig. 2.4. The weight, in terms of the area difference due to the interchange of two particles, then reads

$$w = 1 + \sum_{\mathcal{P}' \neq \mathcal{P}} \frac{\cos \frac{\Delta A}{2\kappa}}{\cosh \left(\frac{b \Delta A}{2} + \frac{\Delta(\sum p^2_{\perp q})}{2\sigma^2_{p_\perp}} \right)} \tag{2.20}$$

This approach has the advantage that the method is close to the true quantum-mechanical symmetrisation of an n particle matrix element. In addition, it requires no extra parameters, as other models do (see next section). An additional advantage is that the R parameter in Eq. 1.21, measured from the correlation functions generated by this approach is of the order of 1 fm, precisely what is measured in e^+e^- interactions. Importantly, we note that, in this case, the R parameter is not related to the total source radius, but rather to the distance over which transverse momentum is compensated along the string.

For partonic states composed of multiple strings, one major problem remains, however. There are no means by which the area difference resulting from the interchange of particles from a different string, can be computed. Unfortunately, this is precisely the case for two decaying W bosons in the reaction $e^+e^- \to W^+W^-$ or, for Z^0 decays where the radiation of a hard gluon produces a kink in the string.

2.3 Modelling BEC in PYTHIA

As emphasised in [49], no rigorous method exists to date which would allow to account for the Bose-Einstein symmetrisation of the production amplitudes in Monte Carlo event generators. The algorithms implemented in the Monte Carlo event generator JETSET [47] which simulate the Bose-Einstein effect, are all based on introducing BEC as local shifts of final-state particle momenta among pairs of identical particles. They differ only in the way global energy and momentum conservation is ensured. Other, so called "global-weight" methods, have been proposed wherein a single weight factor is assigned to each event, calculated on the basis of a model for the identical-pair two-particle correlation function [21, 50]. The Lund area law model, as it is described in Sect. 2.2.3, can be considered as a global-weight model.

The global re-weighting methods are somehow more theoretically appealing since they leave the original generated event untouched. However, they are restricted by many experimental facts about hadron production at LEP. Most of these restrictions have their origin in the factorisation property of QCD, which states that the non-perturbative phase cannot influence the hard perturbative phase of the QCD cascade. Whereas many models with global weights break this factorisation property, the ones with local weights take it as a starting point.

The local model LUBOEI, as it is implemented in JETSET, will be discussed in more detail below, since it is currently the most widely spread comparison model within the LEP community. A general overview of models with a detailed description of the LUBOEI variants is given in [49, 51].

2.3.1 The LUBOEI model

The LUBOEI model takes as starting point the hadrons produced by the string fragmentation in JETSET, where no Bose-Einstein effects are present. It shifts the momenta of identical bosons i and j such that the inclusive distribution of the relative separation Q of identical pairs is enhanced by a factor $f_2(Q) \geq 1$. The latter is parametrised with the phenomenological form

$$f_2(Q) = 1 + \lambda \exp(-Q^2R^2), \tag{2.21}$$

where Q is the difference in four-momenta of the pair.

Short-lived resonances like the ρ and K^* are allowed to decay before the BE procedure is applied, while decay products of longer-lived ones (width $\Gamma < 20$ MeV/c^2) are not affected.

Starting from the ansatz that the original Q distribution is given by the two-particle phase space, $d^3p/E \propto Q^2dQ^2/\sqrt{Q^2+4m^2}$, an appropriate shift δQ for a meson pair with separation Q can be given by calculating δQ from the following relation:

$$\int_0^Q \frac{q^2dq}{\sqrt{q^2+4m^2}} = \int_0^{Q+\delta Q} f_2(Q)\frac{q^2dq}{\sqrt{q^2+4m^2}}. \tag{2.22}$$

Expression 2.22 prescribes a negative δQ, for any $f_2(Q) \geq 1$, but the corresponding change in particle momenta is not unique. Energy and momentum cannot be simultaneously conserved. The model chooses to conserve three-momentum in the frame where the algorithm is applied. For a given set of particles i and j the change in momenta is

$$p'_i = p_i + \delta p_i^j \tag{2.23}$$
$$p'_j = p_j + \delta p_j^i, \tag{2.24}$$

with $\delta p_i^j + \delta p_j^i = 0$. The BE_0 model[2] takes $\delta p_i^j = c(p_j - p_i)$, corresponding to pulling the particles closer along the line connecting them in the current frame. A given particle is likely to belong to more than one pair. If the momentum shifts as described above are performed in a specific order, the end result will depend on this order. Therefore, first all pairwise shifts are calculated on the basis of the undisturbed momentum configuration, and afterwards each momentum p_i is shifted to $p'_i = p_i + \sum_{j\neq i}\delta p_i^j$. The above procedure preserves total momentum, while the shift on particle pairs toward each other reduces the total energy, since the invariant mass is reduced. In practice this is solved by rescaling all three-momenta by a common factor, which is very close to unity.

In general, the model describes two and even three particle correlations in $e^+e^- \to Z^0 \to q\bar{q}$ reactions very well. It can therefore also be successfully applied to the decay of a single W boson into quarks.

When it is applied to $e^+e^- \to W^+W^- \to q_1\bar{q}_2q_3\bar{q}_4$ reactions, including particles coming from the decay of the two different produced W's, large shifts in the reconstructed W mass, of the order of 100 MeV are predicted [51]. The BE_0 model has, however, some flaws when no BEC are allowed between particles coming from different W's. In this case, the global rescaling to conserve the total energy introduces unwanted negative shifts in the reconstructed W mass (M_W). Variants of the BE_0 model were constructed in order to overcome this problem.

All these variants are based on calculating an additional shift δr_k^l for some subclass of particle pairs. In the end each particle momentum will then be shifted to

$$p'_i = p_i + \sum_{j\neq i}\delta p_i^j + \alpha\sum_{k\neq i}\delta r_i^k, \tag{2.25}$$

where the parameter α is adjusted separately for each event so that the total energy is conserved.

The weight factor $f_2(Q) = 1 + \lambda\exp(-Q^2R^2)$ is somehow arbitrary and can be adjusted to take into account possible oscillatory behaviour due to non-Gaussian sources or to obtain better agreement with global weight approaches.

[2] following the nomenclature in [49].

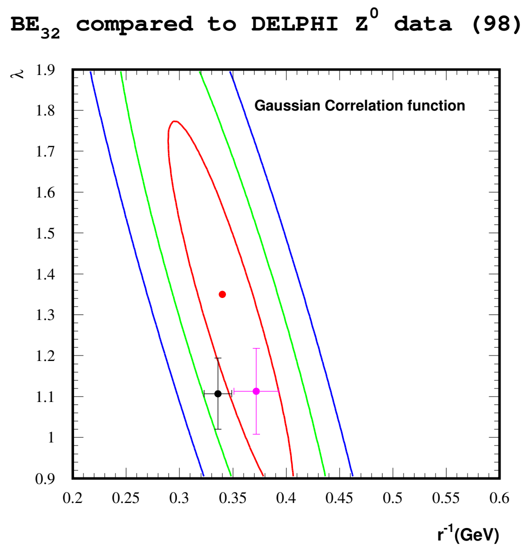

Figure 2.5: One, two and three sigma contours for the values of λ and R used in the BE$_{32}$ model, obtained from a χ^2 fit to the inclusive two-particle density $\rho(Q)$ for like-sign particles. *J. D'Hondt, private communications.*

In the BE$_3$ model, δr_i^k is only non-zero for pairs of identical bosons and $f_2(Q)$ is multiplied by an additional factor $1 + \alpha \exp(-Q^2R^2/9)$.

The much-used BE_{32} model is a modification of BE_3 where $f_2(Q)$ is adjusted in such a way that $f_2(0) = 1 + \lambda$. The weight function now takes the form

$$f_2(Q) = \left\{1 + \lambda \exp(-Q^2R^2)\right\}\left\{1 + \alpha\lambda \exp(-Q^2R^2/9)\left(1 - \exp(-Q^2R^2/4)\right)\right\}. \tag{2.26}$$

In other modifications, which will not be discussed further, the original simple form of $f_2(Q)$ is retained. The energy and momentum is conserved by shifting other non-identical particle pairs apart, being "closest" to the pair affected by the BE effect. These models differ in the definition "closeness" and are known under the names of BE_m and BE_λ.

2.3.2 The tuning of JETSET and LUBOEI in DELPHI

As was shown before, the JETSET Monte Carlo model has a set of basic parameters, of which Q_0, Λ_{QCD}, σ_q, a and b are the most important.

Although most of the JETSET parameters are bound by theoretical and experimental constraints, there is still room for variation. Therefore, the JETSET Monte Carlo model (and also other commonly used fragmentation models) has been tuned to data collected at the centre-of-mass energy of 91.2 GeV where the Z^0 boson is abundantly produced. This large amount of data allows a comparison by means of a χ^2 fit of the JETSET model with event

Λ_{QCD}	Q_0	σ_q	a	b	λ_{BE32}	R_{BE32}
0.297	1.34	0.401	0.409	0.844	1.35	0.60 fm

Table 2.1: Summary of the essential parameters of JETSET tuned to DELPHI Z^0 data. The LUBOEI BE32 parameters tuned to the like-sign two-particle inclusive density in Q are given in the last two columns.

shapes and single particle spectra. For further details we refer to [52]. A summary of the on DELPHI data tuned values of the most important JETSET parameters is given in Table 2.1.

The DELPHI standard tuning does not take into account the presence of Bose-Einstein correlations, although they are well measured at the Z^0 [53]. The LUBOEI algorithm was only used later in special Monte Carlo samples for BEC studies.

In this work, the BE_{32} model was used for all studies. The use of the LUBOEI algorithm introduces two new parameters to be tuned, hereafter called λ_{BE32} and R_{BE32}[3]. These two parameters were tuned on the Q distribution for like-sign pairs only, using data collected at the Z^0 peak. Although the unlike-sign Q distributions are affected by the presence of BEC as well, it was found impossible to tune the BE_{32} model to both the like-sign and unlike-sign Q spectra simultaneously. The tuned values of λ_{BE32} and R_{BE32} are shown in Table 2.1. A χ^2 comparison of the like-sign Q distributions was made using three sets of values for λ_{BE32} and R_{BE32}. The χ^2 contours corresponding to one, two and three standard deviations are shown in Fig. 2.5. Note the large positive correlation between λ and R.

2.3.3 Other hadronisation models

Although string fragmentation, as implemented in the JETSET code, is very successful, alternative fragmentation models exist. In what follows, two alternative fragmentation models, HERWIG [54, 55] and ARIADNE [56] will be briefly discussed. They will be used in chapter 4 for the evaluation of the systematic uncertainty in the inter-W BEC measurement.

The Ariadne Colour Dipole model

All parton shower cascades, including the one in JETSET, start with the radiation of a single gluon form either the primary quark or anti-quark. The $q\bar{q}$ system can be regarded as being a colour dipole in terms of the colour interaction field in between them. The probability of radiating a single gluon can be calculated perturbatively. The cross-section in first order of α_s is given by

$$\frac{d^2\sigma}{dx_1 dx_2} \propto \frac{x_1^2 + x_2^2}{(1-x_1)(1-x_2)}, \tag{2.27}$$

where x_1 and x_2 are the energy fractions of the quark and anti-quark after emission. While JETSET continues the parton shower using the DGLAP evolution Eq. 2.1, ARIADNE uses

[3]In the JETSET code they correspond to the parameter PARJ(92) for λ and PARJ(93) for R, expressed in GeV^{-1} units.

the dipole formula for the sequential branchings up to the parton shower cutoff scale Q_0. The hadronisation is performed using the JETSET string fragmentation. The use of the dipole formula automatically ensures angular ordering, while in other models it has to be introduced by hand. The general picture is that, after generation of the first $q\bar{q}$ dipole, each gluon emission creates a new dipole.

The HERWIG cluster model

The HERWIG cluster model uses the DGLAP equations, computed up to one order in α_s higher than in JETSET, and has explicit angular ordering built in. After the parton shower is stopped, the remaining gluons are forced to split into $q\bar{q}$ pairs. Subsequently, all final partons are combined in colourless clusters. These clusters can, according to their mass, form stable hadrons or can further decay into lighter hadrons.

Chapter 3

Experimental setup

3.1 The LEP collider

In august 1989 a new era of particle physics research was started when the LEP (Large Electron Positron) collider became operational. After more than ten years of dazzling research its dismantling was started in november 2000. It will be replaced by a new accelerator, the LHC (Large Hadron Collider) which will accelerate proton beams up to energies in the TeV range, where new phenomena beyond the Standard Model are likely to emerge.

With a circumference of nearly 27 km, LEP was the largest accelerator ever built. It was located in a tunnel between 50 and 150 metres underground on the French-Swiss border, housed by the European Organisation for Nuclear Research, CERN, in Geneva. LEP was designed to accelerate electrons and their antimatter counterparts, positrons, in opposite directions and make them collide in four interaction points, surrounded by four detectors: ALEPH, OPAL, DELPHI and L3.

The complete LEP collider does not consist of just the large LEP ring. There are a number of other, smaller CERN accelerators in which the particles are accelerated, before being injected in the main ring. A schematic view of the complete acceleration cycle is given in Fig. 3.1. Electron and positrons are produced and accelerated in the LEP injector Linacs up to 600 MeV. The Electron-Positron Accumulator collects them in bunches which are accelerated to 3.5 GeV in the Proton Synchrotron (PS). Finally, the Super Proton Synchrotron accelerates them to 22 GeV before injection in the LEP ring.

Four particle bunches, containing on average $3 \cdot 10^{11}$ particles, are kept on a circular orbit and focused into narrow beams by a complex system of dipole and quadrupole magnets. The bunches are accelerated by Radio Frequency (RF) cavities. During its first operational period, called LEP1, copper RF cavities were used to reach a nominal centre-of-mass energy of ~ 91 GeV, corresponding to the mass of the Z^0 boson. After 1996, during the LEP2 period, the centre-of-mass energy was increased up to 209 GeV using superconducting cavities. This allowed the study of pair produced W^+W^- bosons and the search for the enigmatic Higgs boson and supersymmetric particles.

In the collision points, the interaction rate for a specific process depends on the cross-section, σ, for that process and the number of beam particles that traverse the interaction

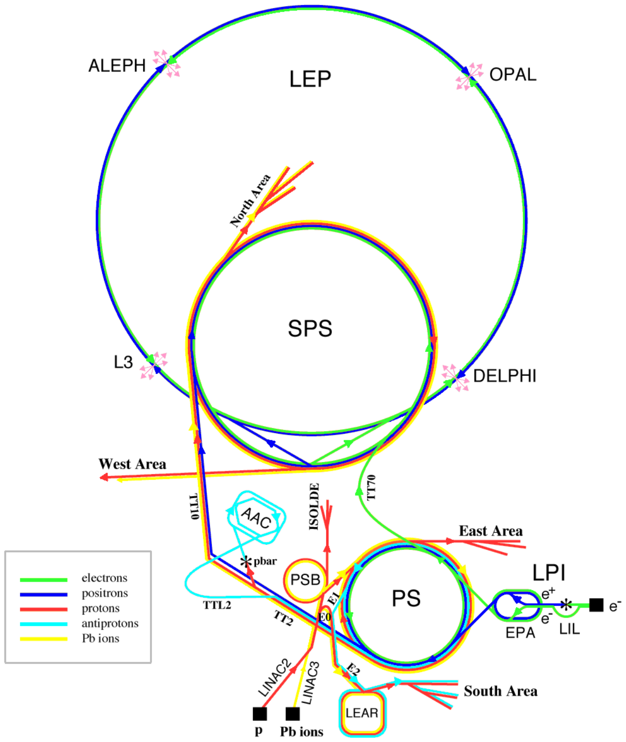

Figure 3.1: A schematic view of the LEP acceleration cycle.

region per second and per unit surface. This instantaneous luminosity, $L(t)$ is given by

$$L(t) = \frac{N_{e^-} N_{e^+} n_{\text{bunch}} f}{4\pi\sigma_x\sigma_y}, \tag{3.1}$$

where N_{e^-} and N_{e^+} are the number of electrons and positrons per bunch, n_{bunch} is the number of bunches and f is the bunch revolution frequency. The size of the beam at the interaction point in the plane perpendicular to the direction of motion is represented by σ_x and σ_y. The instantaneous luminosity depends on the LEP machine conditions and the time the bunches are circulating in the machine during a fill (period between the injection of the bunches in LEP and the moment when the beams are dumped). At the beginning of a fill the instantaneous luminosity reaches values of 10^{32} cm^{-2} s^{-1}. The total number of collected events for a given process over a certain time period is given by the product of its cross-section and the integral of the instantaneous luminosity over time

$$N_{evt} = \sigma \cdot \int L(t) \quad dt = \sigma\mathcal{L}. \tag{3.2}$$

The total integrated luminosity, $\mathcal{L}$, of a given period is calculated with high precision by measuring small angle Bhabha scattering ($e^+e^- \rightarrow e^+e^-$), for which the cross-section is precisely known from theoretical calculations. The integrated luminosities, collected by the DELPHI detector in the years analysed in this thesis, together with the corresponding centre-of-mass energies, is given in Tab. 3.1. After September 1st of 2000, one sector (corresponding to 1/12) of the main track detector of DELPHI, the TPC, failed beyond repair. The data collected afterwards was not analysed in this thesis. It corresponds roughly to 27% of the total amount of collected data in that year.

Year	1998	1999				2000
$\sqrt{s}$ (GeV)	189	192	196	200	202	204-209
$\mathcal{L}$ (pb^{-1})	158	25.9	76.9	84.3	41.1	163.4

Table 3.1: The integrated luminosities, $\mathcal{L}$, for the various years of LEP2 data-taking, expressed in units of pb^{-1}. The corresponding centre-of-mass energies are also given.

3.2 The DELPHI detector

DELPHI (DEtector for Lepton Photon and Hadron Identification) is one of the four multipurpose detectors situated around the LEP ring. Its main functions are particle tracking, calorimetry, particle identification, precise vertex determination and muon detection. The detector was installed in a cavern 100 m below ground and consists of a cylindrical section and two end-caps. Besides the subsystems used for particle detection a superconducting solenoid with a length of 7.4 m and a diameter of 5.2 meter, providing a homogeneous field of 1.2 T is included for precise momentum determination.

Since the analysis is mainly based on manipulating individual tracks, most emphasis will be given here to the description of the DELPHI subsystems involved in tracking. For a full description of the DELPHI detector and its performance, see [57, 58].

The DELPHI coordinate system is defined as a right-handed orthogonal set of three axis, having its centre in the nominal interaction point. The z axis points along the flight direction of the electrons, the x axis in the horizontal plane towards the centre of LEP and the y axis points upwards. A schematic drawing of the DELPHI detector, indicating its main detector systems is given in Fig. 3.2.

3.2.1 Tracking chambers

Vertex Detector

The Vertex Detector (VD) is the detector situated closest to the beam pipe. Its main objective is to provide maximum $R\phi$-resolution, important for heavy flavor physics and vertex reconstruction in general. R is the distance to the beam axis, ϕ the azimuthal angle around it and θ the polar angle w.r.t. the z axis. It consists of three coaxial cylindrical layers of silicon strip detectors at average radii of 6.3, 9.0 and 10.9 cm. Each layer covers the full azimuthal angle, while only tracks with a polar angle of $25° \leq \theta \leq 155°$ cross all three layers of the detector. The single hit precision in the Rϕ plane is 7.6 μm for one layer. For the z coordinate, the single-hit precision is a function of the incidence angle of the track, reaching a minimum value of 9 μm for tracks perpendicular to the VD modules.

Inner Detector

The ID provides high redundancy for vertex reconstruction and trigger information. It consists of an inner jet-chamber, surrounded by 5 cylindrical layers of straw tube detectors. The jet chamber consists of 24 azimuthal sectors, each providing up to 24 $R\phi$ measurements per track between radii of 12 and 23 cm. The polar angle acceptance for tracks giving a hit on the 10 innermost anode wires is $15° \leq \theta \leq 165°$. The two track resolution is about 1mm. The straw tubes provide additional $R\phi$ measurements, mainly used in triggering and in resolving left/right ambiguities inherent in the jet-chamber. During the LEP2 running period the ID did not provide any z-coordinate measurement.

Time Projection Chamber

The TPC is the most important tracking device of DELPHI. Pattern recognition normally starts from its information. It provides also additional dE/dx information, useful for e-π separation below 8 GeV. The TPC consists of two gaseous drift volumes, separated by a high tension plate, producing an electric field of 150 Volts/cm. A charged particle crossing the TPC produces by ionisation around 70 electrons per cm of gas. Under the action of the electric field these primary electrons drift in the direction of 6 proportional chambers at the two extremities of the chamber, responsible for the amplification of the ionisation signal. Each of the 6 azimuthal chambers contains 192 sense wires and 16 circular pad rows with constant spacing. The detector thus provides a maximum of 16 space points per track at a distance between 40 and 110 cm perpendicular to the beam direction , provided that its polar angle lies between $39° \leq \theta \leq 141°$. The single point precision obtained from $Z \rightarrow \mu^+\mu^-$ decays is 250 μm in the $R\phi$ plane and 880 μm in the Rz plane. As the size of the TPC is limited by the presence of the RICH detectors, more track chambers are added to improve momentum resolution (see below).

Outer Detector

The OD is essential to provide fast trigger information and serves as an extra lever arm to improve the momentum resolution for fast particles. It is composed of 5 layers of drift tubes, operating in limited streamer mode, located between radii of 197 and 206 cm, giving full azimuthal coverage. All layers provide $R\phi$ information while three layers are equipped to read the z coordinate by timing the signals at the ends of the anode wires. The geometrical acceptance corresponds to polar angles between $42° \leq \theta \leq 138°$. The respective single point precisions in the $R\phi$ plane and for the z coordinate are 110 μm and 3.5 cm.

Forward Chamber A

The FCA is situated in both end caps of the detector and provides tracking and triggering in the angular region between $11° \leq \theta \leq 32°$ and $148° \leq \theta \leq 169°$. Its three modules are mounted on each end of the TPC at a distance from the interaction point of about 160 cm. A module consists of two staggered layers of drift tubes which are operated in limited streamer mode. The orientation of the wires in the three modules are rotated over $120°$ w.r.t. each other. The polar angle precision for reconstructed track elements is 8.5 mrad and 24 mrad for the azimuthal angle.

Forward Chamber B

The FCB is a drift chamber situated at a distance of 275 cm from the interaction point, consisting of 12 readout planes, and providing 4×3 coordinate measurements, used for triggering and pattern recognition. This detector substantially improves the momentum resolution in the forward region. The sensitive area of the chamber corresponds to polar angles of $11^\circ \leq \theta \leq 36^\circ$ and $144^\circ \leq \theta \leq 169^\circ$. The respective track element precisions in θ and ϕ are 3.5 mrad and $4.0/\sin\theta$ mrad. in polar and azimuthal angle. The precision of the x,y measurement is 150 μm.

3.2.2 Momentum Precision

The precisions obtained on particle momenta can be derived from $Z^0 \rightarrow \mu^+\mu^-$ decays where both muons should have equal and opposite momenta. The widths of the (1/p) distribution for particles traversing different tracking detectors are summarised in Tab. 3.2. The precision on track parameters at other momenta can be estimated comparing simulated and reconstructed tracks in a sample of generated hadronic Z^0 decays. Data on several track parameter resolutions can be found in [58].

$\theta(\,^\circ)$	Detectors	$\sigma(1/\mathrm{p})(\mathrm{GeV/c})^{-1}$
≥ 42	VD+ID+TPC+OD	0.6×10^{-3}
≥ 42	ID+TPC+OD	1.1×10^{-3}
≥ 42	VD+ID+TPC	1.7×10^{-3}
≤ 36	VD+FCB included	1.3×10^{-3}
$25 - 30$	FCB included	1.5×10^{-3}
< 25	FCB included	2.7×10^{-3}

Table 3.2: Precision on the inverse momentum, obtained from 45.6 GeV/c muons.

3.2.3 Electromagnetic Calorimeters

DELPHI includes two main electromagnetic calorimeter systems, one in the barrel region, the HPC (High Density Projection Chamber), and the FEMC (Forward Electromagnetic Calorimeter) located in both end caps. In addition there are two luminosity monitors, the STIC (Small Angle Tile Calorimeter) and the VSAT (Very Small Angle Tagger). Supplementary photon taggers have been installed in gaps between the HPC and the FEMC, mainly used by searches analysis. DELPHI also contains a Time-of-Flight (TOF) scintillating counter system, serving as fast trigger for beam events and cosmics. Other uses are tagging of particles escaping through gaps between the DELPHI sub-detectors.

High Density Projection Chamber

The aim of the HPC is to measure the three dimensional charge distributions induced by e.m. showers and hadrons with a very high granularity. It consists of 144 modules situated in the magnetic field of the solenoid at radii between 208 and 260 cm away from the beam. Each module is in principle a small TPC with layers of high density material inside the gas volume, acting as absorber. The energy resolution obtained from $Z \rightarrow e^+e^-$ processes and neutral pion decays can be parametrised as $\sigma(E)/E = 0.043 + 0.32/\sqrt{E}$.

Forward Electromagnetic Calorimeter

The FEMC consists of two 5 m diameter disks with a total of 9064 lead glass blocks pointing toward the interaction point. They cover the polar angle region of $8° \leq \theta \leq 35°$ and $145° \leq \theta \leq 172°$. The scintillation light produced by the charged particles in the shower is read out by photomultipliers to extract the energy information. The energy resolution of this device can be determined by means of Bhabha events. The relative precision on the measured energy can be parametrised as $\sigma(E)/E = 0.03 + (0.12/\sqrt{E}) + (0.11/E)$.

Electron and Photon identification

Electron identification is performed using combined information from the electromagnetic calorimeters and the dE/dx measurement from the TPC. After corrections and calibrations the E/p ratio is expected to be close to unity for electrons, this ratio is therefore parametrised and converted into a probability for the electron hypothesis. The deviation of the cluster coordinates from an extrapolated TPC track leads to a further $\mathrm{e} - \pi$ separation. All this, combined with a probability variable describing the electromagnetic character of a shower profile is complemented by the dE/dx measurement of a particle traversing the TPC. Finally three levels of tagging are available ranging in efficiencies from 80 to 45 % with corresponding misidentification probabilities of 1.6 to 0.2 %.

Photons are identified by means of their conversion signature in $\mathrm{e}^+\mathrm{e}^-$ pairs or by summing neighbouring electromagnetic showers which are not associated to a charged track.

Luminosity detectors

In DELPHI two detectors are used to measure the Luminosity, the STIC and the VSAT. The process chosen to calculate the luminosity is the Bhabha scattering at small angles, which has a high cross section and is theoretically well known. The absolute luminosity is measured by the STIC calorimeter, while the VSAT measures relative luminosities with a very high precision, thus acting as a cross check for the STIC measurements. The overall experimental precision of the luminosity measurement amounts to 0.5%.

Hadronic Calorimeter

The HCAL is a sampling gas detector installed in the return yoke of the solenoid which acts as absorber. The barrel section and its two end caps almost cover the full solid angle: $11° \leq \theta \leq 169°$. In total, the HCAL consists of more than 19,000 limited streamer tubes and is calibrated using muons coming from $Z \to \mu^+\mu^-$ decays. In the barrel region, the energy precision is given by $\sigma(E)/E = 0.21 + 1.12/\sqrt{E}$.

Muon Chambers

The DELPHI muon system consists of a barrel muon section (MUB) and two forward muon detectors (MUF), the latter were constructed and maintained by the Belgian groups. Both are composed of drift chambers, the MUB operating in proportional mode, the MUF operating in limited streamer mode. The resolution of the coordinate measurements perpendicular to the wires amounts to 3-4 mm for both systems. The MUB provides also a measurement along the wires with a resolution of 2.5 cm. An additional set of surround muon chambers (MUS) was added later during DELPHI running to cover the gaps between the barrel region and the end-cap region. The principles of operation of this system are similar to MUB and MUF. The iron of the return yoke and hadron calorimeter provides a first filter to separate muons from hadrons. Most hadrons are stopped by this material while muons with momenta larger than 2 GeV/c will give hits in the muon chambers. A residual background remains however due to punch-trough of hadronic showers, hadronic decays in flight and particles traversing cracks and boundaries in the detector. The first two backgrounds can be reduced since those signals will give generally larger deviations from the track extrapolation than are expected from multiple scattering of a muon. In DELPHI, four muon tags are used ranging in efficiencies from 96% to 76% and in misidentification probabilities from 5.4% to 0.4%.

Ring Imaging Cherenkov detector

The ability of superior hadron identification makes DELPHI unique among the four LEP experiments. The RICH detectors are based on the detection of Cherenkov light emitted by a particle traversing a dielectric medium with a speed faster than the speed of light in that medium. The mass M and the momentum p of a particle are related to the emission angle θ_c according to $\cos\theta_c = 1/n \times \sqrt{1 + M^2/p^2}$ where n is the refractive index of the medium. The RICH detector covers a momentum range between 0.7 and 8 GeV/c with a liquid radiator, while the momentum range between 2.5 and 25 GeV/c is covered by a gas radiator. The RICH systems in the forward region (FRICH) and barrel region (BRICH) cover the full solid angle between 40° and 140°. Cherenkov photons are focused by parabolic mirrors onto photosensitive time projection chambers. Several algorithms have been developed to perform pion, kaon and proton separation, and are not used in this work.

3.2.4 Data processing and simulation

When LEP is in physics collision conditions, its beams cross each other every 22 μs, resulting in an event rate which would be too high to process, let alone to store. Therefore a series of trigger levels are defined to select events which are kept for further analysis. This trigger consists of two hardware levels, which make their decisions on-line and two off-line software triggers. The rate of events collected and stored after the fourth trigger level is around two events per second. For all these events the DELPHI data acquisition system collects the raw data from each sub-detector and stores them on tape for further analysis.

Information about the running conditions of the detectors and relevant information on the beam conditions are stored in a database. The information in this raw data is analysed by the DELPHI reconstruction software DELANA [59], which reconstructs particles by applying pattern recognition and track fitting algorithms to combine the information obtained from all sub-detectors. Some particle identification is done already at this stage and a basic event classification is performed. This information is stored on magnetic tape for further analysis by the users. The DELPHI software packages PHDST [60] and SKELANA [61] provide a further convenient framework for the physics analysis. The DELphi SIMulation program (DELSIM) [62] simulates the response of the DELPHI detector and the interactions of particles with its material. It uses as input simulated particles from Monte Carlo generators and generates an output in the same format as real data, which can be analysed by DELANA.

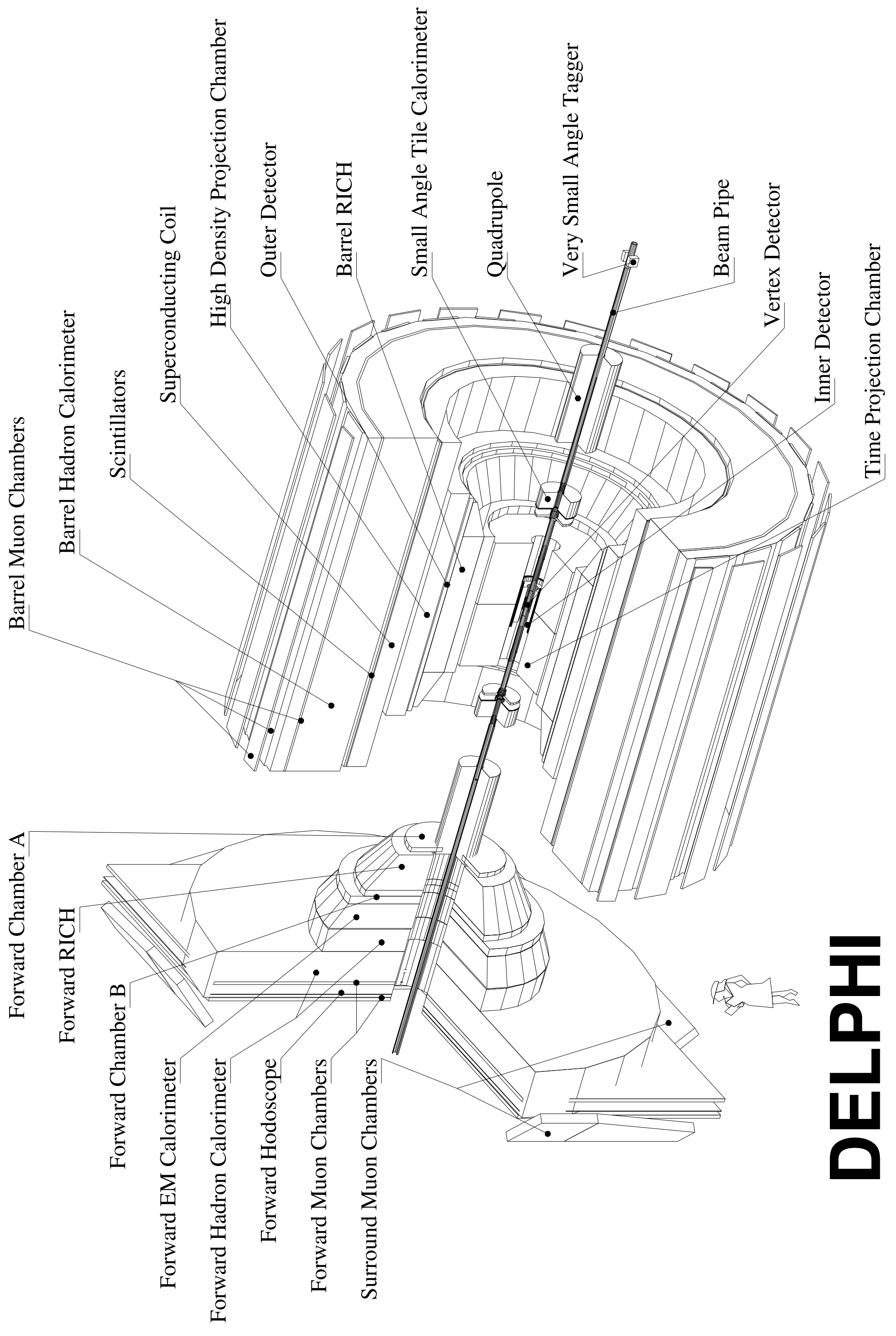

Figure 3.2: A schematic drawing of the DELPHI detector. The main sub-detector systems are indicated.

Chapter 4

Bose-Einstein correlations in $\mathrm{W}^+\mathrm{W}^-$ events

Correlations between final state particles in high energy collisions have been extensively studied since the Goldhaber et al. experiment [9, 10] and were briefly reviewed in Chpt. 1. They can be due to phase space, energy-momentum conservation, resonance production, hadronisation mechanisms, or are dynamical in nature. In the particular case of identical bosons the correlations are enhanced by the Bose-Einstein effect. These Bose-Einstein Correlations (BEC) are a consequence of quantum statistics. The net result is that multiplets of identical bosons are produced with smaller energy-momentum differences than non-identical ones.

In this chapter, Bose-Einstein correlations between bosons originating from different W's in the reaction $e^+e^- \rightarrow W^+W^- \rightarrow q_1\bar{q}_2q_3\bar{q}_4$[1] will be investigated. This topic has recently become of high interest in the framework of the precise determination of W boson mass. If Bose-Einstein correlations between different W's (inter-W BEC) are observed, one can no longer assume that the two W bosons in the reaction $e^+e^- \rightarrow W^+W^- \rightarrow q_1\bar{q}_2q_3\bar{q}_4$ decay independently. This induces a systematic uncertainty on the W mass when measured in this decay channel. In addition, observation of inter-W BEC is of high interest for our understanding of hadronisation models, since, at present, all assume an independent hadronisation of the W decay products.

The structure of this chapter is as follows. First, we expand on the relevance of measuring inter-W BEC. The main characteristics of the reaction $e^+e^- \rightarrow W^+W^-$ are given in Sect. 4.2, together with a description of the main background processes. Hereafter, the analysis method is described, followed by an overview of the procedures to select W^+W^- events. Using the particles from these selected events, two-particle densities will be constructed. They will contain all information about inter-W BEC. The treatment of background contamination and the construction of a reference sample without inter-W BEC require special attention. This is discussed in Sects. 4.5.1 and 4.5.2. The statistical treatment of two-particle densities is important in order to quantify the significance of our result. Section 4.5.2 explains how all statistical uncertainties should be correctly taken into account. A technique, based on giving weights to particle pairs which are more likely to originate from differ-

[1]The symbol q_i denotes a quark of flavor i, where i can correspond to the up, down, charm, strange and bottom flavor. The symbol $\bar{q}_j$ corresponds to an anti-quark of flavor j.

ent W's, will improve the sensitivity of our measurement. This technique is described in Sect. 4.7.2. We conclude with a discussion of the results, where we make a comparison with data from other LEP experiments and give an estimate of the systematic uncertainty on the DELPHI W mass measurement.

4.1 Relevance of the analysis

In Sect. 1.2 an overview was given of Bose-Einstein correlations in various reactions, and in particular in the reaction $e^+e^- \to Z^0$. There is no reason why Bose-Einstein correlations should not be present in $e^+e^- \to W^+W^-$ events. After all, as far as hadronisation is concerned, there is not much difference between the hadronic decay of a W boson and that of a Z^0 boson, since both decay into a quark and an anti-quark.

The life-time of a W boson is very short. The average proper life-time of a W, $\langle\tau\rangle$, depends on its mass according to

$$\langle\tau\rangle = \frac{\hbar m}{\sqrt{(m^2 - m_W^2)^2 + (\Gamma_W m^2/m_W)^2}}, \tag{4.1}$$

where m_W and Γ_W are the nominal W boson mass and width and $1 = \hbar \approx 0.197$ GeV$\cdot$ fm. For a W boson with nominal mass, this reduces to the standard expression, $\tau(m_W) = \hbar/\Gamma_W \approx 0.1$ fm. However, with a standard Breit-Wigner distribution of masses, the W life-time is only about two thirds as long as the naive expectation. Compared to the emission source sizes measured in e^+e^- interactions, which are of the order of 0.5 –1 fm, this flight distance is small. Therefore, it is natural to expect a large space-time overlap between the decay products of the W's and thus allowing correlations of the BE type between identical bosons originating from different W's to exist.

Together with colour reconnection [63, 64], the poor understanding of the inter-W BEC effect introduces large systematic uncertainty in the measurement of the W mass in the channel $e^+e^- \to W^+W^- \to q_1\bar{q}_2q_3\bar{q}_4$ [51]. The current statistical uncertainty of the combined LEP measurement in this channel amounts to 36 MeV [65], to be compared with the total systematic uncertainty in this channel of 101 MeV. The effect of possible inter-W BEC amounts to 35 MeV. It is thus clear that a better understanding of the inter-W BEC phenomenon would help in reducing this uncertainty.

The precise measurement of the W mass is one of the main goals of the LEP2 physics program [66]. Together with the mass of the top quark and the mass of the undiscovered Higgs boson, it is one of the key parameters of the Standard Model (SM). Complementary to a direct search for the Higgs boson, the measurement of the W mass and top quark mass can put indirect limits on the Higgs boson mass, thus giving an indication of the energy threshold where the Higgs boson could be produced.

The relation between the different SM parameters is demonstrated by the theoretical expression for the Fermi coupling constant G_μ, which is accurately measured from the decay of the muon:

$$G_\mu = \frac{\alpha\pi}{\sqrt{2}m_W^2(1 - m_W^2/m_Z^2)}\frac{1}{1-\Delta r}, \tag{4.2}$$

where α is the fine structure constant and m_W and m_Z are the W and Z^0 boson masses, respectively. In this expression, $\Delta r = 0$ at tree level. However, due to loop corrections Δr is a function of the top quark mass and that of the Higgs boson. The above relation predicts for any chosen Higgs mass M_H and measured W mass M_W a value for the top mass m_t that can be used as an input for LEP2 loop calculations and can be compared with direct top quark measurements.

In addition to its impact on the W mass measurement, the observation of an inter-W BEC signal would be of interest to the understanding of hadronisation models, describing the non-perturbative QCD aspects of hadron production. At present, it is not clear how inter-W BEC can be understood in the framework of these models. Different BEC models, predicting widely different effects on the W mass measurement [51, 50, 66] vary considerably.

4.2 The reaction $\mathrm{e^+e^-} \rightarrow \mathrm{W^+W^-}$ and its background processes

In its first stage of operation LEP was running at a centre-of-mass energy corresponding to the mass of the Z^0 boson, $\sqrt{s} \approx 91.2$ GeV. In the LEP2 stage, the centre-of-mass energy was increased to 161 GeV, in order to produce the W boson which is produced in pairs in e^+e^- annihilations. Throughout the years 1996-2000, the centre-of mass energy was steadily raised to the record energy of 209 GeV.

In what follows, the main characteristics of the reaction $\mathrm{e^+e^-} \rightarrow \mathrm{W^+W^-}$ will be discussed. The three possible decay modes of the W^+W^- system will be described, whereafter it will be shown that other processes, some having a similar or even larger cross-section than the W^+W^- production, require a dedicated strategy to separate them from the signal W^+W^- events.

At tree level, the calculation of on-shell W-pair production in e^+e^- annihilations is described by the diagrams given in Fig. 4.1. The first diagram in this figure corresponds to the t-channel exchange of an electron-neutrino and is dominant near the W-pair production threshold energy. The second diagram describes the s-channel exchange of a virtual Z^0 or photon, γ, which allows in addition to the determination of the W mass a study of the gauge couplings between the W, γ and the Z^0.

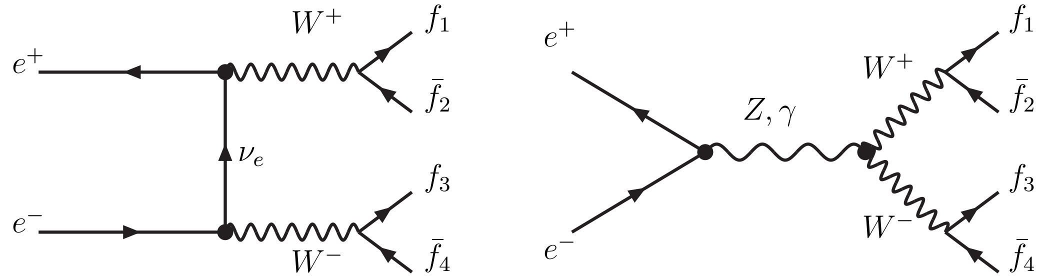

Figure 4.1: The two lowest-order diagrams for $e^+e^- \rightarrow W^+W^-$. Note that the diagram on the right has two contributions, one from the Z boson and one from the photon γ.

Each of the W's decays into two fermions (particles with half-integer spin), resulting in a four fermion final state. Only a restricted amount of decays is possible. A W can either decay into one of the three lepton species and its corresponding (anti)-neutrino or into a quark-antiquark pair ($q_1\bar{q}_2$) resulting in a total net charge of either +1 or -1, depending on the charge of the W. An overview of the quark and lepton generations and their relevant properties is given in Tab. 4.1. For this reason, the final states of a decaying pair of W's are

Fermions	Generation 1		Generation 2		Generation 3		Q	I_3 (left-handed)
Leptons	ν_e		ν_μ		ν_τ		0	1/2
	e^-	(electron)	μ^-	(muon)	τ^-	(tau)	-1	-1/2
Quarks	u	(up)	c	(charm)	t	(top)	2/3	1/2
	d	(down)	s	(strange)	b	(bottom)	-1/3	-1/2

Table 4.1: The three generations of leptons (further denoted l) and quarks (further denoted q) in the Standard Model. Their quantum numbers corresponding to their electric charge, Q and the third component of the weak isospin, I_3, for the left-handed chirality state. All particles have their corresponding anti-particles (denoted $\bar{l}$ and $\bar{q}$, with opposite charge and third isospin component.

categorised in three classes:

- **fully hadronic**: Both W's decay into a quark-antiquark pair, further denoted as the $4q$ mode.

$$e^+e^- \to W^+W^- \to q_1\bar{q}_2q_3\bar{q}_4,$$

- **semi-leptonic**: One of the W bosons decays in a lepton-(anti)neutrino pair, while the other W decays in a quark-antiquark pair, further denoted as the $2q$ mode.

$$e^+e^- \to W^+W^- \to q_1\bar{q}_2 l\bar{\nu_l}(\mathrm{l} = \mathrm{e}, \mu, \tau),$$

- **fully-leptonic**: Both W's decay in a lepton-(anti)neutrino pair.

$$e^+e^- \to W^+W^- \to \bar{l_1}\nu_{l1}l_2\bar{\nu_{l2}}(\mathrm{l} = \mathrm{e}, \mu, \tau).$$

Only the first two processes are relevant for the work described in this thesis. The Standard Model predicts branching ratio's of 45.6% for the $4q$ channel and 43.9% for the $2q$ channel.

The fully-hadronic decays are characterised by a large amount of visible energy in the detector and a clear four- (or more) jet topology.

The semi-leptonic events are characterised by missing energy and momentum due to the undetected neutrino, a clear isolated track or narrow jet, attributed to the lepton and two separated jets corresponding to the hadronisation of the $q\bar{q}$ pair. Fig. 4.2 shows a selected fully-hadronic WW candidate, having a clear four-jet topology and a semi-leptonic candidate showing an imbalance in momentum and a track being tagged as a muon, due to its detection by the forward muon chambers.

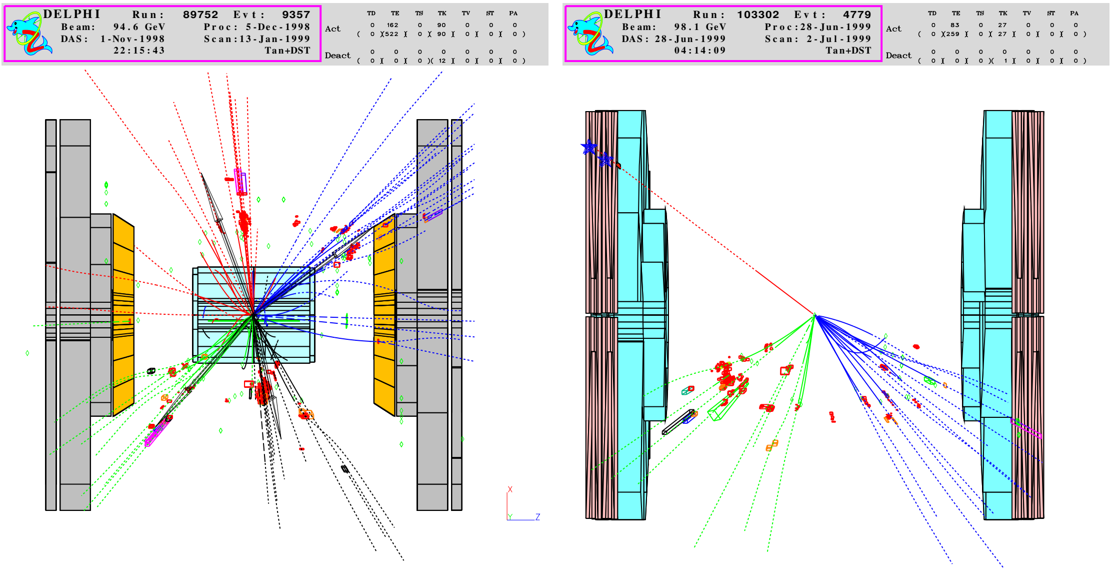

Figure 4.2: Two reconstructed WW candidates, recorded by the DELPHI detector. The picture on the left shows a fully-hadronic WW decay, with a clear four-jet topology. The picture on the right shows an imbalance in momentum, an isolated muon, giving hits in the forward muon chambers and two isolated jets.

As seen in Fig. 4.3 the cross-section for W pair production rises steeply at the threshold energy of 161 GeV. In the energy range from 189 to 207 GeV, the cross-section is $\approx 16-18$ pb. In the same figure, the cross-sections are shown for many other electroweak processes.

The most dominant background for both fully-hadronic and semi-leptonic events is the process $e^+e^- \rightarrow q\bar{q}(\gamma)$, denoted by the dashed line in Fig. 4.3. It has a cross-section decreasing from 99.4 pb and 77.8 pb in the energy range between 189 and 207 GeV. In this process, the incoming electron or positron radiates a photon before the interaction takes place, therefore reducing the available centre-of-mass energy to create a W^+W^- pair. The resulting final state is an event with two hadronic jets, and an amount of missing momentum and energy due to the radiated photon, which escapes through the beam pipe in most of the cases. If the original produced quarks radiate hard gluons, this can result in a multi-jet final state, very similar to a fully-hadronic WW decay. The semi-leptonic WW events are further contaminated by the $e^+e^- \rightarrow Z^0Z^0 \rightarrow q\bar{q}l\bar{l}$ and $e^+e^- \rightarrow Z^0e^+e^- \rightarrow q\bar{q}e^+e^-$ processes. The first process is characterised by the presence of two detected leptons of the same flavour, while in the latter the electron or the positron often escape through the beam pipe.

All processes leading to a four-fermion final state (including the signal WW events) are (in DELPHI) generated by means of the WPHACT generator [67]. It is based on a state-of-the-art description of the 4-fermion processes, including charged current, neutral current and mixed current diagrams, the generation of Initial State Radiation with finite transverse momentum and an optimised phase space coverage. The $q\bar{q}(\gamma)$ process is generated by the KK2f generator [68].

Dedicated signal and background samples were generated including Bose-Einstein correlations. These samples include the LUBOEI BE_{32} implementation of the Bose-Einstein ef-

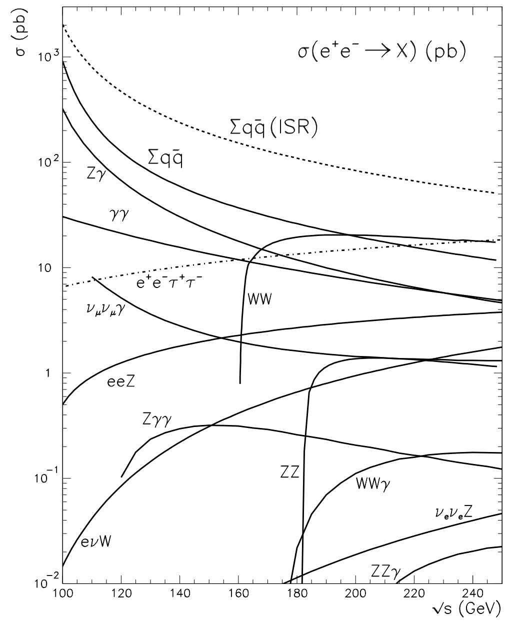

Figure 4.3: Cross-sections for the most typical standard electroweak processes at LEP2 energies. Only the most dominant diagrams are taken into account. Plot adopted from [66].

fect. The input parameters PARJ(92) and PARJ(93) as they are defined in the JETSET code, were tuned to the DELPHI data, as was shown in Sect. 2.3.2. Their values are PARJ(92)=1.35 and PARJ(93)=0.34 GeV^{-1}=0.6 fm. Two different options are considered: the model where Bose-Einstein correlations are switched on for the whole event, further denoted as the BEfull sample and the model where Bose-Einstein correlations only occur inside a single W and not between the different W's, further denoted as the BEins model.

An alternative tuning for the $q\bar{q}(\gamma)$ events exists, having parameter PARJ(92)=0.9. The use of this alternative tuning is explained later.

4.3 Analysis method

Two particle correlation functions and normalised densities have already been defined and discussed in Chpt 1. The separation of inter-W Bose-Einstein correlations from the correlations inside a W needs an extension of the formalism from Sect. 1.1.1.

We know that even if no inter-W correlations are present, we will measure a non-zero correlation function in fully hadronic WW decays, due to the fact that particles coming from the same W are subjected to BEC.

References [69] and [22] provide an elegant solution. In the case of two stochastically independent hadronically decaying W's, the single and two-particle inclusive densities obey the following relations:

$$\begin{aligned} \rho^{WW}(1) &= \rho^{W^+}(1) + \rho^{W^-}(1), \\ \rho^{WW}(1,2) &= \rho^{W^+}(1,2) + \rho^{W^-}(1,2) + 2\rho^{W^+}(1)\rho^{W^-}(2), \end{aligned} \tag{4.3}$$

where $\rho^W(1)$ denotes the inclusive single particle density of one W and $\rho^W(1,2)$ the inclusive two-particle density of one W. The densities $\rho^{WW}(1)$ and $\rho^{WW}(1,2)$ then correspond to the single, resp. two-particle inclusive density of a fully hadronic WW event. Equation 4.3 differs from the sum of two-particle densities for each independent W taken separately by the term $2\rho^{W^+}(1)\rho^{W^-}(2)$. Assuming that the densities for the W^+ and the W^- are the same, Eq. 4.3 can be re-written as

$$\rho^{WW}(1,2) = 2\rho^{W}(1,2) + 2\rho^{W^+}(1)\rho^{W^-}(2). \tag{4.4}$$

The terms $\rho^{WW}(1,2)$ and $\rho^{W}(1,2)$ can be measured in, respectively, fully-hadronic and semi-leptonic WW decays. The product of the single particle densities $\rho^W(1)\rho^W(2)$ is, in practical applications, replaced by a two-particle density ρ^{WW}_{mix}, obtained by combining particles from two hadronic W decays taken from different semi-leptonic events. The details of this "mixing" procedure are explained later. Expressed in the variable $Q = \sqrt{-(p_1 - p_2)^2}$, Eq. 4.4 can be re-written as

$$\rho^{WW}(Q) = 2\rho^{W}(Q) + 2\rho^{WW}_{\text{mix}}(Q). \tag{4.5}$$

Experimentally, the factor 2 in front of $\rho^{W^+}(1)\rho^{W^-}(2)$ is accommodated for automatically since two W's from different semi-leptonic events are mixed, irrespective of their electrical charge.

Keeping in mind that Eq. 4.3 was formulated for independent W decays, one can construct test observables to look for deviations from this assumption. Such deviations will signal that particles from different W decays do correlate. The observables considered are:

$$\Delta\rho(Q) = \rho^{WW}(Q) - 2\rho^{W}(Q) - 2\rho^{WW}_{mix}(Q), \tag{4.6}$$

$$D(Q) = \frac{\rho^{WW}(Q)}{2\rho^{W}(Q) + 2\rho^{WW}_{mix}(Q)}, \tag{4.7}$$

Any deviation from zero of $\Delta\rho(Q)$, or any deviation from one of $D(Q)$, indicates the presence of inter-W BEC. Note that the integral of $\Delta\rho(Q)$ over the whole Q range corresponds to the covariance of the charge multiplicity distribution[2] of one W and that of the second W [22]. Therefore it vanishes in the absence of inter-W correlations.

In order to establish a possible inter-W BEC effect, one possibility is to integrate the distribution $\Delta\rho(Q)$ over a given Q interval. Alternatively, $D(Q)$ can be fitted with e.g. an exponential parametrisation of the form:

$$D(Q) = N(1 + \Lambda e^{-RQ})(1 + \delta Q). \tag{4.8}$$

[2]This is the distribution of the number of charged particles in the event.

The parameter Λ is a measure of the strength of the Bose-Einstein correlations between different W's. The parameter R is a measure of the space-time overlap between the two W's.

The measurement of $\Delta\rho(Q)$ and $D(Q)$ proceeds in the following way. Firstly, fully-hadronic and semi-leptonic WW events have to be selected from the total data sample collected by the DELPHI detector. After this, the analysis splits up into two parts, corresponding to the treatment of both event classes.

The fully-hadronic event sample is contaminated by background from the process $e^+e^- \rightarrow q\bar{q}(\gamma)$. The strength of the Bose-Einstein effect in this background is not known. Therefore, it has to be modeled using a Monte Carlo model, including BEC. After modeling BEC inside this background sample, it will be subtracted from the real data. The systematic uncertainty due to the modeling of the background will, evidently, be smaller when the background fraction is reduced. This can be accomplished by a more stringent selection of fully-hadronic WW events, resulting in a smaller number of selected signal events and, consequently, a reduction of the statistical precision. This cost-benefit exercise will be optimised choosing a selection giving the smallest total uncertainty.

In the semi-leptonic events, the hadronically decaying W has to be separated from the rest of the event. Its total momentum, energy and direction has to be precisely determined, in order to combine it properly with another W. At this stage, the tracks of the two independent W's are mixed, and a new WW event is constructed. Finally, the same selection procedure as is applied to the true fully-hadronic event, will be also applied on the "mixed" events.

4.4 Selection of WW events

In this section, it will be explained how the fully-hadronic and semi-leptonic WW decays are separated from the background processes mentioned in Sect. 4.2. For a detailed overview of the selection cuts and procedures we refer to App. B. The total analysed dataset used in this thesis amounts to 549.6 pb^{-1}, collected with the DELPHI detector during the years 1998-2000. A summary of the total amount of integrated luminosity per energy point is given in Tab. 3.1.

Firstly, some basic tools concerning the event reconstruction are discussed. After explaining these techniques, the selection of fully-hadronic and semi-leptonic events by means of a neural network will be briefly discussed.

4.4.1 Analysis tools

In order to select fully-hadronic and semi-leptonic events from the total data sample, some basic properties of the events have to be calculated. In the case of selecting WW events, two techniques are of main importance:

- **Jet clustering**, in order to identify and analyse the hadronic decay products of a W boson;

- **A constrained fit**, to improve the measurement of the invariant mass beyond the detector resolution, using the knowledge of the initial e^+e^- state.

Jet Clustering

When a primary quark (or anti-quark) radiates soft gluons which evolve according to the parton shower scheme, the transverse momentum of each daughter particle w.r.t. its mother particle decreases rapidly. Therefore the final state hadrons, originating from a primary quark are not distributed uniformly in space, they are collimated around the original flight direction of the quark and have a “jet”-like structure. This can be seen in Fig. 4.2. Experimentalists want to calculate the original quark momentum and energy from the energy and momenta of all final state hadrons observed in th detector. For this purpose, jet clustering algorithms are used. In addition, in the analysis of fully-hadronic events, it is important to know which particles originate from which W. The assignment of particles to a given W is, therefore, easier when they are already grouped in jets.

All jet clustering algorithms merge pairs, or triplets, of particles successively in function of an increasing distance measure or resolution variable. The merging is done according to a so-called recombination scheme, i.e. the way in which the energy and momentum of jets are computed from the original four-momenta of the particles. This procedure is repeated until a pre-defined resolution or a desired number of jets is obtained. In the LUCLUS [47] clustering scheme, the resolution variable

$$y_{ij} = \frac{2|\overrightarrow{p_i}||\overrightarrow{p_j}|\sin(\theta_{ij}/2)}{|\overrightarrow{p_i}| + |\overrightarrow{p_j}|} \tag{4.9}$$

is computed for each particle pair. The particle pair with the smallest y_{ij} value is, when y_{ij} is smaller than a given pre-defined value of y_{cut}, combined into a pseudo-particle. The four-momentum of this pseudo-particle is simply the sum of the individual four-momenta ($p_k = p_i + p_j$). This procedure is repeated iteratively until no pair has a value of y_{ij} smaller than the value of y_{cut}. The number of objects is then identified with the number of free jets. When the value of y_{cut} is set to an arbitrary large value, it is also possible to force the event in a pre-defined number of jets, the smallest y_{ij} value of the last iteration is then a measure for the separation of the jets. The DURHAM [70] algorithm, as it was used in the reconstruction of hadronic WW events, has the same recombination scheme, but an alternative definition of y_{ij}:

$$y_{ij} = \frac{2\text{min}(E_i^2, E_j^2)(1 - \cos\theta_{ij})}{s}, \tag{4.10}$$

where $E_{i,j}$ is the energy of the particles i and j and s the centre-of-mass energy squared. An example of the DURHAM jet resolution variable y_{34}, corresponding to the minimum distance between the jets in a four-jet topology, is given in Fig. 4.4. It shows that for fully-hadronic events the minimum separation between the jets, after clustering the event into four jets, is larger in the signal events than in the background events.

The constrained fit

For an ideal detector, the estimation of the jet energies and momenta would reproduce accurately the true parton momentum and energy. However, in jets around 15% of the total

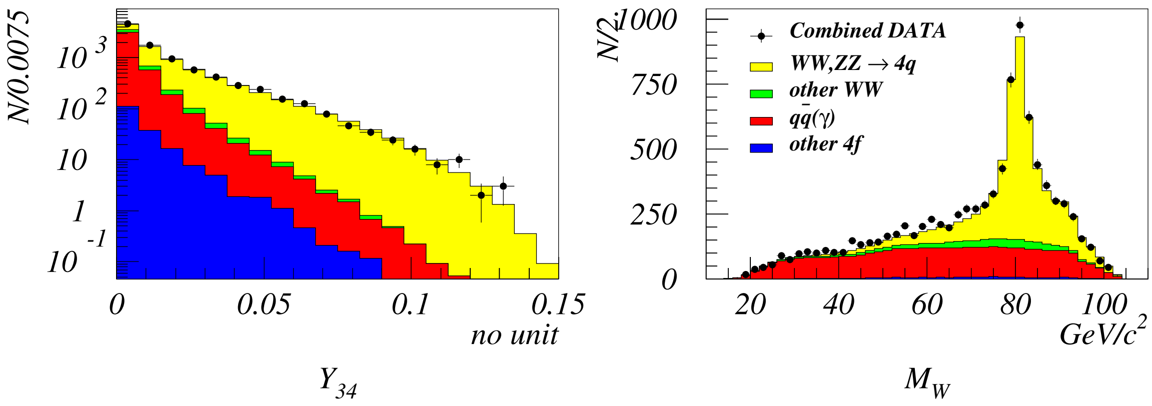

Figure 4.4: (left) The y_{34} variable from the DURHAM algorithm, for events clustered into four jets. (right) The reconstructed W mass M_W, using a constrained fit, imposing the two di-jet masses to be equal. The signal and background processes are shown by the light and the dark shaded histograms, respectively. It is seen that the $q\bar{q}(\gamma)$ process is the most dominant background.

energy is not reconstructed. This is due to the presence of undetected neutrino's, particles escaping the detector, the intrinsic resolutions of the calorimeters, etc.

In contrast to this, the initial e^+e^- state is accurately known. The beam energy is known up to a precision of better then one per mille and the momenta are perfectly balanced in absence of initial state QED radiation (ISR).

One can therefore subject the jet energies and momenta to a fit with the following four constraints:

$$\sum_{i}^{n_{\text{jets}}} (p_1^i, p_2^i, p_3^i, E^i) = (0, 0, 0, \sqrt{s}), \tag{4.11}$$

where $p_j^i, j = 1, 3$ are the momenta of the jets, E^i their energies and $\sqrt{s}$ the centre-of-mass energy.

This fit is known as a 4C fit, since four constraints are to be satisfied. In the case of semi-leptonic decays, containing a neutrino in the final state ($W^+W^- \to q\bar{q}l\nu_l$), three constraints are "absorbed" in the fit.

Under the assumption that the jets (or jets + lepton and missing momentum) originate from two decaying W's, additional constraints can be introduced. These additional constraints are related to the reconstructed di-jet masses. Both masses can be constrained to be equal to each other and, in addition, equal to the nominal W mass. These fits are called a 5C and 6C fit, respectively. An example of the reconstructed di-jet mass, using a 5C fit is shown in Fig. 4.4.

The constrained fit is implemented in DELPHI inside the PUFITC package [71]. The χ^2 of the fit is defined in the usual way:

$$\chi^2 = \sum_{i}^{n_{\text{jets}}} \frac{(y_i^{\text{fit}} - y_i^{\text{meas}})^2}{\sigma_{yi}^2}, \tag{4.12}$$

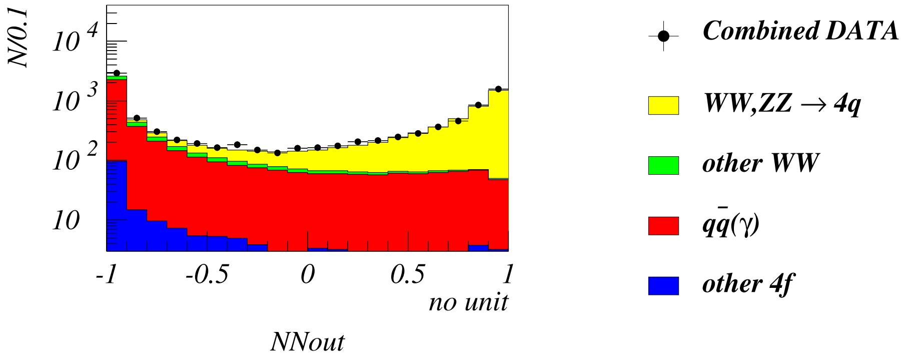

Figure 4.5: The neural network output variable for the fully-hadronic event selection. The light shaded histogram are the signal events, while the dark shaded histograms correspond to the background processes. It is clear that the $q\bar{q}$ background process is the most dominant.

where y_i^{fit} are the fitted jet energies and momenta and y_i^{meas} the measured ones. The estimated errors on the energies and momenta, σ_{yi}^2, are supplied by the user.

The constrained fit can be used to estimate the so-called effective centre-of-mass energy of an event, $\sqrt{s'}$ in the case of initial-state photon radiation. This measures the available centre-of-mass energy if one of the incoming beams radiated a photon, collinear with its flight direction. The number constraints is then reduced by one and the photon momentum is left free:

$$\sum_i^{n_{\mathrm{jets}}}(p_1, p_2, p_3, E) = (0, 0, p_z^\gamma, \sqrt{s} - |p_z^\gamma|), \tag{4.13}$$

where p_z^γ is the momentum of the radiated ISR photon, assuming it was emitted along the z direction. Although the experimental resolution on $\sqrt{s'}$ is not very good (a few GeV) it can be used to separate the $q\bar{q}(\gamma)$ background from the signal WW events. For a more detailed description of the constrained fit procedure in DELPHI we refer to [72].

4.4.2 Selection

The samples of fully-hadronic and semi-leptonic events required for the WW BEC analysis were selected using neural networks, developed in [73] and [74]

For the **fully-hadronic** event selection, a minimum multiplicity was required, a large effective centre-of-mass energy, $\sqrt{s'}$, large visible energy and a topology of four or more jets.

The final selection was performed using a neural network trained on thirteen event variables. A list of all the input variables and their distributions are given in App. B. Overall, a very good agreement between simulated and real data events was found for all the input distributions.

The neural network output variable for the fully-hadronic event selection is given in Fig. 4.5. The value of the output variable is close to -1 when an event is likely to be a background event and close to +1 when it is a signal event. It can be observed from the figure that the dominant background contribution comes from the $q\bar{q}(\gamma)$ events. All other backgrounds are negligible. The hadronically decaying ZZ events were taken as signal events in the fully-hadronic selection.

By requiring an neural network output bigger than a given value, a desired purity or efficiency can be reached [3].

The whole analysis is repeated for several cuts on the neural network output, selecting samples with an increasing purity, ranging from 83% to 97%. This will allow us to choose an optimal working point, as will be discussed later.

It was observed that the selection purity and efficiency depend little on the centre-of-mass energy, the average values are given in Tab. 4.2, together with the number of selected data events and the expected number of events calculated from Monte Carlo signal and background samples. The WPHACT [67] generator with the JETSET [47] hadronisation model was used for the simulation of all signal and four-fermion background events. The $q\bar{q}(\gamma)$ background was simulated using the KK2F [68] generator and also hadronized with JETSET.

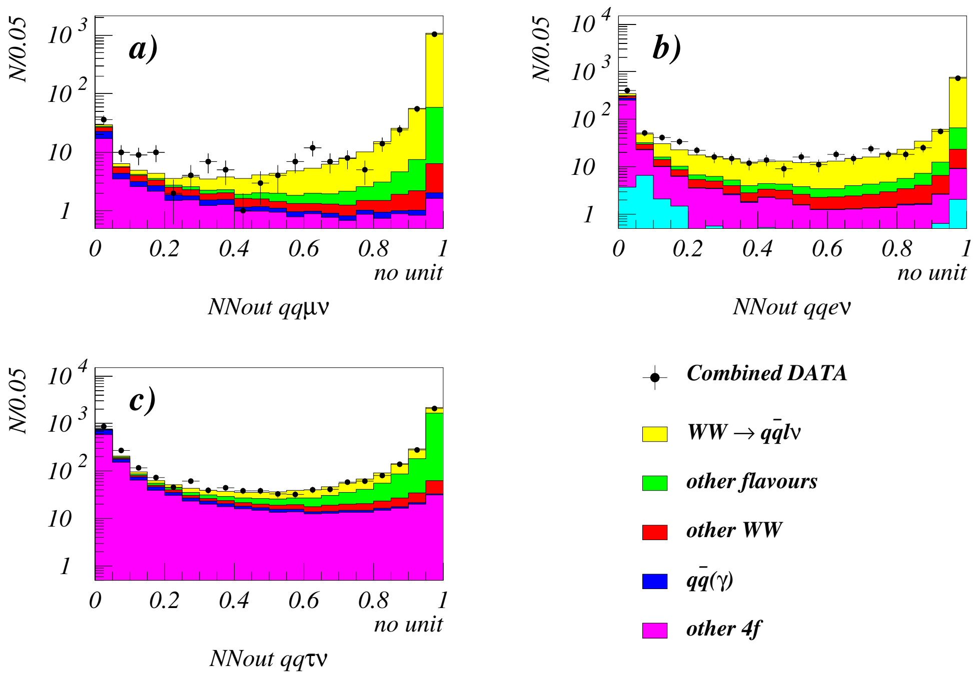

Figure 4.6: The neural network outputs for the three semi-leptonic event selections. The muon channel (a) and electron channel (b) have small background contaminations, due to the clear identification of the isolated lepton. (c) The taus are more difficult to identify, resulting in a higher background rate. All signal events are shown by the light shaded histograms, the background events correspond to the dark shaded histograms.

[3] The selection efficiency and purity are determined by means of Monte Carlo events. The efficiency is defined as the ratio of the total number of selected signal events and the total number of generated signal events, $\mathrm{eff} = N_{\mathrm{sel}}/N_{\mathrm{gen}}$. The purity is defined as the ratio of the total number of selected signal events and the sum of the total number of selected signal and background events, $\mathrm{pur} = N_{\mathrm{sig}}/N_{\mathrm{sig}} + N_{\mathrm{bg}}$.

The **semi-leptonic** events are selected by requiring two hadronic jets, a well isolated, identified muon or electron or a narrow jet with a low multiplicity (in case of hadronic tau decays) and missing momentum resulting from the neutrino. The missing momentum direction should point away from the beam pipe. Dedicated neural network trainings were used for all lepton flavours and are discussed in App. B. The final neural network outputs for all three lepton flavours are shown in Fig. 4.6. By cutting on a value of 0.4 for the electron and muon output and 0.9 for the tau output, an overall efficiency and purity of respectively 61% and 96% was reached, see Tab. 4.2. The semi-leptonic selection remains fixed for the rest of the analysis.

Selection	Fully-hadronic					Semi-leptonic
NN	NN > -0.3	NN > 0.0	NN > 0.3	NN > 0.6	NN > 0.9	NN > 0.4(e, μ) or 0.9(τ)
eff	0.84	0.80	0.73	0.63	0.33	0.61
pur	0.83	0.86	0.89	0.92	0.97	0.96
n_{obs}	4958	4516	3976	3252	1570	2567
n_{exp}	4922	4494	4002	3270	1593	2670

Table 4.2: The average purity and efficiency for both the fully-hadronic and semi-leptonic selection. The total number of selected data events and the number of expected events, calculated using signal and background Monte Carlo sets using the WPHACT and KK2F generators and hadronized with JETSET are also given.

4.4.3 Track selection

The analysis of two-particle inclusive densities requires a selection of tracks of good quality. In WW events, most of the charged particles are pions. Although no explicit pion identification is made, it is a good approximation to assume that all charged tracks in the event are pions.

The charged tracks used in the inter-W BEC analysis are required to fulfil the following criteria:

- information from the TPC was used to reconstruct the track;
- their momentum is bigger than 0.1 GeV/c;
- the relative error on the measured momentum, $\Delta p/p$ is smaller than unity;
- their impact parameter with respect to the nominal interaction point is less than 0.4 cm in the plane perpendicular to the beam and less than $1/\sin\theta$ cm along the beam;
- the particle is not associated with a reconstructed secondary vertex;
- the particle is not the tagged lepton or does not belong to the leptonic jet in the semi-leptonic selection.

The strict impact parameter cuts are stronger than the standard DELPHI track selection procedure. The cut is, however, justified since it reduces considerably the amount of tracks coming from secondary interactions with the detector material, as can be seen from Fig. 4.7. The total fraction of secondary tracks per event amounts to 5% after this stricter track selection, to be compared with more than 10% in the standard selection.

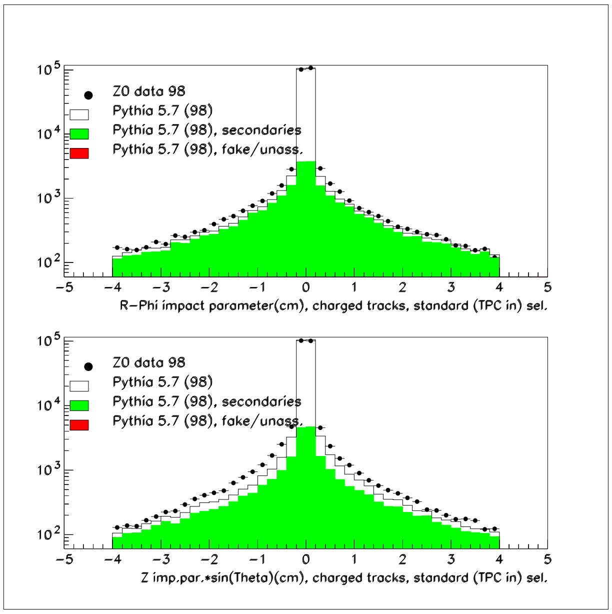

Figure 4.7: The impact parameters in the transverse and longitudinal plane w.r.t. the beam axis, showing the contribution of secondary tracks (filled histogram) to the total number of tracks (open histogram), compared with Z^0 data (solid dots). *S. Todorova, private communication.*

4.5 Measurement of inclusive two-particle densities

The selection criteria for fully-hadronic and semi-leptonic events, discussed previously, are necessary in order to reduce the contamination of background processes to a minimum. The semi-leptonic events, having a total background contamination of 4% are nearly free of background. The fully-hadronic events have a background contamination from $q\bar{q}(\gamma)$ processes, ranging from 17% to 3%, depending on the neural network output cut. The treatment of this background is explained in detail in the next section.

The construction of the "mixed" event sample is given special attention in Sect. 4.5.2. The mixing of semi-hadronic W events needs to be done with care, taking into account the geometrical differences in the detector acceptance and track resolutions. Furthermore, it will be shown that the inclusive two-particle density of fully hadronic events is strongly affected by the event selection procedure. It is therefore necessary that the "mixed" events are subjected to the same selection criteria.

Finally, the statistical properties of the two-particle densities are discussed in Sect. 4.5.2. It is shown that, due to correlations between different bins of the distributions, the statistical bin errors can be underestimated.

4.5.1 Background subtraction

Depending on the chosen value of the neural network output parameter, the fully hadronic W events can be contaminated by a considerable fraction of high energy $q\bar{q}(\gamma)$ events. Therefore, the density $\rho^{WW}(Q)$ is corrected for this background using the expression

$$\rho^{WW}(Q) = \frac{1}{N_{tot} - N_{q\bar{q}}} \left(\frac{dn_{tot}}{dQ} - \frac{dn_{q\bar{q}}}{dQ} \right), \tag{4.14}$$

where N_{tot} and $N_{q\bar{q}}$ are the total number of selected events and the number of selected background events, respectively, and n_{tot} and $n_{q\bar{q}}$ the respective number of particle pairs from these events.

The background is subtracted using simulated Monte Carlo events including Bose-Einstein correlations implemented with the LUBOEI BE_{32} algorithm. Due to the fact that the LUBOEI model is tuned using data at the Z^0 peak, we know that the model should describe the inclusive high energy Z^0 data fairly well. It is not known, however, whether it will describe the special subsample of events that are selected by the fully-hadronic WW selection. It would be impossible to select real WW-like $q\bar{q}(\gamma)$ events at high energies due to the high contamination by WW events itself. We therefore selected events at the Z^0 peak which exhibit a clear four-jet structure.

The top left plot of Fig. 4.8 shows a comparison of the two-particle density $\rho^{Z^0}(Q)$ taken from the inclusive Z^0 sample at $\sqrt{s} = 91.2$ GeV with the standard LUBOEI BE_{32} tuning, using an input correlation strength PARJ(92)=1.35. Since this parameter is tuned on inclusive Z^0 events, the description is very good. The following plots of Fig. 4.8 show how the agreement becomes worse when four-jet topologies are selected, using the LUCLUS algorithm, with an increasing jet resolution variable y_{34}. The input correlation strength is too high to describe the four-jet events. Therefore, an alternative background sample was used with a lower correlation strength of PARJ(92)=0.9. This gives a better description of the data having a clear four-jet topology, as can be seen from Fig. 4.8.

The background MC with the lower correlation strength of PARJ(92)=0.9 is used as standard for the background subtraction. A systematic uncertainty due to the uncertainty on that parameter is taken into account by performing the analysis subtracting two background samples corresponding to half of the data luminosity with respectively both tunings. The difference between results obtained by the standard and this alternative background subtraction are taken as systematic error.

4.5.2 W Mixing procedure

In this section it will be described how ρ^{WW}_{mix} is measured by means of mixing tacks from different events. The main features of a good "mixed" sample should be that it represents a real fully-hadronic sample in all respects, except for inter-W correlations.

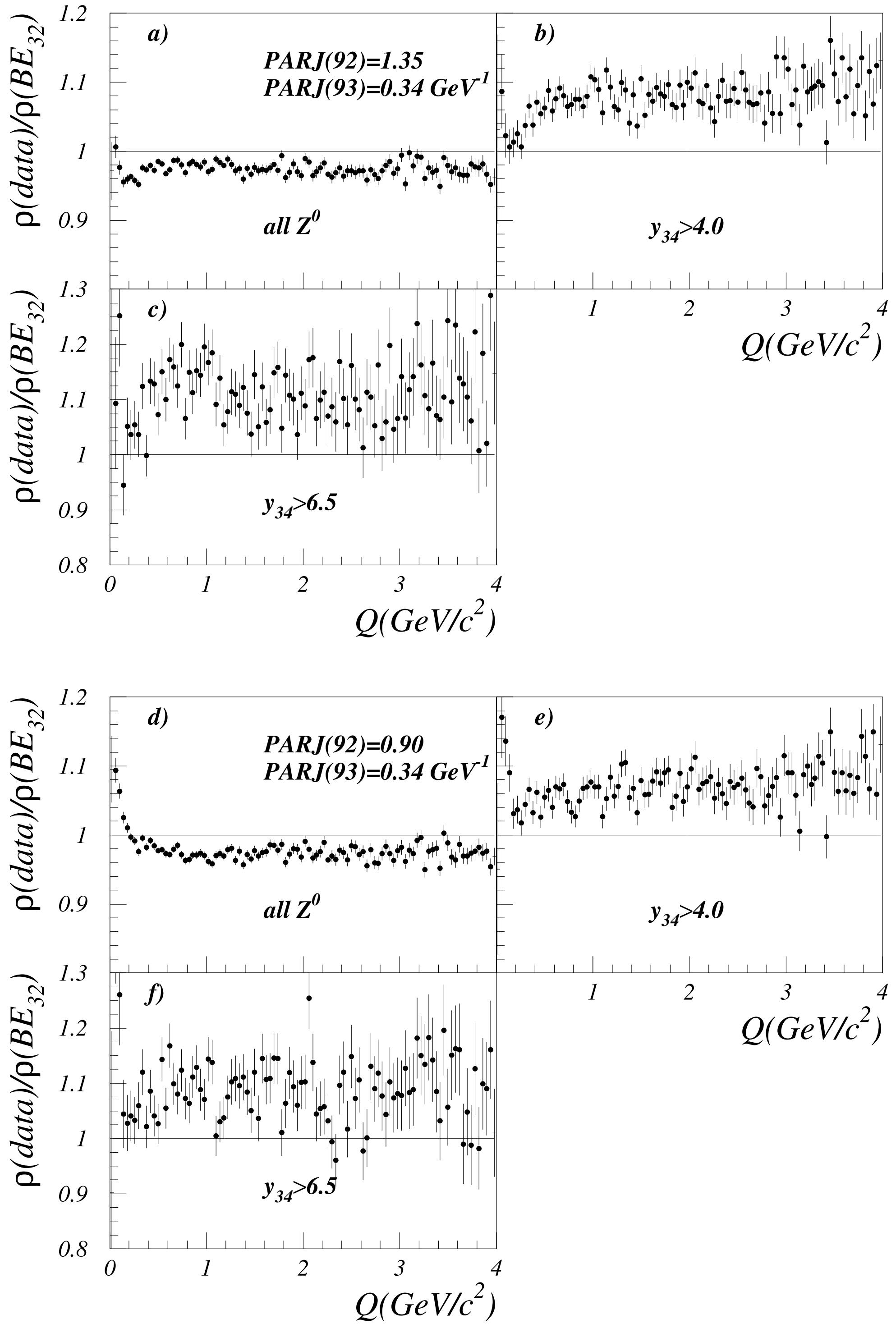

Figure 4.8: Top plots: The ratio of the two-particle densities of like-sign particle pairs for Z^0 events in data and in Monte Carlo events using the BE_{32} model with parameters PARJ(92)=1.35 and PARJ(93)=0.34, for the inclusive sample, a four-jet sample with $y_{34} > 4.$ and with $y_{43} > 6.5$. The three bottom plots show the same comparison but with a different BE_{32} input parameter PARJ(92)=0.9.

Technique

The mixed sample is constructed by taking a single hadronically decaying W and combine it with another one. These hadronic W's are taken from semi-leptonic WW decays, $q\bar{q}l\bar{\nu}_l$, of which the $l\bar{\nu}_l$ system is removed. In practice it means that the identified lepton, or leptonic jet is removed from these events, together with any possible remaining neutrals in a cone of $10°$ around it. The four-momentum of the hadronic W is obtained from a constrained fit, assuming total energy and momentum conservation of the event and where every W is given the nominal W mass of 80.35 GeV/c^2.

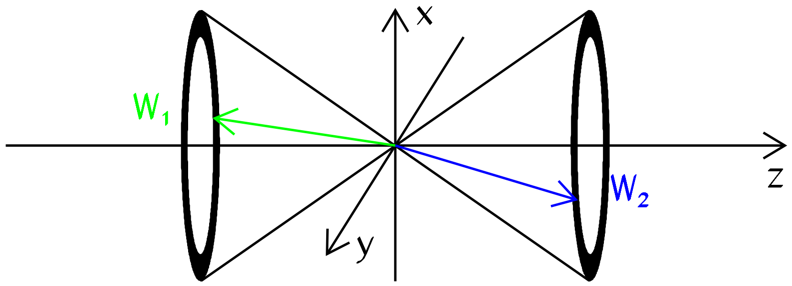

Figure 4.9: The surface on which different single W systems can be combined into a fully hadronic mixed event.

All particles from one W system are rotated in such a way that the directions of the momenta of the two W systems are opposite. In order to take into account the detector acceptance, two events are combined only if the W momenta are lying on a double cone of a diabolo shape with a full opening angle of $10°$. This is sketched in Fig. 4.9.

In order to make the combined event balanced in momentum, only rotations in azimuthal angle are performed in combination with an inversion of the z component of the momenta in cases where both W directions point in the same hemisphere. This reflects the azimuthal and left-right symmetry of the detector. The remaining imbalance in polar angle is not compensated for. Due to the presence of ISR photons, true fully hadronic WW events have an imbalance, resulting in a missing momentum spectrum that does not peak at zero. The ISR spectrum is simulated in the mixed events by smearing the W momenta obtained from the constrained fit. This smearing is performed by making a linear combination of the W momenta obtained from the 3C fit with the vector sum of all particles belonging to the W system:

$$\overrightarrow{p}_W = 0.4\overrightarrow{p}_{tracks} + 0.6\overrightarrow{p}_{3Cfit}. \tag{4.15}$$

An illustration of the effect of the smearing is shown in Fig. 4.10, where the missing momentum spectrum of fully-hadronic events is compared with mixed events. The improvement due to the smearing is clearly visible in the figure.

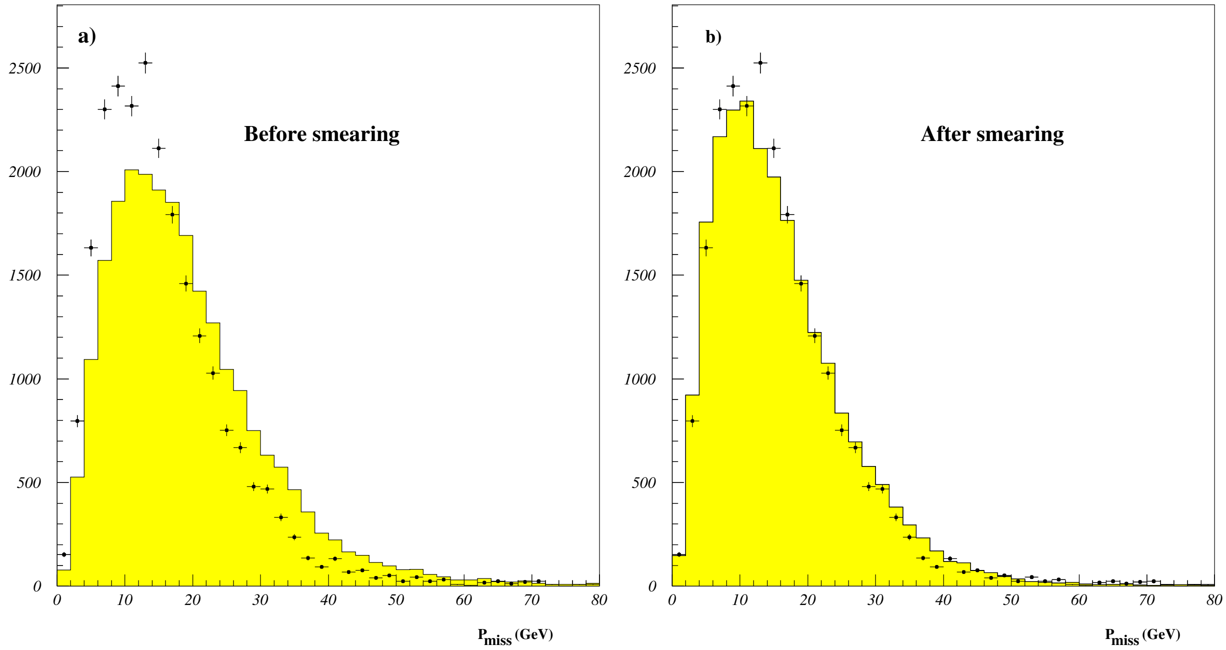

Figure 4.10: A comparison of the missing momentum spectrum, related to the ISR spectrum, and undetected particles, between fully-hadronic events (points) and mixed events (histogram), before (a) and after (b) smearing of the reconstructed W momenta.

Additional requirements

The mixing procedure results in a new sample of artificial events that have the same properties as fully hadronic WW events, except for inter-W correlations.

The DELPHI detector's two-track reconstruction efficiency drops drastically if the angle between two tracks becomes smaller than 2.5 degrees as can be seen from Fig. 4.11. Therefore, all track pairs having an opening angle less than 2.5 degrees are omitted in all the two-particle densities.

Due to the selection procedure, only a subsample of all true fully-hadronic WW events was selected. These are typically events with well separated jets, etc. It is clear that the two-particle densities are distorted by this selection. Figure 4.12 clearly illustrates this distortion. It shows the selection efficiency of the like-sign two-particle densities for WW events, obtained from a MC sample without BEC

$$\epsilon Q = \frac{\rho(2)_{\text{selected}}}{\rho(2)_{\text{all}}}, \tag{4.16}$$

where $\rho(2)_{\text{selected}}$ is the two-particle density of selected signal events and $\rho(2)_{\text{all}}$ two-particle density of all generated signal events. In the top plot of Fig. 4.12 (a) and (b) it is shown that the densities of pairs coming from the same W are hardly affected by the selection, while that of pairs coming from different W's (bottom Fig. 4.12) is clearly distorted. After applying the same event selections on the mixed events, this distortion is reproduced as can be seen from the bottom plot of Fig. 4.12.

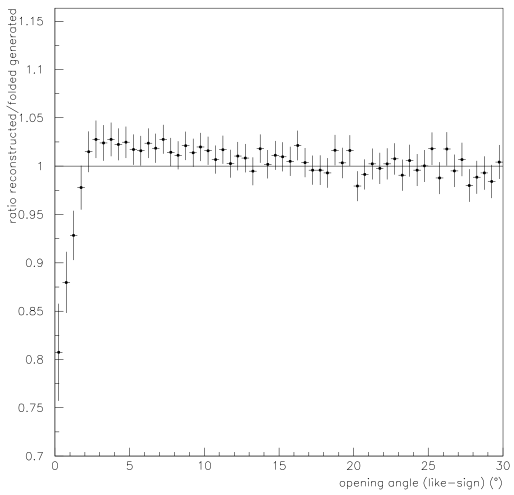

Figure 4.11: Reconstruction efficiency for like-sign pairs as a function of the opening angle α between the particles of the pair.

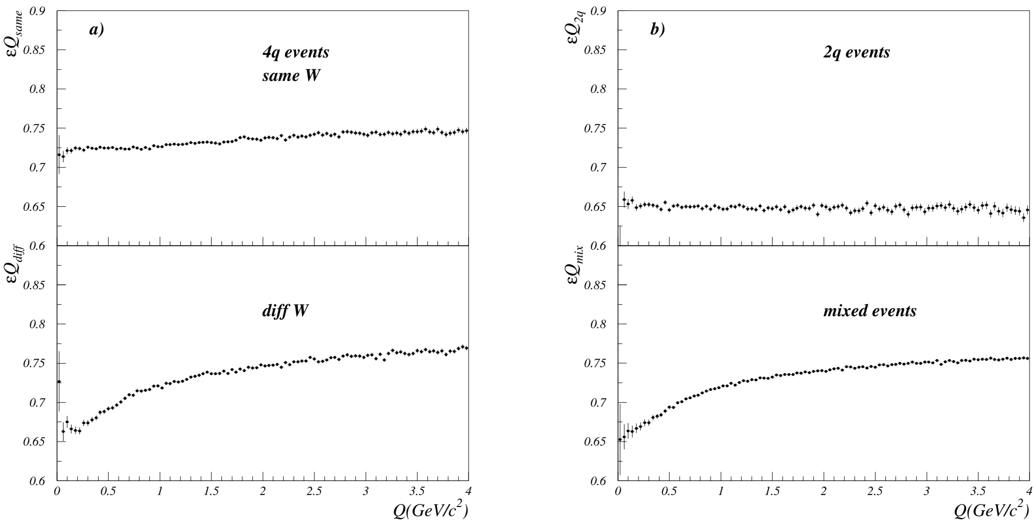

Figure 4.12: The influence of the event selection on like-sign pairs from the same and different W's a) in Monte Carlo generated fully-hadronic events. b) The same for pairs coming from semi-leptonic and from mixed events.

In Figs. C.1– C.5 a comparison is made between the combined data and the mixed events for all variables used as input for the fully hadronic neural network. To these variables, a set of seven other useful variables was added:

1. the number of charged particles in the event;

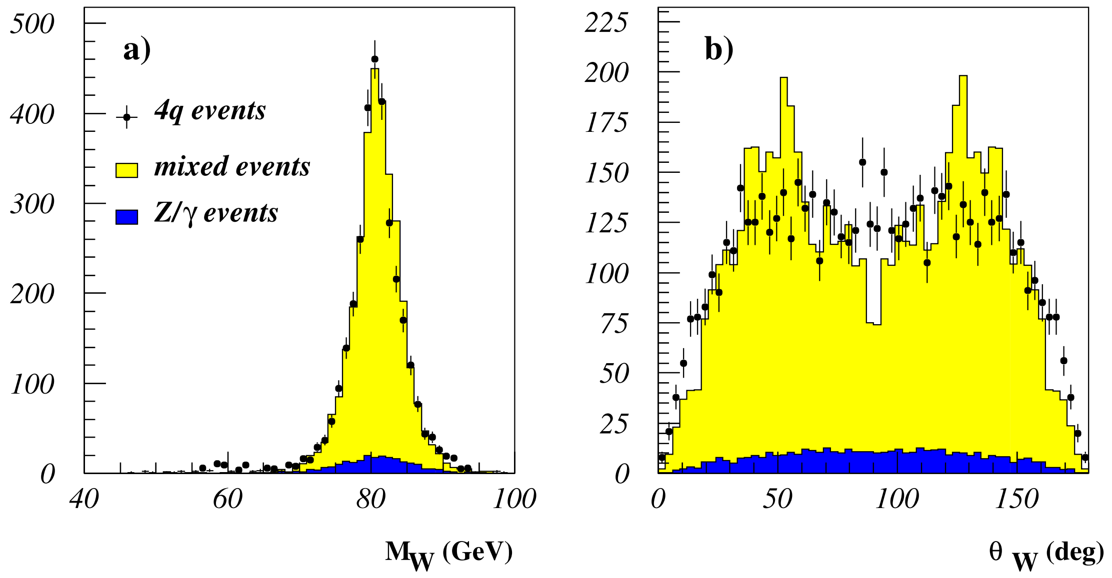

Figure 4.13: A comparison between real data mixed events (light shaded histogram) and fully-hadronic events (points) for a) the reconstructed W mass and b) the reconstructed polar angle of the W. The dark shaded histogram shows the contribution from the $q\bar{q}(\gamma)$ background.

2. the amount of missing momentum;
3. the $D_{4C} = \frac{E_{min}}{E_{max}} \frac{\theta_{min}}{E_{max}-E_{min}}$ variable;
4. the number of natural jets, clustered with LUCLUS, using a resolution variable $y_{ij} = 6.5$;
5. the neural net output variable;
6. the W mass after a 5C constrained fit;
7. the polar angle of the fitted W momenta.

The same comparison is made in Figs. C.6–C.10 for a MC sample at 189 GeV. In general a very good agreement is obtained in all these global event characteristics. An example is given in Fig. 4.13 where a good agreement between fully-hadronic data events and mixed events can be seen in the reconstructed W mass and a discrepancy due to a dip at 90° in the W polar angle distribution for mixed events. Since no rotations are made in polar angle in the mixing procedure, this is solely due to the semi-leptonic event selection cuts.

In addition to event shapes some relevant single particle spectra such as the momentum, transverse momentum and rapidity w.r.t. to the W momentum direction and the polar angle of all charged particles used to construct the two-particle densities are compared in Fig. 4.14. A similar comparison for Monte Carlo events can be found in Fig. C.12 of App. C. In all the distributions, very good agreement is found between mixed events and real fully-hadronic events.

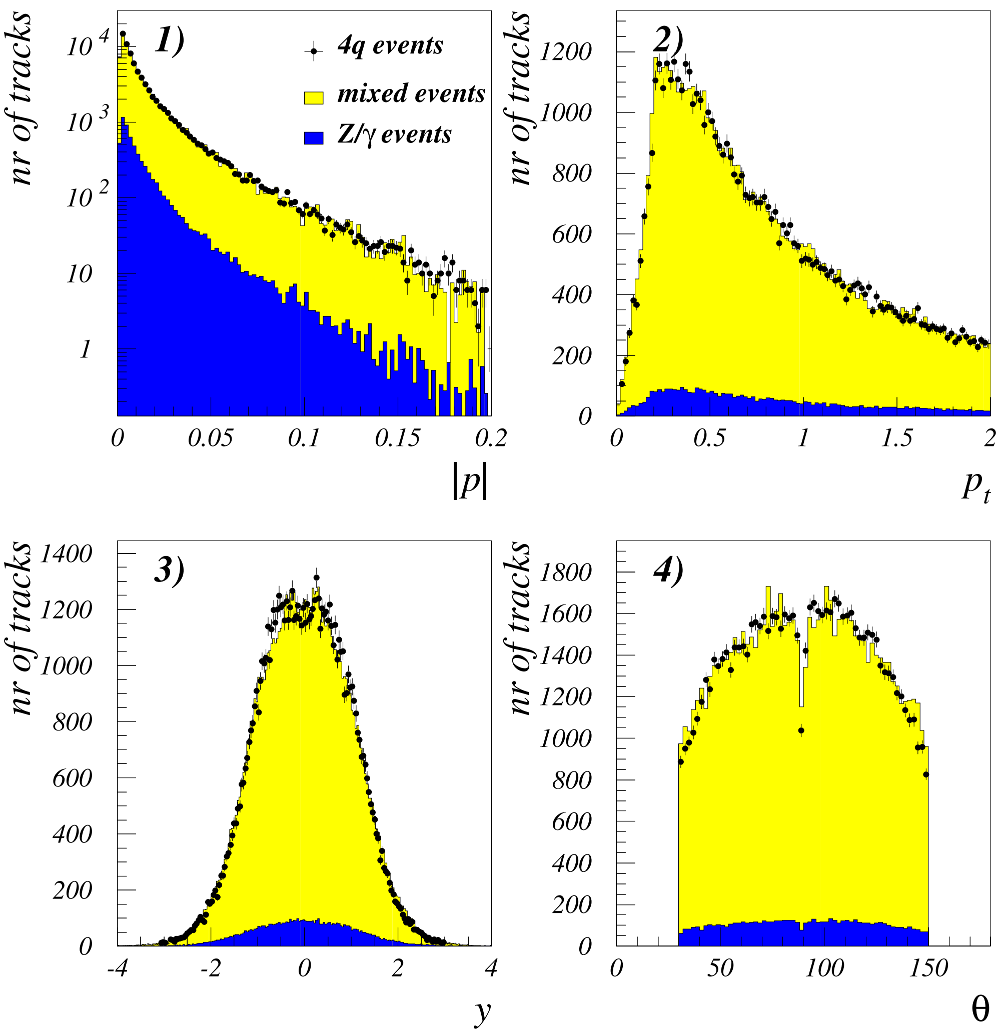

Figure 4.14: A comparison between real data mixed events (light shaded histogram) and fully-hadronic events (points) for (1) the momenta of all charged particles , (2) their transverse momentum w.r.t the W momentum, (3) the rapidity w.r.t. the W momentum and (4) the polar angle w.r.t. the z axis. The dark shaded histogram shows the contribution from the $q\bar{q}(\gamma)$ background.

Two particle densities and their statistical properties

An example of the two-particle Q distributions for the combined data set is shown in Fig. 4.15 for both like-sign particle pairs and unlike sign particle pairs. The two-particle densities for the fully-hadronic events, shown in the top of Fig. 4.15, is computed for all events which have a neural network output value bigger than 0.6. This corresponds to a purity of $\sim 92\%$ and a selection efficiency of $\sim 63\%$. The histograms show the contribution from $q\bar{q}(\gamma)$ background events as they are simulated with the BE$_{32}$ model with an input BE correlation strength of PARJ(92)=0.9.

In both the fully-hadronic and semi-leptonic samples, the number of unlike-sign pairs is higher than the number of like-sign pairs at Q values below 2 GeV/c^2. This is due to the large number of resonance decays with masses in this range. The area around $Q = 0.7$ GeV is dominated by $\pi^+\pi^-$ pairs coming from the ρ resonance which is abundantly present in hadronic decays of the W. Reflections of three-body decays are even present in the like-sign distributions. The two-particle densities of like-sign and unlike-sign pairs for the mixed events coincide, the reason for this being that all pairs in this distribution contain particles from different events.

None of the distributions in Fig. 4.15 are corrected for detector effects, it will be discussed later why these corrections are not necessary.

The statistical bin errors of the two-particle density distributions cannot be estimated using simple Poisson statistics. This can be understood as follows.

By taking combinations of n identically charged particles one obtains a total amount of $n(n-1)/2$ entries in the density distributions. Since a particle can contribute several entries in the same bin or in different bins, this introduces bin-to-bin correlations [75]. In addition, the value of n is fluctuating from event to event. In order to know the statistical bin error of the density distributions, several techniques can be applied. The simplest is a Monte Carlo re-sampling technique in which the analysis is repeated on N samples, containing a comparable amount of events as the data sample. This corresponds to a set of N repeated experiments. The spread on the number of bin entries for this set of N experiments gives an approximation for the true bin error.

A more rigorous method uses the covariance matrix of the distribution [76] defined as:

$$V_{j,k} = \frac{N_{ev}}{N_{ev}-1} \sum_{i=1}^{N_{ev}} (h_j^i - H_j/N_{ev})(h_k^i - H_k/N_{ev}), \tag{4.17}$$

where the h_j^i are the numbers of entries in bin j of event i and $H_j = \sum_i h_j^i$. The expression is nothing more than a long-hand notation of $\langle h_j h_k \rangle - \langle h_j \rangle \langle h_k \rangle$, where $\langle\ \rangle$ denotes the statistical average. Note that the diagonal elements of the covariance matrix are the variances of each bin: $V_{i,i} = \sigma_i^2$. If operations are done on several distributions, i.e. to construct variables $D(Q)$ and $\Delta\rho(Q)$, the covariance matrices of these quantities are computed using an analytical propagation according to classical statistical methods.
An example of the covariance matrices for the $\rho^{4q}(Q)$ and $\rho^{2q}(Q)$ distributions is given in Fig. 4.16.

The events in the density $\rho^{mix}(Q)$ are not statistically independent, in addition it will be correlated with $\rho^{2q}(Q)$. This problem is addressed by calculating the covariance ma-

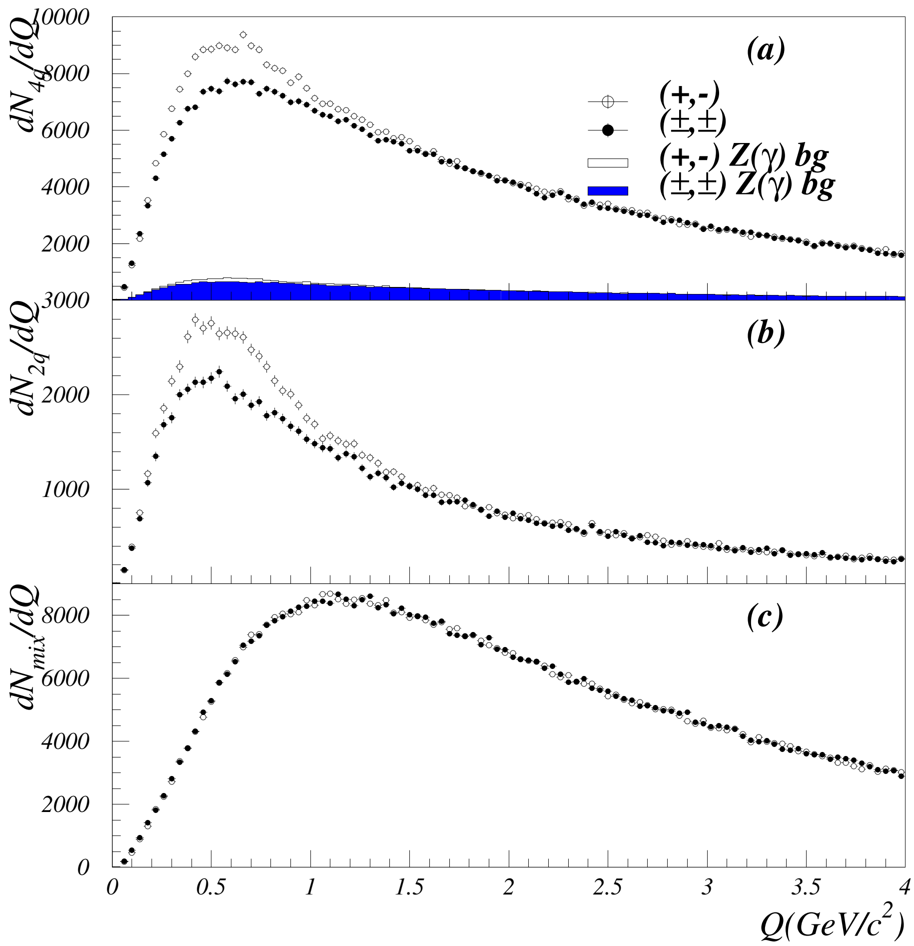

Figure 4.15: The two-particle distributions in the variable Q for like-sign and unlike-sign particle pairs. The contribution of the $q\bar{q}(\gamma)$ background to the fully hadronic WW decay channel is shown by the shaded histogram. Figure (a) shows the like-sign and unlike-sign densities for fully hadronic events, $N_{4q}\rho^{WW}(Q)$. Figure (b) shows the densities for semi-leptonic events, $N_{2q}\rho^{W}(Q)$, and Fig. (c) shows the densities for mixed events, $N_{\rm mix}\rho^{WW}_{\rm mix}(Q)$.

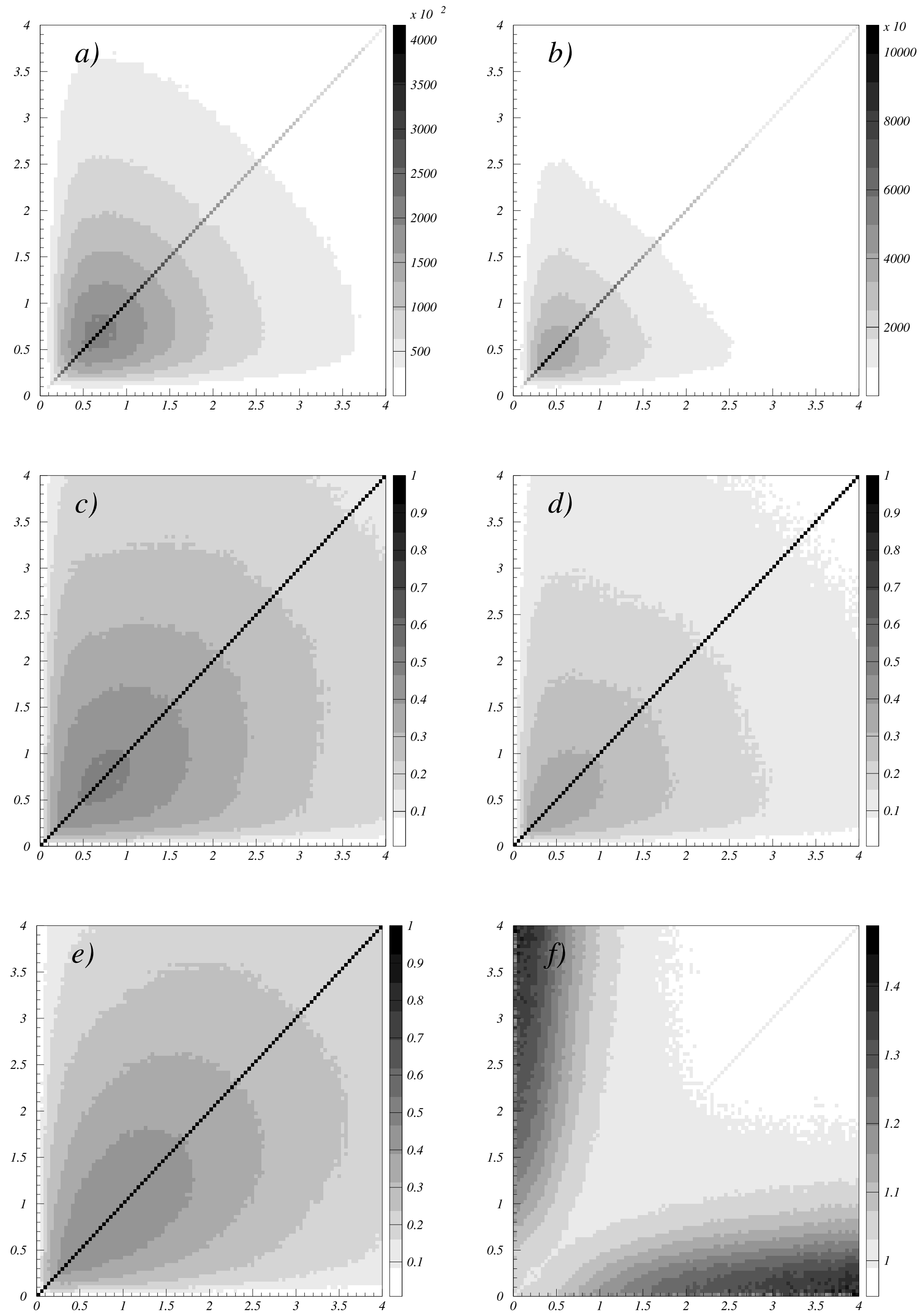

Figure 4.16: The covariance (a) and (b) and correlation matrices (c) and (d) for the $\rho^{4q}(Q)$ and $\rho^{2q}(Q)$ distributions are given respectively. The correlation matrix corresponding to the $2\rho^{2q}(Q) + \rho^{mix}(Q)$ distribution, (e), and the ratio between the correlation matrix of $2\rho^{2q}(Q) + \rho^{mix}(Q)$ and the correlation matrix of the independent sum of the 2 components (f) are also shown.

trix of the term $2\rho^{2q}(Q) + \rho^{mix}(Q)$ in one go. Let $H_j(2q) = \sum_{i=1}^{n_{2q}} 2h_j^i(2q)$, $H_j(mix) = \sum_{i=1}^{n_{mix}} h_j^i(mix)$ and $\mathcal{H}_j^i = \sum_{(i)} h_j^{(i)}(mix)$, where the last expression is the sum of the bin entries of all mixed events containing the same 2q event i. The covariance matrix then reads:

$$\begin{aligned} V_{jk}(2 \cdot 2q + mix) = \sum_{i=1}^{n_{2q}} & (H_j(2q)/n_{2q} - 2h_j^i(2q) + H_j(mix)n_{2q}(i)/n_{mix} - \mathcal{H}_j^i) \\ & \cdot (H_k(2q)/n_{2q} - 2h_k^i(2q) + H_k(mix)n_{2q}(i)/n_{mix} - \mathcal{H}_k^i), \end{aligned} \tag{4.18}$$

where $n_{2q}(i)$ represents the number of mixed events containing 2q event i.

As one can see, due to the presence of "interference" terms the covariance matrix $V_{jk}(2 \cdot 2q + mix)$ does not factorize:

$$V_{jk}(2 \cdot 2q + mix) \neq V_{jk}(2 \cdot 2q) + V_{jk}(mix). \tag{4.19}$$

An example of the correctly computed covariance matrix and the ratio of the correct covariance matrix with the one obtained assuming the 2 distributions to be independent is given in Fig. 4.16 e) and f).

4.6 The $\Delta\rho(\mathrm{Q})$ and $\mathrm{D}(\mathrm{Q})$ distribution

Using the normalised two-particle densities, $\rho^{WW}(Q)$, $\rho^{W}(Q)$ and $\rho^{WW}_{\mathrm{mix}}(Q)$ one can construct two variables which are sensitive to inter-W Bose-Einstein correlations. Their definition is, for reasons of clarity, once more repeated:

$$\Delta\rho(Q) = \rho^{WW}(Q) - 2\rho^{W}(Q) - 2\rho^{WW}_{mix}(Q), \tag{4.20}$$

$$D(Q) = \frac{\rho^{WW}(Q)}{2\rho^{W}(Q) + 2\rho^{WW}_{mix}(Q)}. \tag{4.21}$$

The measured $\Delta\rho(Q)$ distribution, using the complete dataset, together with the predictions from the BEins and BEfull model, are given in Fig. 4.17. The bin errors are taken as the square root of the diagonal elements of the covariance matrix of $\Delta\rho(Q)$.

From this figure, several observations can be made. Firstly, the BEfull model shows a deviation from zero, both in the like-sign and unlike-sign particle pairs.

An enhancement can be observed at Q values below 0.5 GeV/c^2, compensated by a dip in the Q range between 0.5 and 2.5 GeV/c^2. The reason for this dip is understandable for the following reasons. It is known that the total number of charged particles is not affected by any of the LUBOEI models. Therefore, the integral $\int_0^{Q_{\max}} \Delta\rho(Q)dQ$ should be exactly zero. As a consequence, any enhancement at low Q values must be compensated by a depletion at higher Q values. A second reason is that in real experimental situations it is practically impossible to obtain a sample of mixed events with exactly the same charge multiplicity as real fully-hadronic events. This is due to the nature of the selection procedure to obtain pure event samples. Any difference in charge multiplicity will therefore distort the structure of the $\Delta\rho(Q)$ distribution. In our case the mean charge multiplicity in the BEfull model is 0.8% higher in mixed events than in fully-hadronic events. Therefore, the total integral of the $\Delta\rho(Q)$ distribution will be negative.

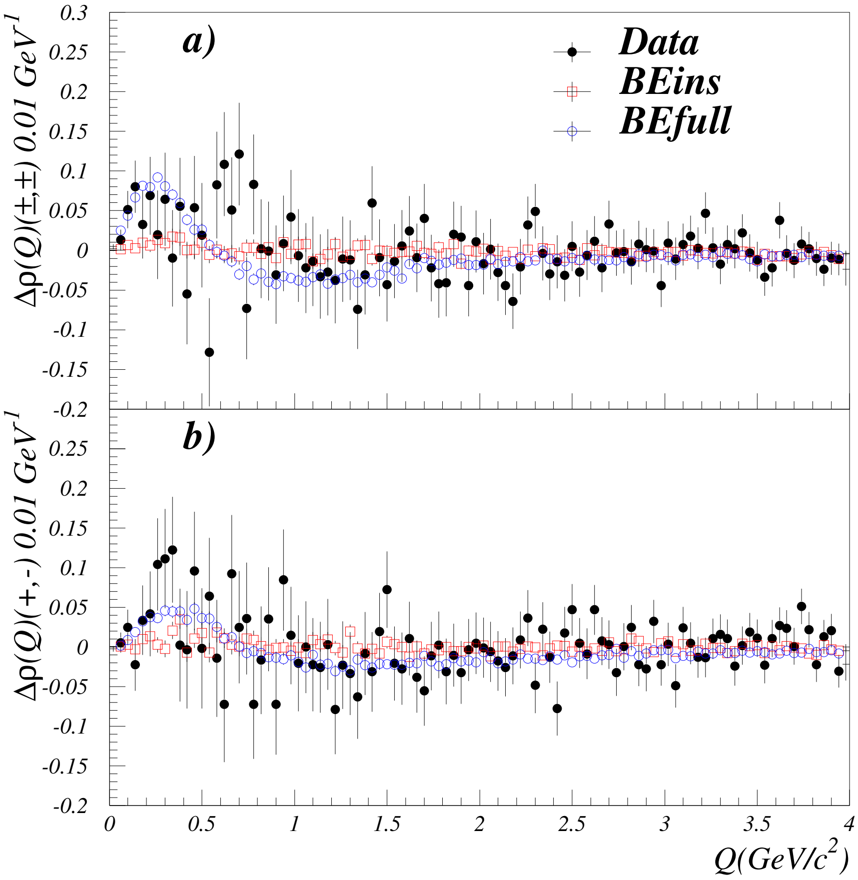

Figure 4.17: The $\Delta\rho(Q)$ distribution for like-sign particle pairs a). The MC predictions for the BEins and BEfull model are superimposed. In b) the same is shown for unlike-sign particle pairs.

In the BEins model this difference is only 0.4% and its $\Delta\rho(Q)$ distribution is more compatible with a constant zero. Furthermore, no enhancement at small Q values is observed in this model.

The data exhibit an excess similar to the BEfull scenario, both for like-sign and unlike-sign pairs, although at even smaller Q values than the model.

The measured $D(Q)$ distribution is shown in Fig. 4.18, together with the BEins and BEfull Monte Carlo predictions. All bin errors are extracted from the covariance matrix of $D(Q)$. A clear enhancement at low values of Q can be observed in Fig. 4.18 for the like-sign

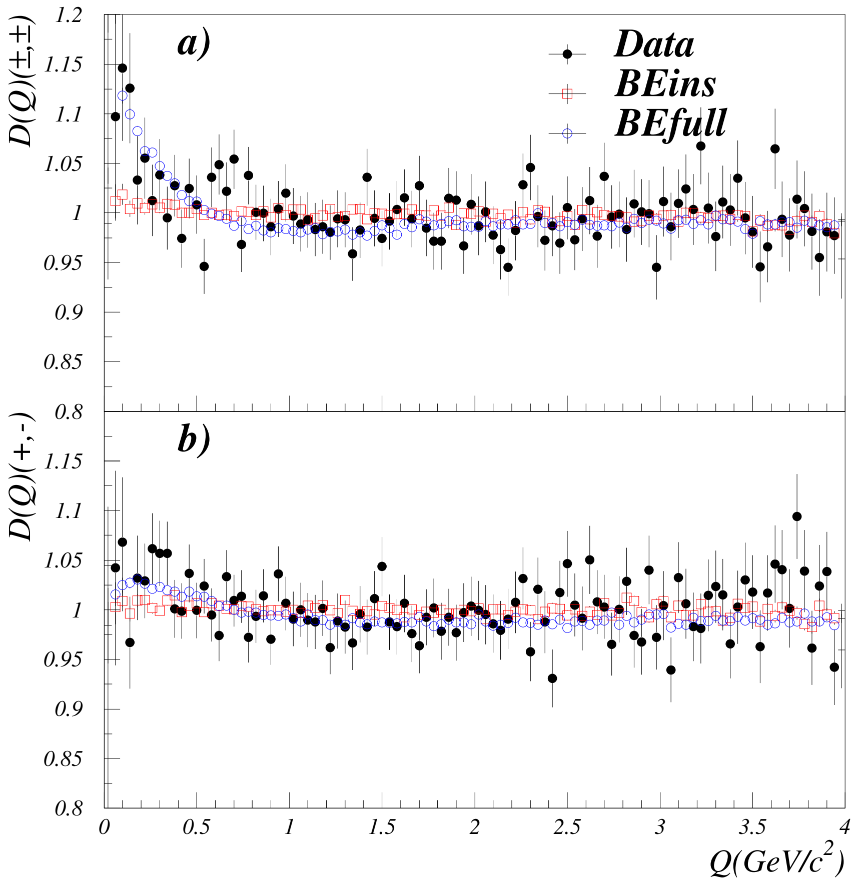

Figure 4.18: The $D(Q)$ distribution for like-sign particle pairs a). The solid dots represent the combined dataset. In addition, the predictions from a WPHACT Monte Carlo simulation of the BEins model (open squares) and the BEfull model (open dots) is shown. In b) the same distributions are shown for unlike-sign particle pairs.

pairs of the BEfull model. A smaller enhancement can, again, be observed in the unlike-sign pairs as well. In both cases, a dip can be observed on the Q region between 0.5 and 2.5

GeV/c^2, for the same reasons as mentioned in the discussion of the $\Delta\rho(Q)$ distribution.

In both the like-sign and unlike-sign distributions, the BEins model shows a flat distribution, compatible with one. The combined data lie in between the two models, showing again an excess situated in a very small Q region, below 0.3 GeV/c^2, both for like-sign pairs and unlike-sign pairs.

4.6.1 Quantifying the result

From the discussion of the properties of the $\Delta\rho(Q)$ and $D(Q)$ distributions we concluded that small enhancements at low Q values are present in the data, both for like-sign pairs and unlike-sign pairs. To quantify the presence or absence of inter-W Bose-Einstein correlations two methods are used. They consist in either integrating the $\Delta\rho(Q)$ distribution or fitting the $D(Q)$ distribution with a functional form.

In [77], a large emphasis is given to the method consisting of integration the $\Delta\rho(Q)$ distribution. One can argue [78] that $\Delta\rho(Q)$ is a more fundamental physical quantity, while $D(Q)$ is often misinterpreted as being a genuine correlation function. Although we agree with the latter statement, it will be demonstrated that, from an experimental point of view, the $\Delta\rho(Q)$ distribution is not the most suitable to extract a quantitative result. In what follows, some arguments against the use of this method are given:

- It is clear that in the $\Delta\rho(Q)$ distribution, experimental biases are easily identified. In particular, any differences in the charge multiplicity distribution between fully-hadronic events and mixed events, will result in a deviation from zero of the total integral of $\Delta\rho(Q)$. There is however no rigorous way to take this bias into account.

- The statistical error on $\int_0^{Q_{\max}} \Delta\rho(Q)dQ$ depends on the value of $Q_{\max}$. The sensitivity of the measurement will therefore decrease drastically with increasing integration range. This is demonstrated in Fig. 4.19, where the cumulative distribution, $\int_0^{Q} \Delta\rho(Q)dQ$ is given for like-sign and unlike-sign particle pairs for data and model predictions. The bands correspond to one standard deviation errors on the measured values.

- Although it is often assumed that integrating $\Delta\rho(Q)$, does not assume any model or functional form, its integration domain is based on predictions by the BEfull model. In [77], the value of $Q_{\max}$ coincides with the Q value at which the $\Delta\rho(Q)$ distribution becomes statistically compatible with zero.

Our approach focusses on a fit of the $D(Q)$ distribution, with the following expression:

$$f(Q) = N(1 + \Lambda e^{-RQ})(1 + \delta Q), \tag{4.22}$$

where the value of Λ quantifies the excess due to the presence of inter-W BEC.

A fit of the $D(Q)$ distribution has, indeed, the disadvantage that a functional form has to be assumed. When this functional form is used to quantify the excess at low Q values without attributing a physical meaning to its shape, we see no problem in the use of it. In addition, any normalisation biases due to multiplicity differences can be "absorbed" in the

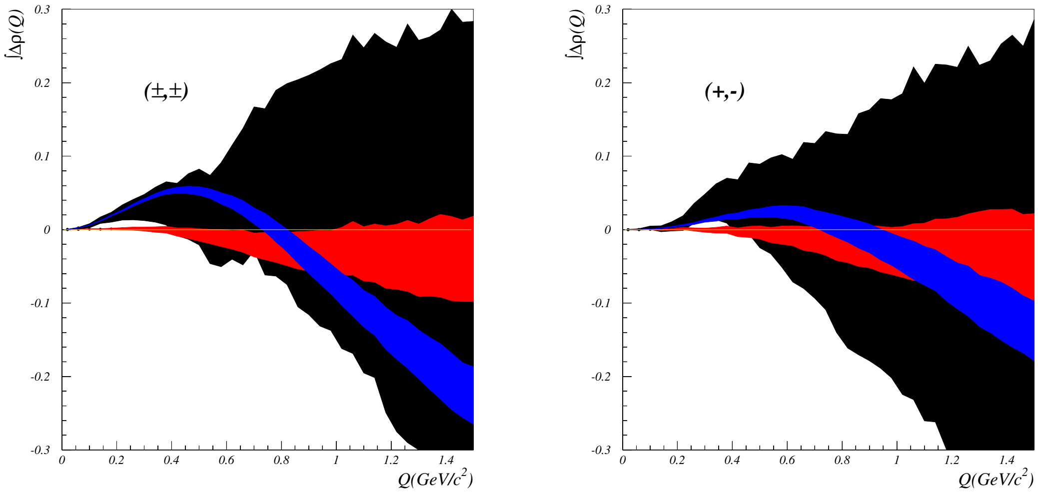

Figure 4.19: The cumulative distributions of $\Delta\rho(Q)$ for like-sign (left) and unlike-sign (right) particle pairs. The 1 σ bands are given for data (black band) and both the BEins (light shaded) and BEfull model (dark shaded).

parameters N and δ. Moreover, an integral of the $\Delta\rho(Q)$ distribution up to a value of $Q_{\max}$, corresponds to a fit of $D(Q)$ with the step function

$$f(Q) = \begin{cases} I & \text{if } Q \leq Q_{\max}, \\ 0 & \text{if } Q > Q_{\max}, \end{cases} \tag{4.23}$$

where I corresponds to the integral $\int_0^{Q_{\max}} \Delta\rho(Q)dQ$.

In what follows, we therefore focus on the fit of $D(Q)$, where however, unexpected statistical problems occur. These are discussed at length in the following section.

4.6.2 Fitting D(Q)

In order to fit the distribution $D(Q)$ with Eq. 4.22 a χ^2 method was chosen. All fits are taken in the range of Q between 0 and 4 GeV/c^2. The reason for fitting such a long Q range is that it gives a better handle on the normalization parameter N and slope δ. When fitting correlated bins, the χ^2 function to be minimized has the following form:

$$\chi^2(N, \delta, \Lambda, R) = (f(Q) - D(Q))^T V^{-1}(f(Q) - D(Q)), \tag{4.24}$$

where $(f(Q) - D(Q))$ is the difference of the fit function and $D(Q)$, and V^{-1} the inverse of the covariance matrix of $D(Q)$. This method has, however, its limitations and possible dangers. A χ^2 fit takes into account correlations between bins, but only up to second order. Furthermore it assumes that all bin errors have gaussian distributions. In the case of $D(Q)$, which is a ratio of two-particle densities, this method tends to bias the fitted parameters,

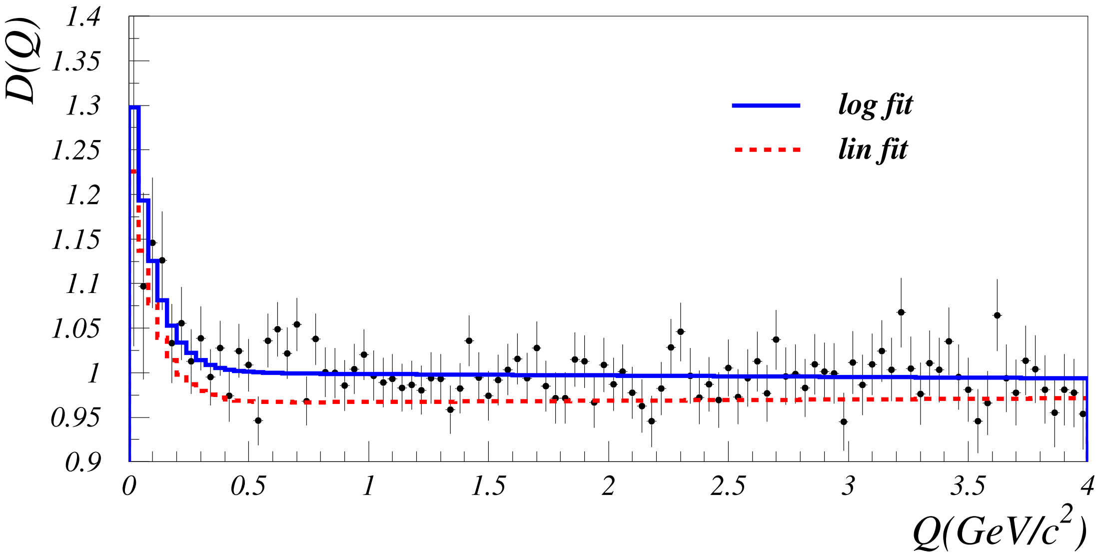

Figure 4.20: The fit results for the D(Q) distribution of the combined data set using either the linear fit approach or the logarithmic approach.

especially the normalization parameter N. The origin of this bias is due to the data points being strongly correlated with their errors. The fact that the data points are also mutually strongly correlated even enhances this effect. A simple gedanken experiment to illustrate the problem is given in App. A. It is clear that if a low bin value of $D(Q)$ has a much smaller statistical error than a high bin value, the total fit will be biased towards a result with a too low value of N.

As shown here, the easiest solution is to remove the correlations between data points and their errors, at least to first order. This can be achieved by fitting the natural logarithm of $D(Q)$ where the covariance between the bins is given by:

$$C_{ij} = \frac{C_{ij}^{DQ}}{D(Q)_i D(Q)_j}, \tag{4.25}$$

where C^{DQ} is the original covariance matrix of $D(Q)$ and $D(Q)_i$ the value of bin i of $D(Q)$.

An example of a fit to the combined data set using a normal fit together with a logarithmic fit, removing the bias is shown in Fig. 4.20. It can be seen on this figure that the logarithmic fit, indicated by the solid line is not lying systematically below all the data points, as is the case for the dashed line, corresponding to a linear fit. In the following, all fits will be performed using the logarithm-method.

In order to check the consistency of the method, 125 Monte Carlo samples of the same size as the data were generated. From these samples, the "pulls" on all parameters, defined as the difference between the mean value and the values from the independent samples, divided by their respective statistical error, were computed. The results are shown in Fig. 4.21. The widths of the pull distributions indicate that the statistical error on all parameters is correct up to 2%.

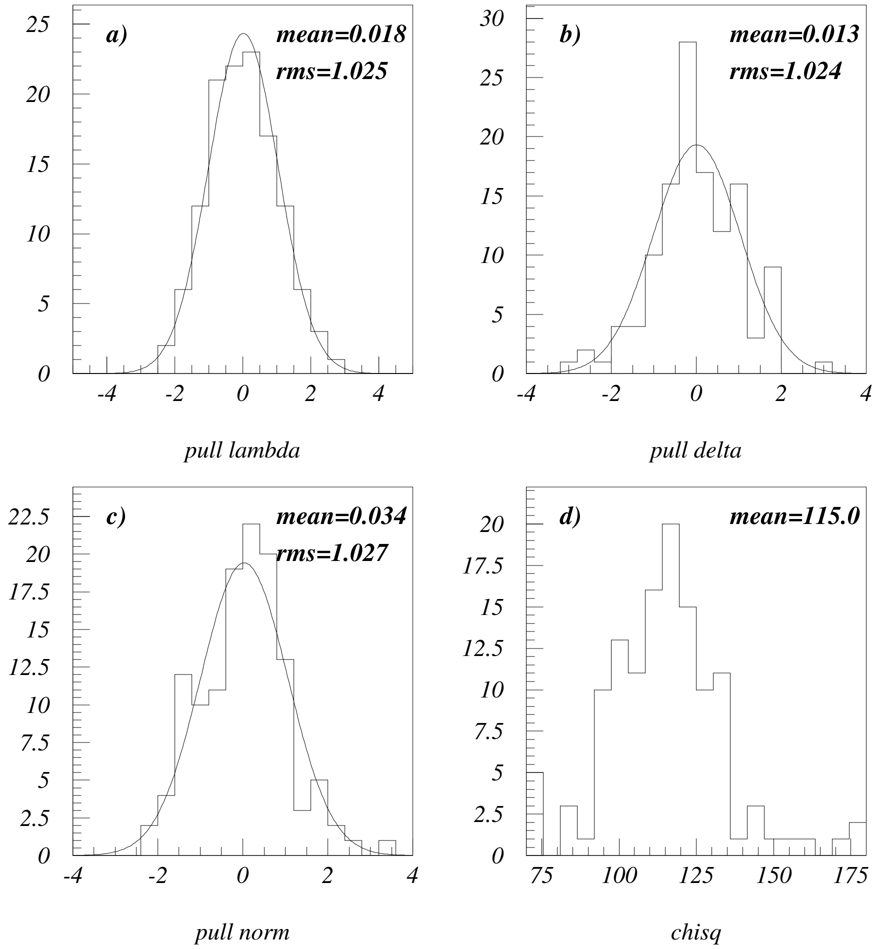

Figure 4.21: The "pull" distributions for the fitted parameters using 125 samples obtained from the BEins model. In addition the, χ^2 distribution of the fits is shown. All pulls were fitted with a Gaussian, giving the same width as the RMS computed from the distribution itself.

NN cut/parameter	Λ	$R(fm)$	δ	N	χ^2 (97 NDF)
-0.3 $(P = 83\%)$	0.264±0.008	0.90±0.03	0.0011±0.0007	0.975±0.002	201.6
0.0 $(P = 86\%)$	0.260±0.008	0.90±0.03	0.0016±0.0007	0.978±0.002	199.9
0.3 $(P = 89\%)$	0.253±0.008	0.88±0.03	0.0022±0.0007	0.980±0.003	199.9
0.6 $(P = 92\%)$	0.239±0.008	0.84±0.03	0.0034±0.0007	0.978±0.003	190.9
0.9 $(P = 97\%)$	0.193±0.008	0.67±0.03	0.0087±0.0010	0.957±0.003	162.5

Table 4.3: Results of the fit of $D(Q)$ with Eq. 4.22 for the BEfull MC sample, for different values of the cut on the neural net output parameter (with corresponding purity, P) in the fully-hadronic WW selection.

4.7 Results

In order to quantify the excess at low Q values in the data, a fit is performed using Eq. 4.22 where the parameter R is fixed to the value obtained from a fit to the BEfull sample. The results of the fits to the like-sign $D(Q)$ distribution for like-sign pairs and for various neural network outputs of the fully-hadronic sample is given in Tab. 4.3. From these results it can be concluded that the values of Λ slightly decrease with increasing purity. This is understandable since, a stricter selection will result in an event sample having well separated jets, hereby reducing the fraction of pairs with a small Q value, coming from different W's. The radius parameter, R, decreases as well with increasing neural network cut, mainly due to the strong correlation with Λ (69%).

The reason why the radius parameter is kept fixed is the strong correlation with the Λ parameter itself. Moreover, fits performed on the BEins model which result in nearly flat distributions, become unreliable if R is left free. In what follows, it will be discussed how the optimal working point, in terms of the purity of the fully hadronic sample is chosen.

After the determination of the optimal working point, the sensitivity of the analysis will be further increased by increasing the purity of pairs originating from different W's.

Finally, a discussion of the systematic uncertainties of the analysis with increased purity will be given, together with a discussion of the results.

4.7.1 Optimisation of the analysis

It was already discussed previously in sections 4.5.1 and 4.5.2 that a selection procedure is necessary to separate the fully-hadronic events from $q\bar{q}(\gamma)$ background. For this purpose a cut on the neural network output is made. The event purity, corresponding to each cut is given in the first column of Tab. 4.3. This background is known to have Bose-Einstein correlations between all identical bosons in the event. The strength of the correlations in this background sample is not known. They are modeled using the BE$_{32}$ model with an input correlation strength of PARJ(92)=0.9. We will refer to this background sample as "Bg1" for further discussion. An alternative background sample, referred to as "Bg2", consists of an equal mixture of Monte Carlo events having a correlation strength of PARJ(92)=0.9 and a strenght PARJ(92)=1.35.

A systematic uncertainty due to the lack of knowledge of the correlations in the background is, consequently, assigned to our measurement of Λ. It is equal to the absolute difference in the Λ values, measured from data, when either Bg1 or Bg2 is subtracted.

It is clear that this uncertainty decreases with increasing purity of the fully-hadronic selection, but at the expense of decreasing statistical precision on the measured Λ value.

Secondly, the selection procedure can introduce a bias in the measurement of Λ. This bias is extracted from a fit to the BEins Monte Carlo model. The measured value of Λ for this sample, being zero for a perfect analysis, is taken as a second systematic uncertainty on our measurement.

It is assumed that only these two systematic uncertainties depend on the choice of neural network cut. The neural network cut, which yields the smallest total uncertainty on Λ, is taken as the working point for the rest of the analysis.

The fits to the data samples for various neural network cuts are summarised in Tab. 4.4. The corresponding errors on the parameters are statistical only. The statistical error on Λ varies little with increasing neural network cut and so does its value.

NN cut/parameter	Λ	R	δ	N	χ^2 (97 NDF)
-0.3	0.136±0.053	0.90	0.0061±0.0061	0.956±0.024	101.0
0.0	0.141±0.053	0.90	0.0064±0.0062	0.962±0.024	102.9
0.3	0.152±0.053	0.88	0.0058±0.0063	0.969±0.024	98.4
0.6	0.135±0.053	0.84	0.0035±0.0064	0.983±0.025	93.4
0.9	0.138±0.056	0.67	0.0048±0.0080	0.983±0.029	102.9

Table 4.4: Results of the fit of $D(Q)$ with Eq. 4.22 for the total data sample, for different values of the cut on the neural net output parameter in the fully-hadronic selection. The R parameter is fixed to the values obtained from a fit to the corresponding BEfull Monte Carlo sample.

The total error on the measured Λ values for each neural network cut are summarised in Tab. 4.5. It can be seen in this table that the systematic uncertainty due to the background subtraction indeed decreases with increasing neural network cut. All other contributions vary little with increasing neural network cut, except for the extreme cut at $NN > 0.9$. The smallest total error is obtained for a cut at $NN > 0.6$, with a corresponding event purity of 92%. The analysis is, therefore, fixed at this neural network value.

4.7.2 Sensitivity

It should be realised that the number of pion pairs originating from different W's is a relatively small fraction of all pairs. This can be seen in Fig. 4.22, where the fraction of pairs from different W's, often denoted as $F(Q)$, is shown. It drops to around 20% at very low Q values. It is, therefore, important to try to increase this fraction, especially in the low Q region.

Besides Q itself, two more variables are found to be sensitive to whether a pair of tracks is coming from different W's or from the same W. These variables are the Lorentz γ factor

NN cut/error	$\sigma_{\text{stat}}(\Lambda)$	σ_{sel}	σ_{bg}	σ_{tot}
-0.3	0.053	0.012	0.031	0.062
0.0	0.053	0.012	0.024	0.059
0.3	0.053	0.014	0.018	0.058
0.6	0.053	0.012	0.011	0.055
0.9	0.056	0.023	0.002	0.060

Table 4.5: Summary of the main contributions to the total error on Λ for all neural network cuts. From left to right are given: the statistical uncertainty (σ_{stat}), the systematic uncertainty due to the event selection (σ_{sel}), the systematic uncertainty due to the background subtraction (σ_{bg}) and the total error (σ_{tot}). The sample corresponding to a neural network output cut of 0.6 has the smallest total error and is chosen as working point for further analysis.

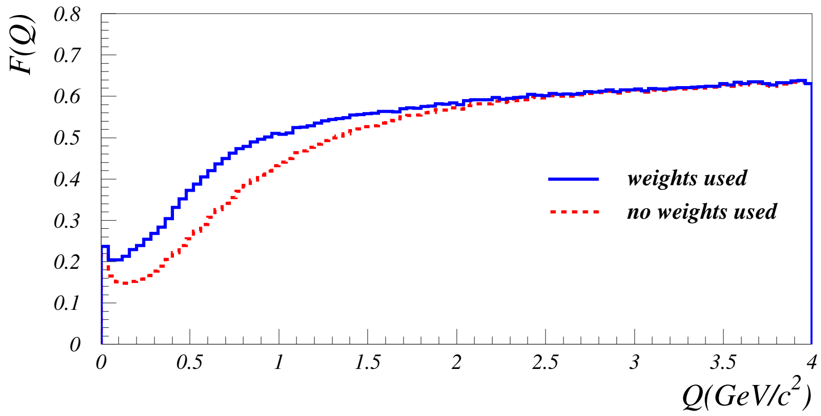

Figure 4.22: The fraction of pairs coming from different W's, $F(Q)$, obtained for a BEins MC sample without pair weights (dashed line) and using pair weights (full line).

of the pair, assuming the pair to be massless:

$$\gamma = \frac{|\overrightarrow{p_1}| + |\overrightarrow{p_2}|}{\sqrt{(|\overrightarrow{p_1}| + |\overrightarrow{p_2}|)^2 - |\overrightarrow{p_1} + \overrightarrow{p_2}|^2}}, \tag{4.26}$$

and the opening angle θ^*, being the angle between one of the two particles in the rest frame of the system and the system's flight direction in the lab frame, where

$$\cos\theta^* = \frac{||\overrightarrow{p_1}| - |\overrightarrow{p_2}||}{|\overrightarrow{p_1} + \overrightarrow{p_2}|}, \tag{4.27}$$

with $\overrightarrow{p_1}$ and $\overrightarrow{p_2}$ the three-momenta of the two particles. These two variables are plotted versus Q for pairs coming from the same and from different W's in Fig. 4.23. The pair fractions are parametrized in this three-dimensional space.

For each individual pair, the "purity" $p(Q, \gamma, \cos\theta^*)$ can be computed and parametrized. As such, each individual pair of tracks can be estimated to have a purity $p(Q, \gamma, \theta^*)$. The sensitivity to Λ will be proportional to this purity. However, the statistical error also depends significantly on whether a pair is coming from the same W event or from two mixed events.

The contribution to the total variance of D(Q) for pairs coming from the same W (taken from the semi-leptonic events) is estimated to be 97.7%, while mixed pairs gave only a variance of 38.6%. The total amount of information coming from a given pair is then proportional to $p/(0.386p + 0.977(1-p))$. When all particle pairs are weighted with their information content, one obtains the full curve for $F(Q)$ in Fig. 4.22. The gain in sensitivity can be estimated fitting the BEfull sample for an unweighted analysis and a weighted analysis. The results are summarized in Tab. 4.6. From this table we can conclude the following. The analysis using pair weights gives, as expected, an increase in sensitivity of 14%, as can be observed from the fits to the BEfull sample. In addition to the BEins model, models without any BEC were also analysed. Studies were made using the JETSET, ARIADNE and HERWIG hadronisation models without BEC. Their fitted Λ values do not change drastically when applying event weights. These models are also used in combination with several implementations of colour reconnection, which will be discussed in more detail in Sect. 4.8.

The results of the real data are given as well. Two background samples have been subtracted from the data, the standard sample, Bg1 and the alternative sample, Bg2. The absolute change in the measured Λ due to the use of an alternative background sample is similar in both the unweighted analysis and the analysis using weights.

The increase in sensitivity and the stability of the results for models without inter-W BEC favours, consequently, the use of the pair-weight analysis. A summary of the measured Λ values obtained from the data at several energy points and the final combined result is given in Tab. 4.8 for like-sign and unlike-sign particle pairs. The data collected at 192 and 196 GeV and at 200 and 202 GeV are combined in order to get a statistical precision similar to the other energy points. The statistical correlation between the measured Λ value in like-sign pairs and unlike-sign pairs was estimated to be 60%.

Figure 4.24 shows the $D(Q)$ distribution for the combined data sample, using the pair-weight analysis. The shaded band indicates the fit to the data points with Eq. 4.22, fixing R to 0.994 fm. The width of the band indicates the statistical uncertainty on all fit parameters, taking into account their mutual correlations. The correlations between all free fit parameters are given in Tab. 4.7. The full lines indicate the fits to the BEins and BEfull models.

The data were also fitted with Eq. 4.22, leaving the R parameter free. The results of this fit are summarised in Tab. 4.9. It is clear that introducing a free parameter increases the statistical uncertainty of the measured Λ. However, it is interesting to observe that the R parameter, measured from the data is higher than the R parameter, measured from the BEfull model. Unfortunately, the statistical precision on the measured R value is rather low. It is also clear that the measured R parameter is smaller for unlike-sign pairs than like-sign pairs, both in real data and in the BEfull model. A two-dimensional contour plot, giving the one, two and three σ contours of the measured Λ and R parameter for the combined data is given in Fig. 4.25. The result for the BEfull model is also shown.

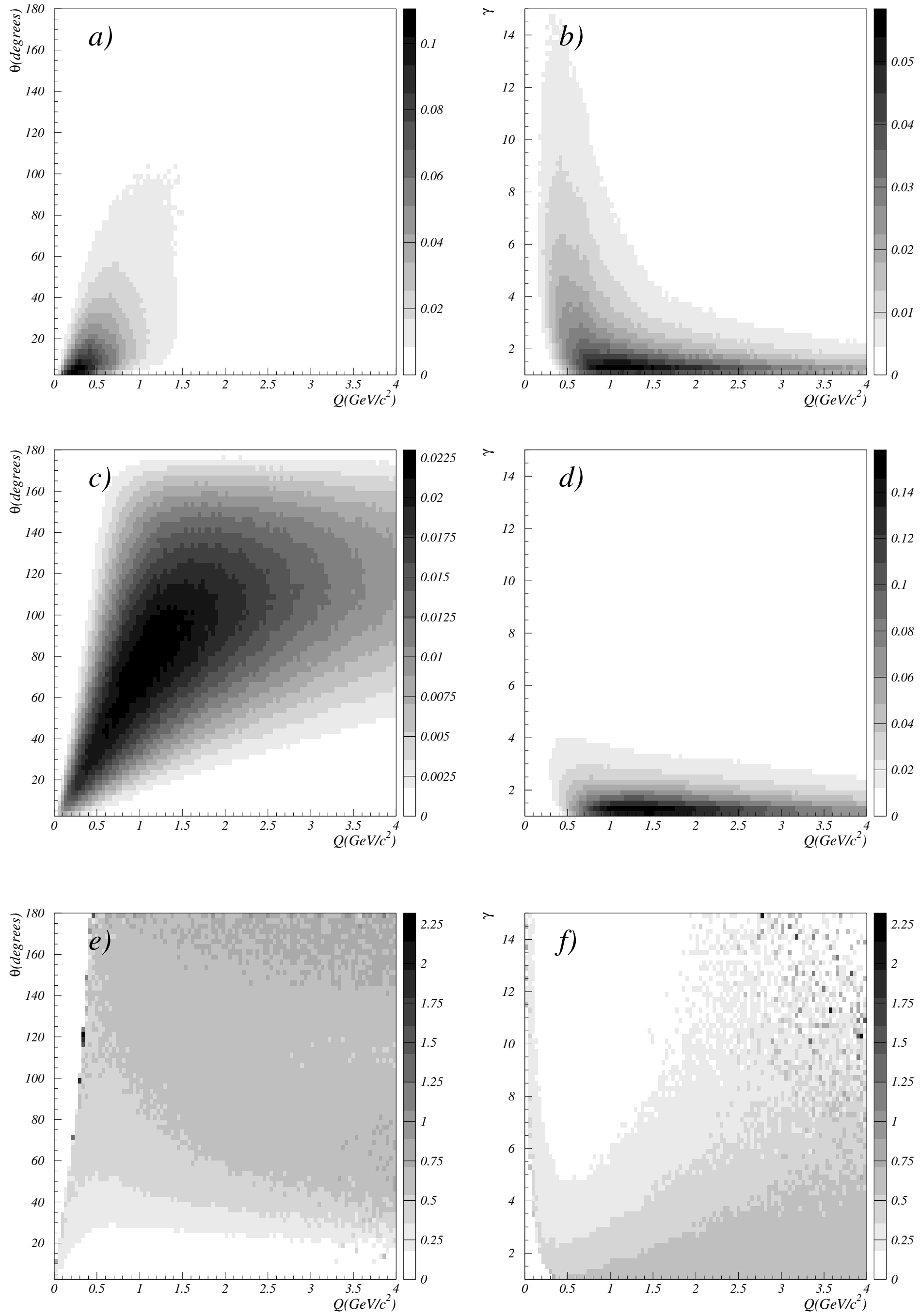

Figure 4.23: The opening angle θ, respectively their Lorentz boost γ vs Q for a)(b) pairs coming from the same W, c)(d) from different W's and e)(f) the ratio different/all pairs.

sample/parameter	Λ	$R(fm)$	δ	N	χ^2 (97 NDF)
no weights used					
BEfull	0.2394 $\pm$ 0.0082	0.845 $\pm$ 0.029	0.00338 $\pm$ 0.00073	0.9784 $\pm$ 0.0028	190.9
BEins	0.0125 $\pm$ 0.0084	0.845	-0.0038 $\pm$ 0.0011	1.0021 $\pm$ 0.0037	88.1
ARIADNE	-0.0027 $\pm$ 0.0096	0.845	-0.0002 $\pm$ 0.0011	0.9922 $\pm$ 0.0046	95.3
HERWIG	-0.0068 $\pm$ 0.0094	0.845	-0.0014 $\pm$ 0.0011	0.9944 $\pm$ 0.0047	79.2
JETSET	-0.0110 $\pm$ 0.0094	0.845	-0.0024 $\pm$ 0.0011	0.9980 $\pm$ 0.0045	73.5
ARIADNE CR	-0.0097 $\pm$ 0.0095	0.845	0.0055 $\pm$ 0.0011	0.9641 $\pm$ 0.0044	106.5
HERWIG CR	-0.0145 $\pm$ 0.0094	0.845	-0.0091 $\pm$ 0.0011	1.0247 $\pm$ 0.0049	94.3
JETSET SK1	0.0320 $\pm$ 0.0097	0.845	0.0076 $\pm$ 0.0011	0.9615 $\pm$ 0.0045	143.3
Data-Bg1	0.135 $\pm$ 0.053	0.845	0.0035 $\pm$ 0.0064	0.983 $\pm$ 0.025	93.4
Data-Bg2	0.124 $\pm$ 0.053	0.845	0.0038 $\pm$ 0.0064	0.980 $\pm$ 0.025	93.2
weights used					
BEfull	0.360 $\pm$ 0.012	0.994 $\pm$ 0.030	0.00375 $\pm$ 0.00094	0.9747 $\pm$ 0.0035	218.7
BEins	0.018 $\pm$ 0.011	0.994	-0.0030 $\pm$ 0.0013	0.9998 $\pm$ 0.0052	95.3
ARIADNE	-0.013 $\pm$ 0.012	0.994	0.0023 $\pm$ 0.0014	0.9851 $\pm$ 0.0051	113.7
HERWIG	-0.003 $\pm$ 0.012	0.994	0.0008 $\pm$ 0.0014	0.9881 $\pm$ 0.0052	86.1
JETSET	-0.023 $\pm$ 0.012	0.994	0.0005 $\pm$ 0.0012	0.9961 $\pm$ 0.0050	87.6
ARIADNE CR	-0.0080 $\pm$ 0.011	0.994	0.0057 $\pm$ 0.0011	0.9637 $\pm$ 0.0043	107.0
HERWIG CR	-0.023 $\pm$ 0.012	0.994	-0.0082 $\pm$ 0.0013	1.0232 $\pm$ 0.0054	96.7
JETSET SK1	0.0084 $\pm$ 0.012	0.994	0.0122 $\pm$ 0.0014	0.9486 $\pm$ 0.0050	183.5
Data-Bg1	0.241 $\pm$ 0.075	0.994	0.0044 $\pm$ 0.0078	0.980 $\pm$ 0.029	89.2
Data-Bg2	0.224 $\pm$ 0.075	0.994	0.0053 $\pm$ 0.0078	0.975 $\pm$ 0.029	89.1

Table 4.6: Summary of the results of fits, using Eq. 4.22 to Monte Carlo models including Bose-Einstein correlations between all identical bosons (BEfull), correlations between identical bosons coming from the same W only (BEins), containing no Bose-Einstein correlations at all (ARIADNE, HERWIG, JETSET) and samples with colour reconnection (CR). Fits to the combined data sample, subtracting Bg1 (standard method) and subtracting Bg2 (alternative background) are also given. For comparison, the results with and without pair weights are given. All results are obtained with a fully-hadronic selection with a purity of 92%, corresponding to a neural network cut $NN > 0.6$. In all fits, the R parameter is fixed to the value obtained from the BEfull Monte Carlo sample. All results are given for like-sign pairs.

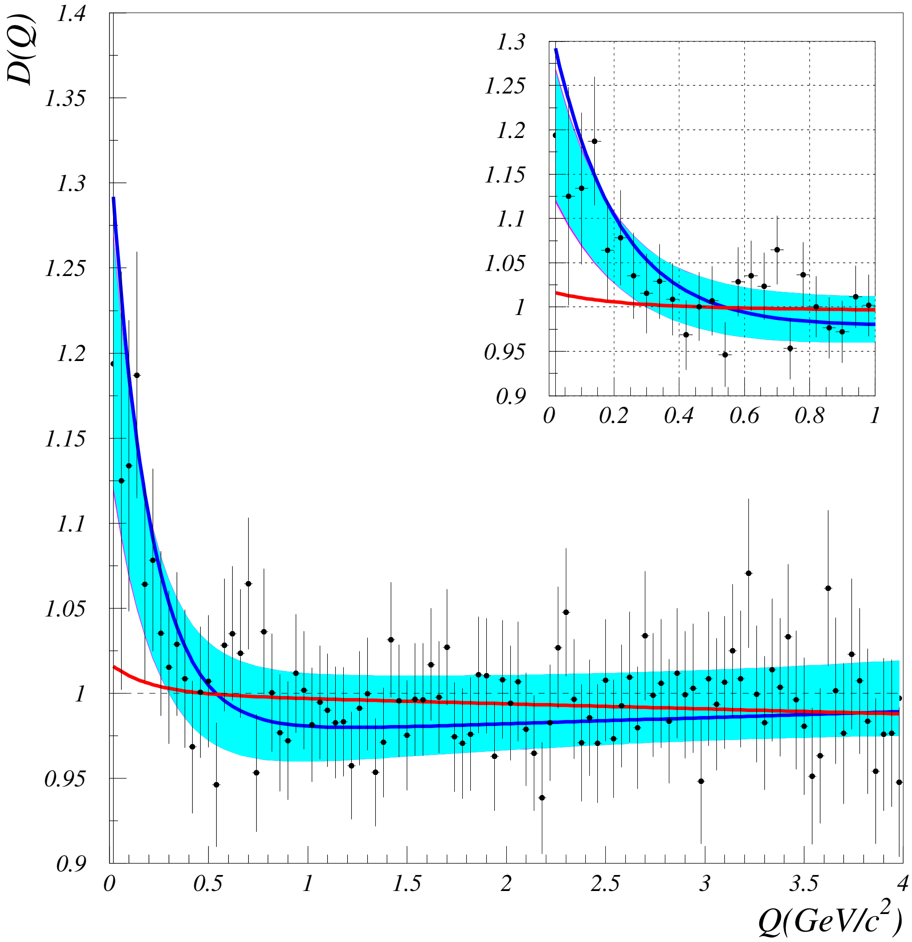

Figure 4.24: The $D(Q)$ distribution for the combined data set. The band indicates the fit result with the R parameter fixed to the one obtained from the BEfull model. The shape of the band includes the correlation between the remaining free fit parameters. In addition the fit to the BEfull and BEins model are shown by the full lines. The inset is a zoom in the Q region below 1.GeV/c^2

Parameter	Λ	δ	N
Λ	1.	0.09	-0.10
δ	0.09	1.	-0.74
N	-0.10	-0.74	1.

Table 4.7: The correlation coefficients between the parameters Λ, δ and N

energy (GeV)	$\Lambda(\pm,\pm)$	$\Lambda(+,-)$
189	0.34 $\pm$ 0.14	0.39 $\pm$ 0.10
192-196	0.31 $\pm$ 0.15	0.12 $\pm$ 0.10
200-202	0.06 $\pm$ 0.13	-0.064 $\pm$ 0.085
$>$ 202	0.15 $\pm$ 0.13	0.088 $\pm$ 0.085
combined	0.241 $\pm$ 0.075 $\pm$ 0.038	0.123 $\pm$ 0.050 $\pm$ 0.042
BEfull	0.360 $\pm$ 0.012	0.0785 $\pm$ 0.0057

Table 4.8: A summary of the final results for fits with the parameter R fixed to 0.994 fm. The second error indicated in row (6) is the total systematic uncertainty.

4.8 Systematic uncertainties

The measurement of inter-W Bose-Einstein correlations by means of the $D(Q)$ distribution proves to be intricate from a statistical point of view. However, due to the fact that, in this analysis data are directly compared with data, it has only limited systematic uncertainties.

The total systematic uncertainty on the measured Λ value is the sum in quadrature of the contributions listed in Tab. 4.10 for both like-sign and unlike-sign particle pairs. The individual contributions can be attributed to the following sources:

- As already mentioned in previous sections, 8% of total selected fully-hadronic events consists of $q\bar{q}(\gamma)$ background events. It is not precisely known how strong the Bose-Einstein correlations in these events are. It was found that the BE_{32} model with an input parameter strength of PARJ(92)=0.9 gives a good description of Z^0 events having a clear four-jet topology at 91.2 GeV. An alternative sample of background events was created, having an equal mixture of simulated events with PARJ(92)=0.9 and PARJ(92)=1.35. The latter input strength describes better the inclusive Z^0 sample. Both background samples were subtracted from the data and the absolute difference in the final result was taken as a systematic uncertainty due to the lack of knowledge about BEC in $q\bar{q}(\gamma)$ events.

- Secondly, the selection of the data and the way in which the mixed reference sample was created can introduce distortions in the two-particle densities. This would result in a non-zero value of Λ, measured in Monte Carlo samples without inter-W BEC. Since it is not known which fragmentation model gives the best description of two-particle densities in the absence of BEC, all available fragmentation models were used. The largest absolute value of the measured Λ for these models was taken as a measure for

sample/parameter	Λ	$R(fm)$	δ	N	χ^2 (97 NDF)
R fixed to R(BEfull)					
data ($\pm$,$\pm$)	0.241 $\pm$ 0.075 $\pm$ 0.038	0.994	0.0044 $\pm$ 0.0078	0.980 $\pm$ 0.029	89.2
data (+,-)	0.123 $\pm$ 0.050 $\pm$ 0.042	0.471	0.0112 $\pm$ 0.0082	0.965 $\pm$ 0.029	93.0
R free					
data ($\pm$,$\pm$)	0.38 $\pm$ 0.16 $\pm$ 0.038	1.63 $\pm$ 0.53	0.0027 $\pm$ 0.0077	0.987 $\pm$ 0.029	87.5
data (+,-)	0.131 $\pm$ 0.059 $\pm$ 0.045	0.58 $\pm$ 0.36	0.0101 $\pm$ 0.0086	0.970 $\pm$ 0.036	92.8
BEfull ($\pm$, $\pm$)	0.360 $\pm$ 0.012	0.994 $\pm$ 0.030	0.00375 $\pm$ 0.00094	0.9747 $\pm$ 0.0035	218.7
BEfull (+,-)	0.0785 $\pm$ 0.0057	0.471 $\pm$ 0.045	0.0030 $\pm$ 0.0010	0.9792 $\pm$ 0.0039	119.0

Table 4.9: Fit results to like-sign and unlike-sign D(Q) with R fixed and R free. The second error on the data Λ values corresponds to the systematic error.

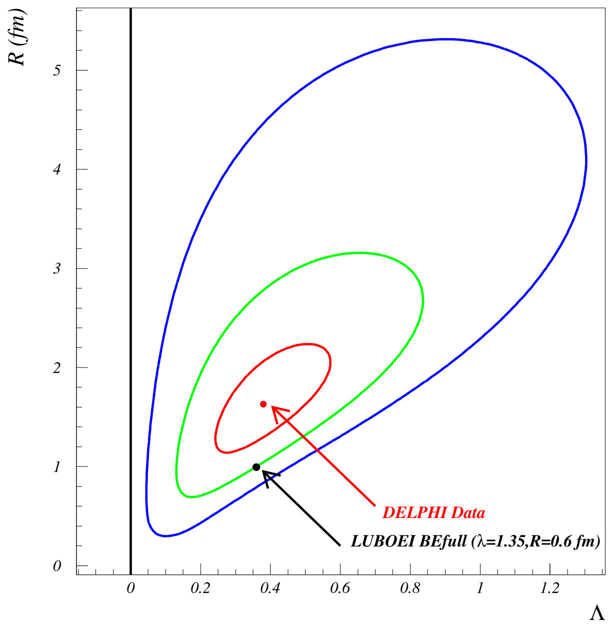

Figure 4.25: The one, two and three σ contours for a fit to the combined data set, leaving the R parameter free. The fit result obtained from the BEfull model is indicated for comparison (the statistical errors on this measurement are smaller than the size of the dot).

syst source	contribution to $\Lambda(\pm,\pm)$	contribution to $\Lambda(+,-)$
background shape	0.017	0.005
cuts & mixing	0.023	0.028
Colour Reconnection (HER)	0.020	0.030
Variation of R	0.014	0.005
Total syst.	0.038	0.042

Table 4.10: A breakdown of the systematic errors for the Λ measurement with fixed R, for like-sign and unlike-sign particle pairs.

the influence of selection procedures and mixing method on our measurement.

- Fixing the R parameter to a value obtained from the BEfull model, neglects the correlations between Λ and R and reduces the statistical error on Λ. In order to take this correlation into account, the R parameter was varied within one standard deviation of its value, measured for the BEfull model. The resulting difference in the Λ value, measured from the data was taken as a systematic uncertainty due to neglection of the statistical correlations between Λ and R.

- A last systematic uncertainty was attributed to the Colour Reconnection (CR) effect. This effect could have, in addition to inter-W BEC drastic consequences for the W mass measurement in the fully hadronic channel [63, 64]. As in BEC, it violates the assumption that the two produced W bosons decay independently of each other.

  Colour reconnection occurs when independent colour singlets interact strongly before hadron formation. In fully hadronic W decays it recombines partons from different parton showers. After fragmentation, the resulting hadrons carry therefore a mixture of energy-momentum of both original showers [79].

  The colour reconnection effect has been modeled in various ways [63, 64, 66]. Only the extreme model SK1 [63], where reconnection occurs in all events has been ruled out by the LEP expermiments [65], however the absence of colour reconnection is also disfavoured.

  For this reason, three possible models of colour reconnection, implemented in JETSET, ARIADNE and HERWIG, were used to estimate their influence on our measurement. The fit results for these models are given in Tab. 4.6 and are marked with the suffix "CR". The maximum difference in Λ between the CR samples and their equivalent models without CR implementation was taken as systematic uncertainty due to the colour reconnection effect. In our case the HERWIG implementation of CR yields the largest value.

From a comparison of the statistical uncertainty on the measured Λ value with the total systematic uncertainty we conclude that the inter-W BEC measurement is mainly statistically limited. This is due to the small fraction of particle pairs at smalll Q which come from different W's. In addition, the inter-W effect seems to be situated in a very small Q region, corresponding to a relatively large value of R. The two-particle densities are poorly populated in this region. This is however good news for the impact on the W mass measurement, since it means that in practice, very few particles contribute to the inter-W Bose-Einstein effect. The reconstructed W mass is therefore probably little affected by this small number of particles.

4.9 Summary

In this chapter, we presented studies of inter-W Bose-Einstein correlations, based on an analysis of 550 pb^{-1} of LEP2 data with centre-of-mass energies ranging from 189 - 209 GeV. An event mixing method is used to extract a signal indicating inter-W Bose-Einstein correlations. The analysis is optimized as function of the purity of the fully-hadronic event sample. The sensitivity to inter-W BEC is increased by giving weights to pairs, according to their probability to come from different W's. The mixing method, including the pair weights is highly model independent, since data are compared directly with data. As a consequence, many systematic uncertainties due to detector acceptance and resolution, selection procedures and corrections are eliminated. The remaining systematic uncertainties are dominated by the modeling of the background shape, the mixing procedure itself and the possible presence of colour reconnection effects.

A non-zero value of Λ was found when fitting the $D(Q)$ distribution for like-sign pairs, giving an indication for inter-W Bose-Einstein correlations, at the level of three standard deviations. The final result is

$$\Lambda = 0.241 \pm 0.075(\mathrm{stat}) \pm 0.038(\mathrm{syst}). \tag{4.28}$$

A significant signal was also found in unlike-sign pairs, in accordance with the predictions of LUBOEI. All results on the fitted values of Λ are summarized in Tab. 4.8.

4.10 Concluding remarks

The results obtained in this analysis give a indication for inter-W BEC. Previous analysis in DELPHI have caused confusion over the years, due to the repeated observation [80, 81] and non-observation [82] of the inter-W BEC signal. The results described in this thesis should be the final DELPHI statement on the subject. The difference between the analysis not observing evidence for inter-W BEC cannot be pinpointed to a single feature. Many things are different and have been optimized over time, i.e. the event selections, the mixing procedure, background subtraction and the correct treatment of all statistical errors and fits. The remaining surprise is the large effect observed in the unlike-sign pairs (half of the effect observed in like-sign pairs).

Two schools exist when it comes to the interpretation of inter-W BEC in unlike sign pairs. In principle unlike-sign pairs are not subjected to BEC, however the fact that both positive and negatively charged pions are mutually pulled closer in energy-momentum space also has its influence on the separation of unlike-sign pairs. Moreover, transverse momentum is known to be conserved locally and total energy-momentum conservation is conserved globally. Therefore, the reflection of Bose-Einstein correlations in unlike-sign pairs inside a single W is known and widely accepted. Whether the same mechanism should describe the observation of inter-W BEC in unlike-sign pairs is not clear. The LUBOEI models, although their implementation of BEC is rather ad-hoc, confirm this hypothesis.

Global rescaling models describing inter-W BEC, which are at present unavailable at full simulation level, might shed light on this situation.

4.10.1 Other LEP results

Much activity is still going on in other LEP experiments to confirm or disprove our results. The L3 collaboration has already published a result based on the same methods as used in this thesis [77]. The result based on the integral of $\Delta\rho(Q)$ and a fit to the ratio $D'(Q) = D(Q)_{\mathrm{data}}/D(Q)_{\mathrm{MC}nointer-WBE}$ do not indicate the presence of inter-W BEC. In Fig. 4.26 the $D(Q)$ and $D'(Q)$ distrubutions of the L3 published analysis [77] are shown. Their measurement, using a dataset with similar statistics, based on a fit to $D'(Q)$, using

$$D'(Q) = (1 + \delta Q)(1 + \Lambda \exp(-\kappa^2 Q^2)), \tag{4.29}$$

yielded a Λ value of

$$\Lambda = 0.008 \pm 0.018\ (stat) \pm 0.012\ (syst). \tag{4.30}$$

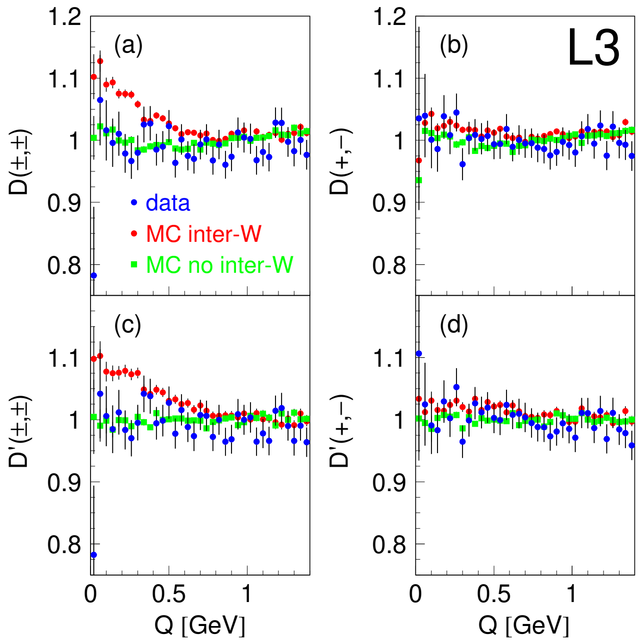

Figure 4.26: The $D(Q)$ and $D'(Q)$ distributions, taken from the published L3 results [77].

Arguments against using integrals of $\Delta\rho(Q)$ are given in this thesis, while it should be noted that the $D'(Q)$ distribution is not as model independent as $D(Q)$. Both might give an indication for the different conclusions drawn by DELPHI and L3.

Final results from the ALEPH and OPAL collaborations using this method and the total available LEP2 statistics have not been released yet. The ALEPH collaboration reports [83, 84] that the LUBOEI model, tuned and corrected at the Z resonance for light quarks describes the data when only intra-W BEC are implemented, while the inter-W model is disfavored at the level of 2.7 standard deviations. In [83] only one third of the available LEP2 statistics was used, while [84] uses all available data, but introduces model dependency by redefining $\Delta\rho(Q)$ as $\Delta\rho(Q) = \Delta\rho(Q)_{\rm data} - \Delta\rho(Q)_{\rm MCnoBE}$. The OPAL collaboration, using only part of the available LEP2 statistics remained inconclusive [85, 86] due to lack of statistics and sensitivity of their method.

4.10.2 Influence of inter-W BEC on the reconstructed W mass

Despite the lack of final results from all LEP collaborations, regular LEP wide combinations of the available results are made [65]. This is done, using a χ^2 combination of the observed fraction of the BEfull model, defined as

$$\Lambda_{frac} = \frac{\rm data - model(noBE)}{\rm model(BEfull) - model(noBE)}. \tag{4.31}$$

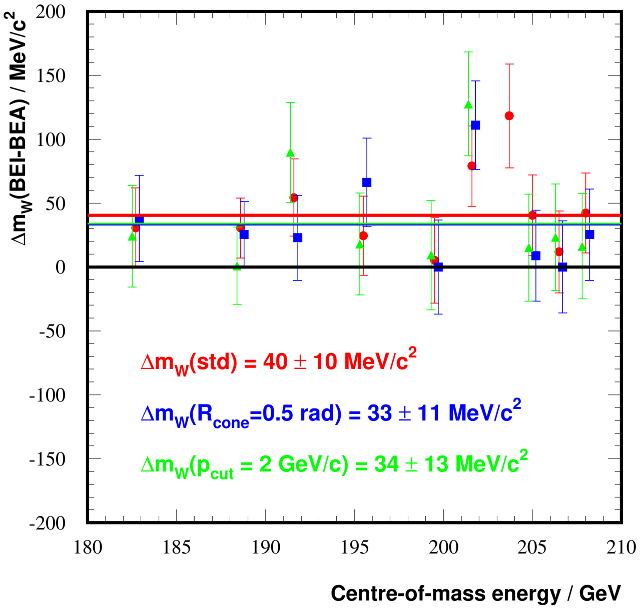

Figure 4.27: The difference in reconstructed W mass between the BEfull and BEins model, using the DELPHI W mass analysis in the fully-hadronic channel. *J. D'Hondt, private comm.*

The obtained result and its total error is translated into a W mass shift by

$$\Delta M_W = (\Lambda_{frac} + \sigma(\Lambda_{frac})) \times [M_W(BEfull) - M_W(noBE)]. \tag{4.32}$$

The latest combination [65], including only the ALEPH and L3 published results, quotes a value of $\Lambda_{frac} = 0.03 \pm 0.18$, resulting in a W mass uncertainty due to BEC of 7 MeV/c^2 (1 σ limit).

Within DELPHI, the shift due to inter-W BEC is estimated using the LUBOEI BEfull model, using at input parameters λ and r the values tuned on inclusive Z^0 data (PARJ(92)=1.35, PARJ(93)=0.6 fm). The difference between the reconstructed W mass in the fully-hadronic channel for the BEfull model and the BEins model is shown in Fig. 4.27 as function of the centre-of-mass energy. The dependence on the centre-of-mass energy is flat, resulting in a general negative W mass shift of 40 MeV/c^2.

Applying the same method as used in the LEP combinations (see Eq. 4.32) and using the measurement described in this thesis, would result in a W mass shift of 36.1 MeV/c^2. The overall LEP result, including the DELPHI final result will therefore give shifts in between the quoted values of 7.0 and 36.1 MeV/c^2. The current value of the W boson mass, obtained from direct reconstruction, combined over all four LEP experiments amounts at the moment [65] to

$$m_W(direct) = 80.448 \pm 0.030(stat) \pm 0.030(syst) GeV/c^2, \tag{4.33}$$

The overall contribution to the total systematic uncertainty due to inter-W BEC is 9 MeV/c^2, and 35 MeV/c^2 in the fully-hadronic channel only [65].

Chapter 5

Bose-Einstein Correlations in three jet events

The analysis of hadronic WW events showed an indication of the presence of Bose-Einstein correlations between identical bosons from different W's. This has some implications for a precise W mass measurement in the fully-hadronic channel. The Lund string interpretation of hadronic decay makes this observation even more interesting, since in this picture the strings spanned between the primary quarks originating from the decay of each W are assumed to decay independently. The presence of inter-W BEC seems to contradict this assumption.

LEP provides another system where two strings or string pieces decay independently: namely hadronic Z^0 decays where one of the primary quarks radiates a hard gluon. These three-jet Z^0 events are quite simple to select and are abundantly present in LEP1 data, where the centre-of-mass energy was tuned to the resonant Z^0 production. The topology of these events consists of two string pieces spanned between the gluon tip and the two primary quarks as indicated in Fig. 5.1. The distance between the two strings in a typical three-jet Z^0 event is smaller than the average distance between the strings in a WW decay. This should result in a higher sensitivity to the inter-string BEC phenomenon.

The structure of this chapter is as follows. First, the selection of hadronic Z^0 events is briefly explained, and the separation between b-quark decays and light quark decays is discussed, using the DELPHI b-tag algorithm. Secondly, the identification of gluon jets, based on the CAMBRIDGE clustering algorithm, is discussed. Finally, we measure two-particle correlations in two- and three-jet events, and compare with WW events. This is followed by a comparison between quark jets and gluon jets, individually.

5.1 The selection of hadronic Z^0 events

The selection of hadronic Z^0 events, where the Z^0 decays into a quark-antiquark pair, possibly with the radiation of one or more hard gluons, is quite straightforward. The cross-section at the Z^0 resonance is high, and background processes like beam gas events, cosmic rays, two-photon collisions, leptonic Z^0 decays, can easily be eliminated by requiring a minimum number of charged particles and a large amount of energy deposited in the detector.

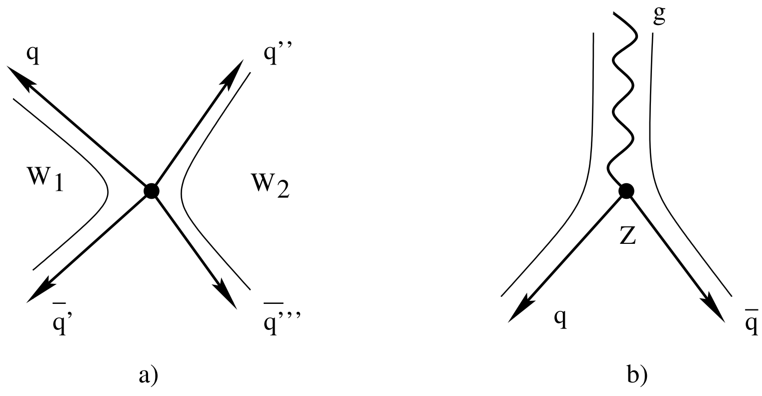

Figure 5.1: Comparison of the string picture of a) a fully hadronically decaying WW event and b) a three-jet Z^0 event

The track selection for this analysis is slightly stricter than the one used for the study of WW events in order to be compatible with LEP1 analyses in DELPHI. The selection of hadronic Z^0 events and the technique to identify gluon jets is largely based on [87].

Charged tracks were required to have

- momentum larger than 300 MeV/c;
- polar angle between 20 and 160 degrees;
- impact parameter in the $r\phi$ plane smaller than 5.cm;
- impact parameter in the z plane smaller than $10.\mathrm{cm}/\sin(\theta)$;
- a minimum track length of 30 cm;
- a relative error on the momentum measurement smaller than 100%.

Neutral tracks were required to have

- energy in the HPC larger than 500 MeV and smaller than 50 GeV;
- energy in the forward electromagnetic calorimeter larger than 500 MeV and smaller than 30 GeV;
- Energy in the hadron calorimeter larger than 1 GeV and smaller than 50 GeV.

The hadronic events were selected by requiring that

- the charged visible energy is larger than 15% of the center-of-mass energy;
- the charged energy in each detector hemisphere is larger than 3% of the centre-of-mass energy;
- the event contains at least 5 charged tracks;

- the polar angle of the smallest sphericity axis is larger than $30°$ and smaller than $150°$
- none of the charged particles has a momentum larger than 45. GeV.

5.1.1 Jet clustering

In the hadronic decay of a Z^0 boson into a quark-antiquark pair, perturbative QCD predicts the probability for a gluon to be radiated with a given transverse momentum p_t:

$$\frac{d\sigma}{dp_t} \propto \frac{\alpha_s(p_t)}{p_t}. \tag{5.1}$$

This means that a fraction of these decays will have a three-jet topology. The fraction of three-jet events depends on the clustering algorithm used and the jet resolution variable. QCD predictions are therefore tested in function of these clustering algorithms and resolution variables.

The Bose-Einstein analysis in three-jet events uses two different clustering algorithms. One will be used to cluster the event in a free number of jets for a fixed resolution variable. The LUCLUS [47] algorithm is chosen for this purpose. The principles of a jet clustering algorithm were already discussed in the previous chapter, but some special attention to the CAMBRIDGE algorithm [88] will be given.

The CAMBRIDGE algorithm

For the selection of gluon jets, the CAMBRIDGE algorithm [88] is the most suited. It is known to reduce the formation of so called 'junk' jets, i.e. the combination of particles originating from two nearby soft gluons into one jet. The CAMBRIDGE algorithm is a modification of the DURHAM algorithm. It differs from other clustering algorithms since it has two distance measures instead of one. One is used as an ordering variable while the other is a resolution variable. In practice, the algorithm starts with a table of N primary objects, the N particles' four-momenta. The clustering starts with the pair of particles having the smallest ordering variable

$$\varepsilon_{ij} = 2(1 - \cos\theta_{ij}), \tag{5.2}$$

where θ_{ij} represents the angle between the particle momenta. The test variable

$$y_{ij} = \frac{2 \cdot min(E_i^2, E_j^2)(1 - \cos\theta_{ij})}{s} \tag{5.3}$$

determines when the clustering stops. The sequence of the algorithm is as follows:

- If one object remains, it is separated as a jet and the iterative procedure stops.
- The pair i,j with the smallest orderings variable ε_{ij} is determined and its test variable y_{ij} is calculated.

- If $y_{ij} < y_{cut}$ then objects i and j are combined into a new object by simply adding the four momenta (recombination scheme). The previous objects i and j are removed from the object table and replaced by the newly created object.
- If $y_{ij} > y_{cut}$ then object i or j, having the largest energy, is separated as a new jet and its entry removed from the object table. The object with the smallest energy of the two remains in the table.

This procedure is known as 'Soft Freezing', since it isolates objects with smaller energies first.

In contrast to other clustering algorithms, the clustering sequence of the CAMBRIDGE algorithm depends on the value of y_{cut}. An important feature of this scheme is that an event can flip from a configuration with n jets to a configuration with m jets, where n and m can be non-consecutive numbers. The solution is given by [88]: While performing the clustering for a particular value of y_{cut}, denoted by y_{init}, one keeps track of the maximum value of y_{ij}. The maximum value of y_{ij} is retained. For any value $y_{cut} > y_{ij}^{max}$ the algorithm will follow the same clustering sequence. For values of y_{cut} smaller than y_{ij}^{max}, the condition $y_{ij} \geq y_{cut}$ is satisfied at least once more and the subsequent clustering sequence may change completely. In order to force the event into a three-jet configuration, the following procedure was followed:

1. Start with a value $y_{init} = 1$ and set $y_{cut} = y_{init}$.
2. Perform the CAMBRIDGE clustering and keep track of all values y_{ij} between all objects i and j. Retain the maximum value y_{ij}^{max}.
3. Store the value of y_{ij}^{max}, the number of jets, n, and the jet information. The clustering for $y_{cut} > y_{ij}^{max}$ is now completely determined.
4. The algorithm stops if the desired number of jets, in our case 3, is reached.
5. Set $y_{cut} = y_{ij}^{max}$ and go to step 2.

In a few cases the desired number of three jets will never be reached. As a consequence these events are discarded for further analysis.

5.2 Study of light quark events

It is known that, due to the long life-time of B-mesons, Bose-Einstein correlations in hadronic b-quark decays are suppressed. It is therefore necessary to select a light (udsc) quark sample to compare two-jet events with three-jet events. On the other hand, if one wants to select gluon jets with a high purity, the tagging of the quark jets by their probability to be a b-quark, thus separating them from the gluon jet, is an essential tool. The DELPHI B-tagging algorithm [89, 90] allows for an efficient separation of light quark decays and b-quark decays, both for events and individual jets, and is discussed below. Further information on the DELPHI b-tag algorithms can be found in [91].

5.2.1 B -tagging

B-hadrons, formed after the hadronisation of an event with primary b quarks, have different properties than other hadrons. They decay under the weak interaction where a b quark decays into a c-or a u-quark according to the CKM matrix elements $|V_{cb}|$ and $|V_{ub}|$. These elements are very small, resulting in a long life-time of a B-hadron (1.54 ps) allowing it to travel several millimetres in the detector before decaying. This results in particles originating from the B-hadron decay having large impact parameters w.r.t. the primary vertex. These impact parameters are on average around $400\mu m$, which can be resolved using the DELPHI Vertex Detector.

Lifetime tag

The impact parameters in the $R\phi$ plane and Rz plane provide the main variable for the b-tagging. For each track, two significances $S_{R\phi}$ and S_{Rz} are computed, which are the ratio of the impact parameters to their errors. The sign of the impact parameter is determined by the point of closest approach in space of the track with respect to its estimated flight direction. This flight direction is, in the simplest case, the jet direction to which the particle belongs. In the case where a track is assigned to a reconstructed secondary vertex, it is defined as the direction from the primary vertex to this reconstructed secondary vertex. The impact parameter sign is then positive (negative) when the point of closest approach is downstream (upstream) w.r.t. to the primary vertex position. With this definition, tracks from decays of long lived particles have predominantly positive signs, while tracks coming from the primary vertex have equal probabilities to have a positive or negative sign. The normalised significance distribution from tracks with negative impact parameter signs, $f(S)$, is then used to construct a track probability function $P(S^0)$, assuming that $P(S^0)$ is the same for primary tracks with either positive or negative significance:

$$P(S^0) = \int_{S^0}^{\infty} f(S)\, dS. \tag{5.4}$$

By definition, tracks from the primary vertex have a flat distribution of $P(S^0)$ between 0 and 1, while tracks coming from long-lived decays have predominantly low track probabilities. Using the track probabilities one can calculate the probability for any given set of N tracks that they are originating from the primary vertex by:

$$P_N = \prod \sum_{j=0}^{N_{r\phi}+N_{Rz}-1} (-\log(\prod)^j/j!, \tag{5.5}$$

where

$$\prod = \prod_{i=1}^{N_{R\phi}} P(S^i_{R\phi}) \cdot \prod_{i=1}^{N_{Rz}} P(S^i_{Rz}). \tag{5.6}$$

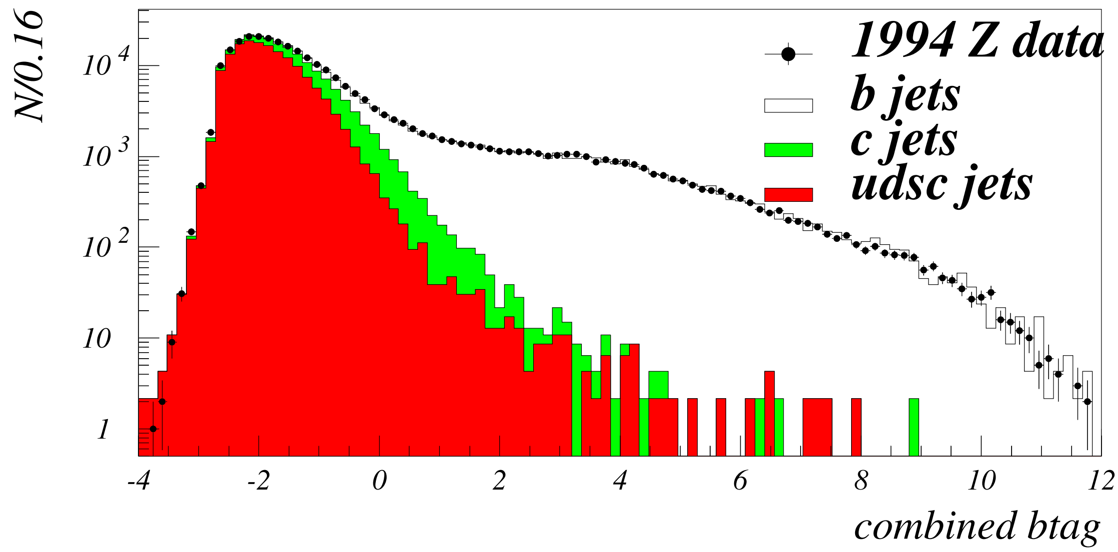

Figure 5.2: A data/MC comparison for the combined event b-tag, the shaded histograms correspond to the light quark flavors, while the open histogram corresponds to events containing b-quarks.

Combined tagging

The impact parameter probability proves to be already a powerful method to separate events containing b-quark decays from events with lighter quarks. However, one can exploit the properties of B-hadrons further to enhance the separating power. Therefore, in addition to the lifetime probability, five additional discriminating variables are computed, provided that jets with a reconstructed secondary vertex are found:

- The mass of particles combined in the secondary vertex, M_s:
  The mass of the secondary vertex in a jet is higher for c- and b-jets, due to the higher masses of c and b-hadrons.

- The fraction of the charged jet energy included in the secondary vertex, X_s^{ch}:
  This reflects the differences in the fragmentation properties of light and heavy quarks.

- The transverse momentum at the secondary vertex, P_s^t:
  It is defined as the resultant transverse momentum with respect to the B-hadron's estimated flight direction of all particles attached to the secondary vertex. This transverse momentum can arise from neutrino's originating from semi-leptonic decays, neutral particles or non-reconstructed charged particles. For b-quark jets the value of P_s^t tends to be higher than for light quark jets.

- The rapidity of each track included in the secondary vertex, R_s^{tr}:
  Although B-hadrons are produced on average with a higher energy, the rapidities of

particles from B-decays are less than those from D-meson decays. This is mainly due to the high B-hadron mass.

- The transverse momentum of an identified energetic lepton, P_l^t:
  In the case where B-hadrons decay semi-leptonically ($\approx 11\%$) the transverse momentum of the lepton with respect to the B-hadron's flight direction can be exploited. Due to the high B-hadron mass this transverse momentum is expected to be larger for b-jets than for light quark jets.

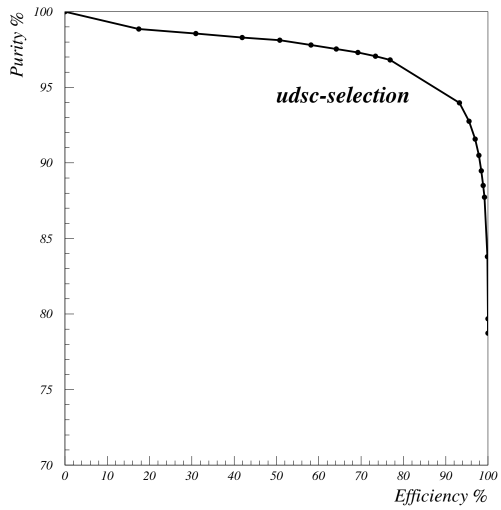

Figure 5.3: The efficiency versus purity for the selection of a light quark (udsc) sample from hadronic Z^0 decays.

This whole set of variables on jet level can than be combined into a combined tagging variable:

$$y = \prod_{i=1,n} y_i, \tag{5.7}$$

where $y_i = f_i^{bgd}(x_i)/f_i^{sig}(x_i)$, with $f_i^{bgd}(x_i)$ and $f_i^{sig}(x_i)$ being the probability density functions of the discriminating variable x_i for background and signal respectively. The backgrounds (corresponding to either c-quarks or u,d,s-quarks) have different behaviour in the variables entering into the combined b-tag procedure. This can be taken into account by modifying the combined b-tag variable y:

$$y = n_c \prod \frac{f_i^c(x_i)}{f_i^b(x_i)} + n_q \prod \frac{f_i^q(x_i)}{f_i^b(x_i)}, \tag{5.8}$$

where n_c and n_q (q=u,d,s) are the normalised numbers of c and light quark jets with a reconstructed secondary vertex in $c\bar{c}$ and $q\bar{q}$ events respectively. The jets are tagged as being a b-jet if the value $y < y_0$ where y_0 can be varied to obtain a desired purity and efficiency. A comparison plot between data and MC is shown in Fig. 5.2 for the combined event b-tag variable ($-\log_{10}(y)$).

5.3 Correlations in two- and three-jet events

After the hadronic selection, a light quark subsample of hadronic Z^0 decays is used. For this purpose the life-time b-tag variable is used. In Fig. 5.3 the efficiency versus purity of an udsc-quark sample is shown for various life-time b-tag cuts. The working point is chosen at an efficiency of 58% and a purity of 98%, corresponding to a value of $-\log 10(\mathrm{blife}) < 0.5$.

The udsc sample is then clustered into natural jets using the LUCLUS algorithm with a jet resolution cut of $y_{\mathrm{cut}} = 4.0$. In order to select a clear two-jet topology, from all events having two jets, only the ones having a thrust value larger than 0.95 are selected for further analysis. The total amount of selected events after anti-b selection and jet clustering is shown in Table. 5.1, both for the collected data sample of 1994 and a Monte Carlo sample, using the KK2f generator.

sample	1994 data	MC no BE
hadronic events	1168038	1258842
udsc events	529857	584860
udsc 2 jet	269325	294189
udsc 3 jet	197111	227241

Table 5.1: Size of the data and MC reference samples after several selection steps. The luminosity of the Monte Carlo sample is not rescaled to the data luminosity.

5.3.1 The normalised density $\mathrm{R_2(Q)}$.

In order to compute the correlation functions for two- and three-jet events, a Monte Carlo sample, having no BEC implemented is taken as reference sample. We thus consider the quantity

$$R_2(Q) = \frac{\rho(Q)}{\rho(Q)_{\mathrm{MCnobe}}} \tag{5.9}$$

In [69] it is noted that in the case of two independent fragmenting sources, S, having no BEC between them, the following relation should hold if the two sources overlap 100% in momentum space:

$$R_2(2S) = \frac{1}{2}(1 + R_2(1S)), \tag{5.10}$$

where the notations $1S$ and $2S$ stand for a system of one and two sources, respectively. If there is no overlap at all between the two sources Eq. 5.10 becomes

$$R_2(2S) = R_2(1S). \tag{5.11}$$

In what follows, a fully-hadronic WW event or a three-jet Z^0 decay corresponds to the two-source, $2S$, analogy, while a semi-leptonic WW event or a two-jet Z^0 decay corresponds to the single source analogy, $1S$.

In [22] it was estimated that for WW events, the intercept at $Q = 0$ of $R_2(2S)$ should be 20% smaller than the intercept of $R_2(2q)$ in the absence of inter-W BEC. Similar behaviour is expected for two- and three-jet Z^0 events. The following section deals with a comparison of two- and three-jet Z^0 events. Due to the analogy with WW events a comparison will be made between two-jet Z^0 decays and semi-leptonic WW events and between three-jet Z^0 decays and fully-hadronic events.

5.3.2 Comparison of $\mathrm{R}_2(\mathrm{Q})$ in Z^0 and WW decays

In Sect. 5.2 it was already pointed out that the presence of B-meson decays reduces the Bose-Einstein decays in hadronic Z^0 decays. In WW events the amount of hadronic decays containing b-quarks is highly suppressed due to the small value of the relevant CKM matrix element. For a direct comparison with WW events it is therefore necessary to use light quark Z^0 decays, also denoted as "(udsc)" Z^0 events. The difference between the inclusive Z^0 sample and an (udsc) Z^0 sample, is shown in Fig. 5.4.

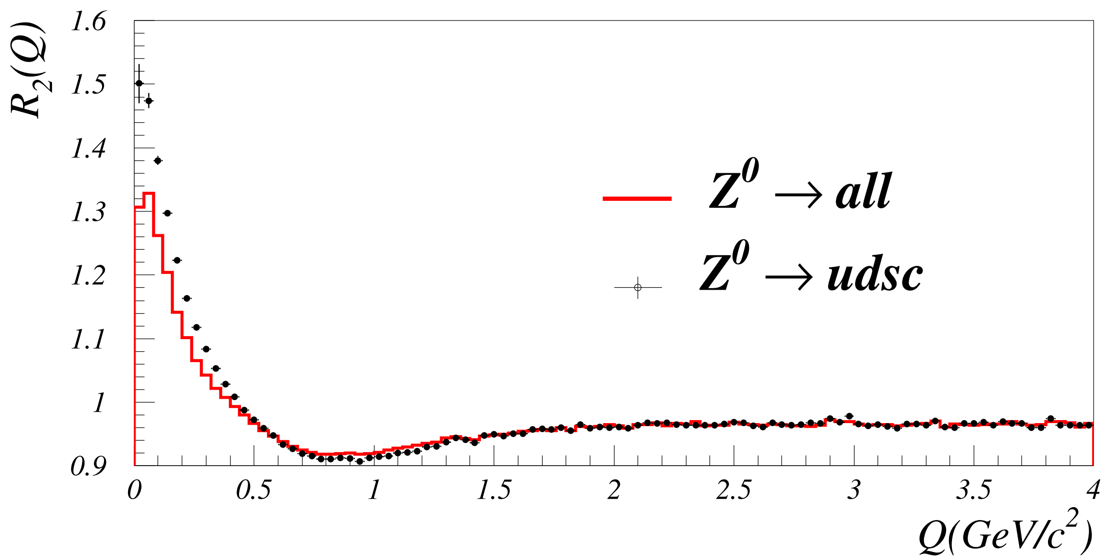

Figure 5.4: A comparison of the $R_2(Q)$ distribution for all hadronic Z^0 decays (full line) and (udsc) Z^0 events (points). The enhancement in $R_2(Q)$ due to the rejection of b-decays is clearly visible.

It is clear from the shape of $R_2(Q)$ in Fig. 5.4 that a simple exponential expression such as Eq. 4.22 is not able to describe the shape of this distribution. A fit to the total hadronic Z^0 sample, using Eq. 4.22 yields the results in Tab. 5.2. The very large χ^2 value indicates that a more sophisticated shape should be used to quantify our results.

To that end, the Laguerre expansion, proposed in [92], is used as a natural extension of

Eq. 4.22:

$$R_2(Q) = N(1+\delta Q)\big[1+\lambda\exp(-QR)(1+\alpha L_1(QR)+\beta L_2(QR))\big], \tag{5.12}$$

where L_1, L_2 are the first and second order Laguerre polynomials, defined as

$$L_1(t) = \quad t-1, \tag{5.13}$$
$$L_2(t) = \quad t^2-4t+2. \tag{5.14}$$

Note that we here adopt another notation of, λ, in order to avoid confusion with the Λ measured in the previous chapter. The results of the fit, using Eq. 5.12 is shown in the second column of Tab. 5.2. The reduction of the χ^2 value with more than a factor 5 indicates clearly that the Laguerre expansion is more suitable for the study of $R_2(Q)$. A comparison of the two fit functions is shown in Fig. 5.5. The six parameters in Eq. 5.12 are, however, so strongly correlated (more than 95%) that leaving them all free would make a comparison between different event classes meaningless. Therefore, in all following discussions, the parameters α and β will be fixed to the values obtained for the total hadronic Z^0 sample, $\alpha = 1.12$, $\beta = 0.597$.

Using Eq. 5.12 and fixing the parameters α and β, a comparison is made between data samples consisting of all Z^0 decays, (udsc) Z^0 decays, (udsc) two-jet events, (udsc) three-jet events, semi-leptonic WW events and fully-hadronic WW events. The values of all remaining four parameters are given in Tab. 5.3. The correlation between the four remaining fit parameters is given in Tab. 5.4. From Tab. 5.3 we can conclude that the (udsc) Z^0 sample has indeed a larger correlation strength, λ than the total Z^0 sample, including around 20% b-quark decays. The λ parameter, measured in two-jet Z^0 decays is 6% larger (relative) than that from three-jet Z^0 decays. This difference is small, compared to the expectations from two independent sources, given in the previous section. In Fig. 5.6 the $R_2(Q)$ distributions from two- and three-jet events are directly compared. The ratio $R_2(2jet)/R_2(3jet)$, is plotted on the bottom of Fig. 5.6.

The measured R parameter is also larger in three-jet events than in two-jet events. Comparing semi-leptonic WW events with fully-hadronic events, the measured λ parameter in

Parameter	exponential	Laguerre
N	0.907 $\pm$ 0.0007	0.833 $\pm$ 0.034
λ	0.655 $\pm$ 0.005	0.63 $\pm$ 0.15
δ	0.021 $\pm$ 0.0003	0.034 $\pm$ 0.010
R (fm)	1.032 $\pm$ 0.007	0.299 $\pm$ 0.007
α	–	1.120 $\pm$ 0.037
β	–	0.597 $\pm$ 0.056
χ^2 (96 NDF)	2547.5	414.3

Table 5.2: The results of a fit to the total hadronic Z^0 sample, using Eq. 4.22 and the second order Laguerre expansion of Eq. 5.12. The lower χ^2 value of the Laguerre fit indicates its better description of $R_2(Q)$.

Parameter/Sample	N	λ	δ	R (fm)	χ^2 (96 NDF)
$Z^0 \rightarrow$ all	0.8327 $\pm$ 0.0008	0.629 $\pm$ 0.004	0.0342 $\pm$ 0.0004	0.298 $\pm$ 0.001	414.3
$Z^0 \rightarrow$ udsc	0.779 $\pm$ 0.001	0.905 $\pm$ 0.008	0.0446 $\pm$ 0.0006	0.298 $\pm$ 0.001	201.0
(udsc) 2 jet	0.801 $\pm$ 0.002	0.943 $\pm$ 0.012	0.040 $\pm$ 0.001	0.287 $\pm$ 0.002	153.7
(udsc) 3 jet	0.738 $\pm$ 0.002	0.891 $\pm$ 0.011	0.0458 $\pm$ 0.0009	0.303 $\pm$ 0.002	155.8
semi-leptonic WW	0.843 $\pm$ 0.014	0.831 $\pm$ 0.080	0.0355 $\pm$ 0.0063	0.309 $\pm$ 0.015	115.1
fully-hadronic WW	0.865 $\pm$ 0.008	0.752 $\pm$ 0.046	0.0262 $\pm$ 0.0033	0.302 $\pm$ 0.010	159.1

Table 5.3: A comparison between the parameters of Eq. 5.12 from fits to the $R_2(Q)$ distributions, for several Z^0 samples, semi-leptonic and fully-hadronic WW events. All indicated errors are statistical only.

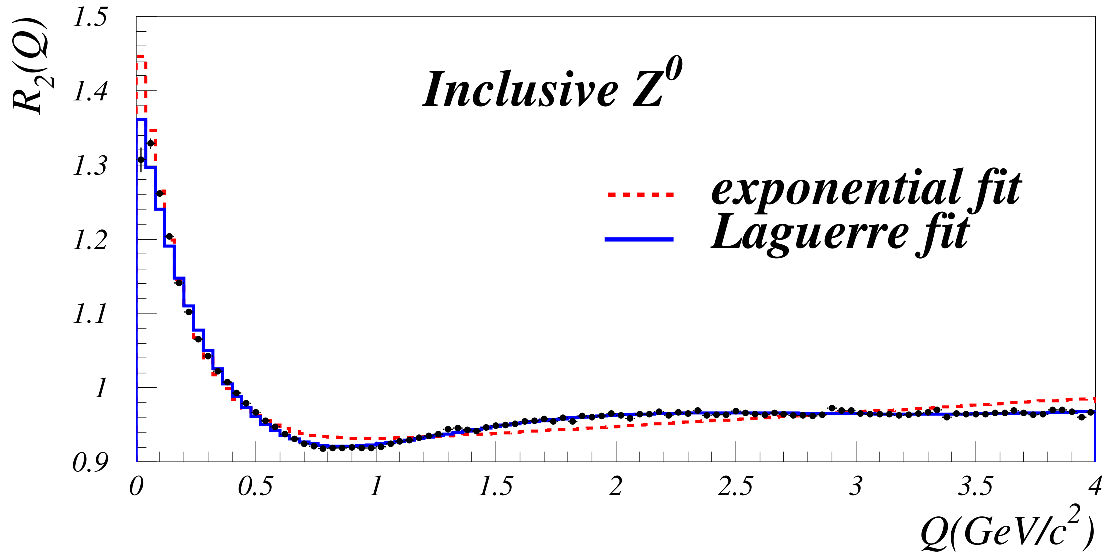

Figure 5.5: A comparison between the shape of the exponential fit of Eq. 4.22 (dashed line) and the Laguerre fit of Eq. 5.12 (solid line) to the total hadronic Z^0 sample (points).

fully-hadronic events is 10% smaller than in semi-leptonic events, while the measured R parameter is essentially the same.

Overall we conclude that the measured λ values, extracted from the $R_2(Q)$ distribution for (udsc) two- and three-jet Z^0 events are larger compared to semi-leptonic and fully-hadronic WW decays respectively. However, compairing the distributions in Fig. 5.7, one notices that $R_2(Q)$ for two-jet (udsc) Z^0 decays is nearly the same as for semi-leptonic WW events. The same holds for three-jet (udsc) Z^0 decays and fully-hadronic WW events shown in Fig. 5.8, where a difference at very small Q values can be observed.

In all cases, the difference in measured λ parameters is very small between the systems consisting of a single source and a double source and smaller than what would be expected from independent sources. This leads us to the general conclusion that the Bose-Einstein correlations manifest themselves in a similar way in hadronic Z^0 decays and in hadronic WW decays, even when the decay of two strings are considered.

Parameter	N	λ	δ	R
N	1.	0.069	-0.894	0.614
λ	0.069	1.	-0.038	0.687
δ	-0.894	-0.038	1.	-0.528
R	0.614	0.687	-0.528	1.

Table 5.4: The correlation coefficients between the four free parameters of the Laguerre fit, taken from the fit to the total hadronic Z^0 sample.

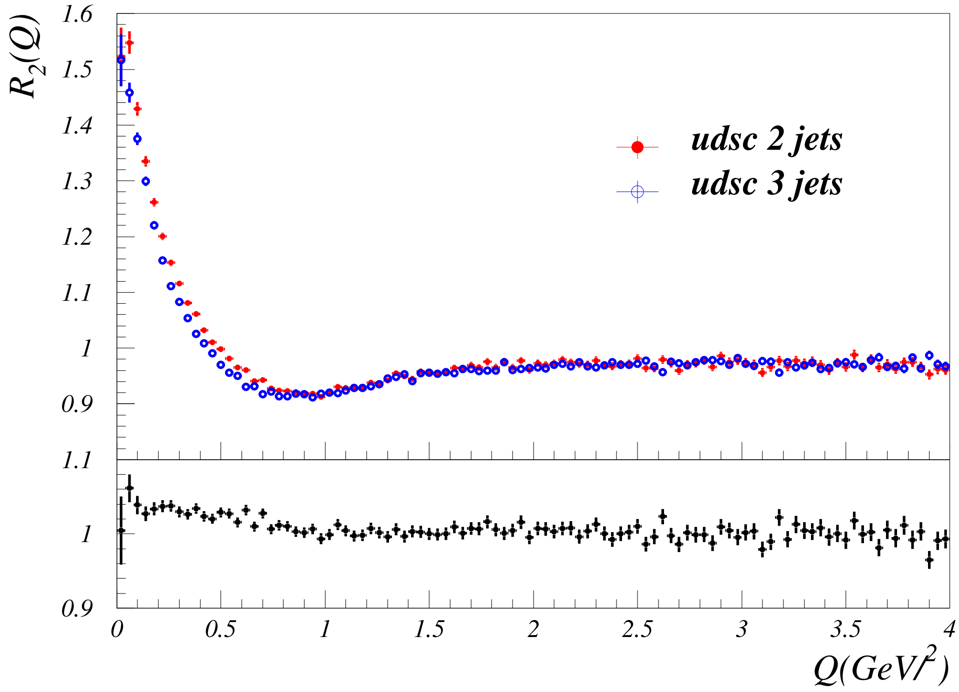

Figure 5.6: A comparison between the $R_2(Q)$ distributions for two- and three-jet (udsc) events. The $R_2(Q)$ distribution for three jet events has been re-normalised in order to have the same integral in the region 2 GeV/c^2 $< Q <$ 4 GeV/c^2.

5.4 Selection of gluon jets

In order to obtain a sample of clean gluon jets, all hadronic Z^0 events are forced into three jets using the CAMBRIDGE algorithm. It is required that the sum of the inter-jet angles is larger than 355°, thus ensuring a planar event topology. The energies of the jets are computed using massless kinematics [87], according to the following formula:

$$E_i = \sqrt{s}\frac{\sin\theta_{jk}}{\sin\theta_{12}+\sin\theta_{13}+\sin\theta_{23}}, \tag{5.15}$$

where $\sqrt{s}$ is the total centre of mass energy and θ_{ij} the angle between jets i and j, after projection into the plane perpendicular to the smallest sphericity eigenvector. The jets are subsequently ordered according to their computed energy, jet 1 being the highest energetic jet. The jet angles $\theta_1, \theta_2, \theta_3$ in the energy ordered configuration are shown in Fig. 5.9. From the pre-selected three-jet events, different topologies can be identified, see Fig. 5.9:

- twofold symmetric events, **Y-events**,
  $\theta_{2,3} \in [150° - 15°, 150° + 15°]$
- threefold symmetric events, **Mercedes events**,
  $\theta_{2,3} \in [120° - 15°, 120° + 15°]$

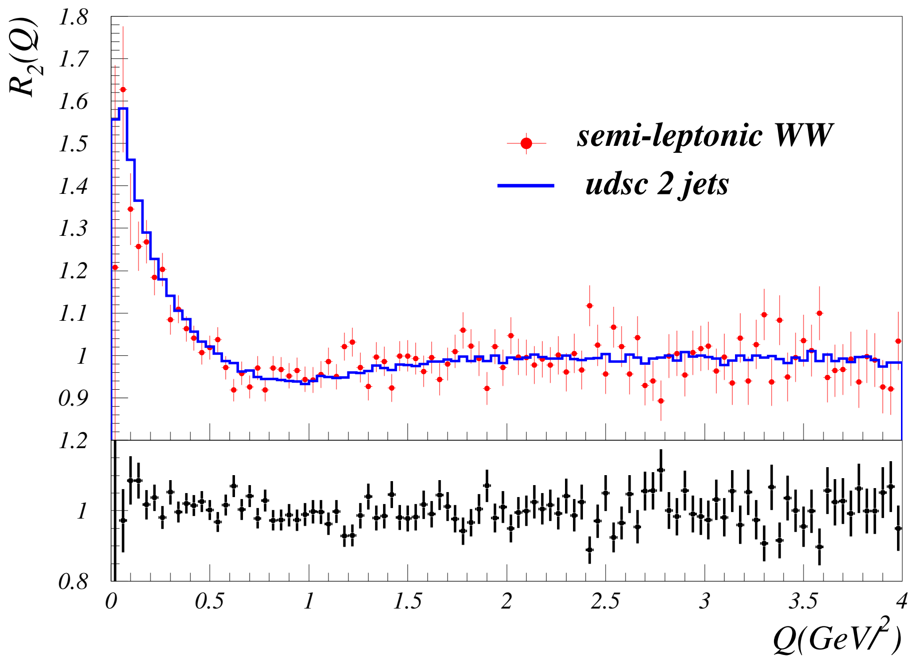

Figure 5.7: A comparison between the $R_2(Q)$ distributions for two-jet (udsc) events and semi-leptonic WW events (top). The $R_2(Q)$ distribution for two jet events has been re-normalised in order to have the same integral in the region 2 GeV/c^2 $< Q <$ 4 GeV/c^2. In addition, the ratio $R_2(2jets)/R_2(semi-leptonicWW)$ is given (bottom).

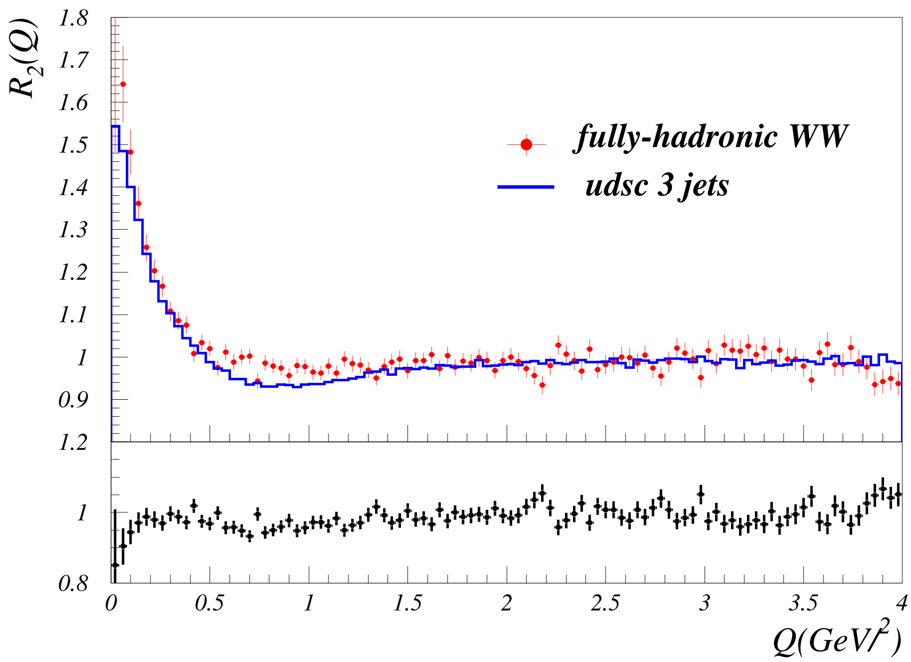

Figure 5.8: A comparison between the $R_2(Q)$ distributions for three-jet (udsc) events and fully-hadronic WW events (top). The $R_2(Q)$ distribution for three jet events has been re-normalised in order to have the same integral in the region 2 GeV/c^2 $< Q <$ 4 GeV/c^2. In addition, the ratio $R_2(3jets)/R_2(fully-hadronicWW)$ is given (bottom).

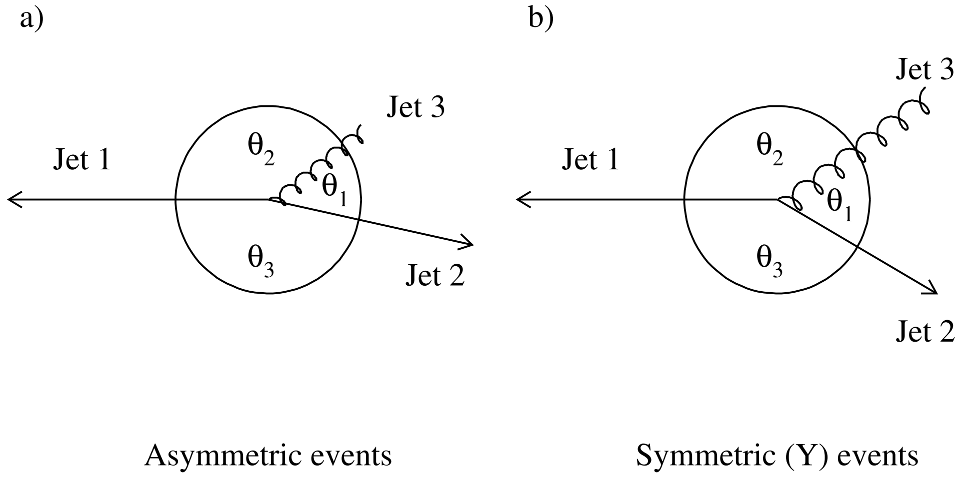

Figure 5.9: The jet configuration for asymmetric events (a) and Y-events (b).

- asymmetric three-jet events,
  $\theta_{2,3} \in [135° - 35°, 135° + 35°]$

An example of a Mercedes and Y event, seen in the DELPHI detector is shown in Fig. 5.10. For all event classes it is required that

- each of the jets has a polar angle between 30° and 150°,
- the energy of each jet is larger than 5 GeV,
- each jet contains at least two charged or neutral tracks.

Tab. 5.5 shows the data and MC statistics for the three selected event topologies.

sample	1994 data	MC no BE
Asymmetric events	86986	97934
Y-events	32915	38891
Mercedes events	8917	10327
Tagged gluons	19917	22211

Table 5.5: Size of the data and MC reference samples for the three selected event topologies

5.4.1 Gluon purity optimisation

In order so select gluon jets, a combination of event b-tagging and jet b-tagging will be applied. The jet corresponding to the gluon will be identified if the other two jets have a high probability to originate from a b-quark. It is clear that this probability will depend both on

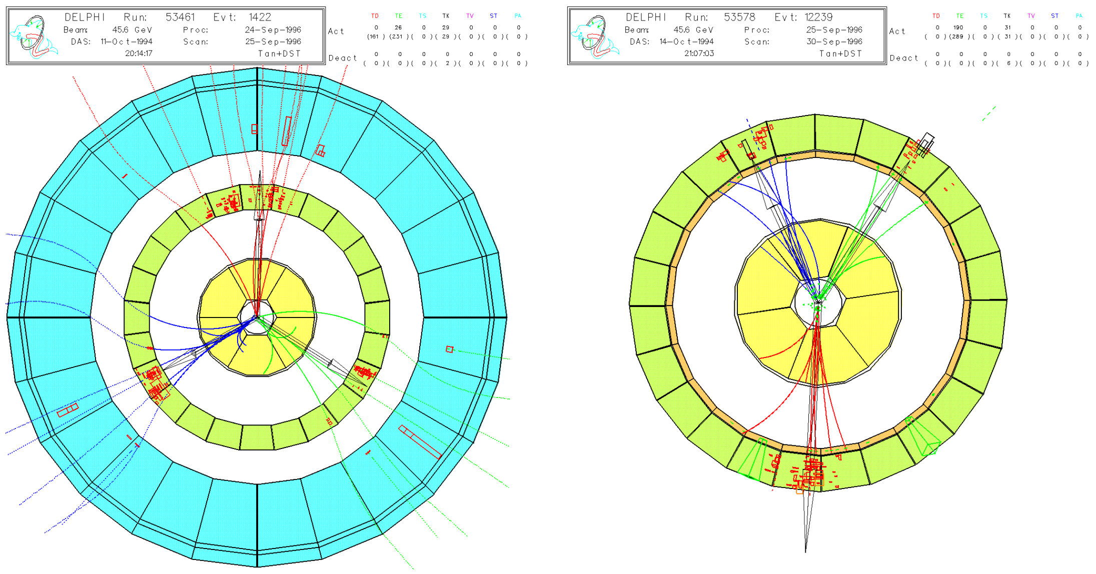

Figure 5.10: Two reconstructed three-jet events, recorded by the DELPHI detector. The picture on the left shows a Mercedes event topology, where the three inter-jet angles are all about equal to 120°. The picture on the right shows a typical Y event.

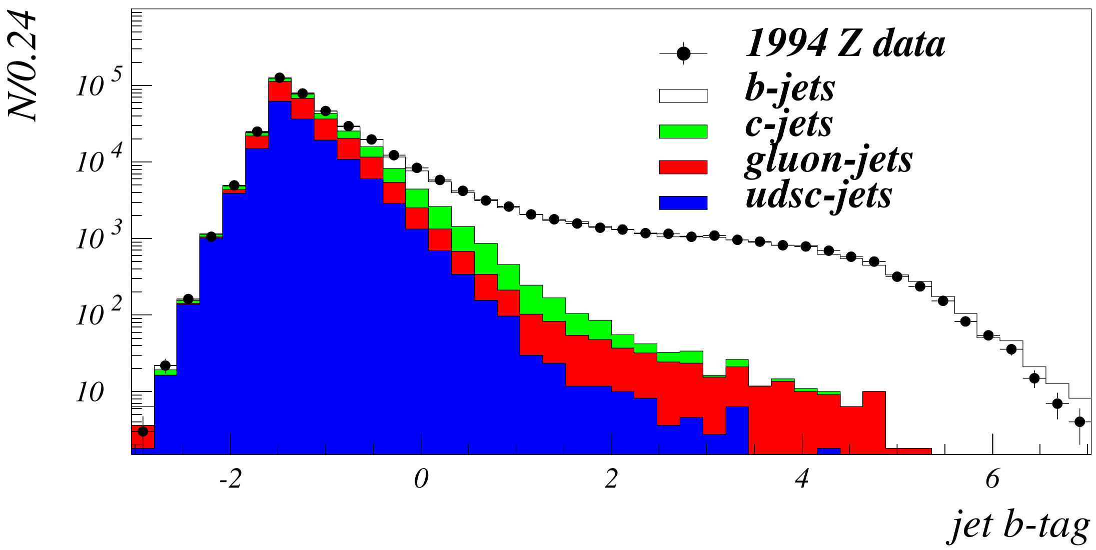

Figure 5.11: A data/Monte Carlo comparison for the combined jet b-tag variable for all hadronic three-jet events. The decomposition into light quark jets and gluons is shown by the shaded histograms.

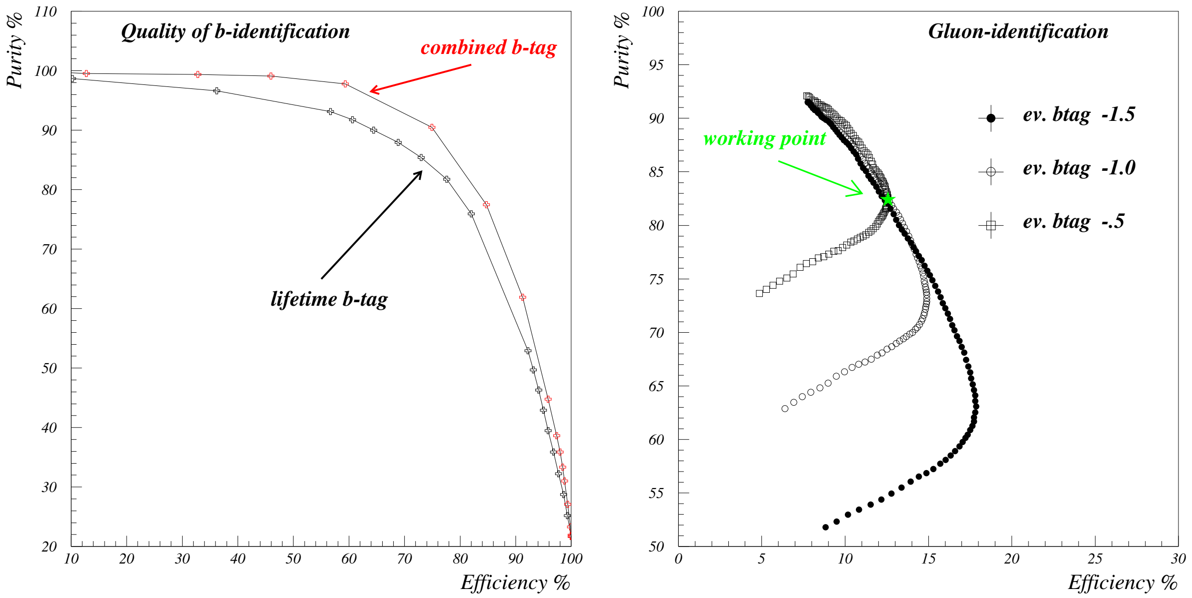

Figure 5.12: (left) The efficiency versus the purity for the selection of events containing b-quarks. The better performance of the combined b-tag w.r.t. the lifetime b-tag can be clearly seen. (right) The performance of the gluon identification. The three curves correspond to different event b-tag cuts, the points along each curve correspond to different jet b-tag cuts..

the event and on the jet b-tag. A data/Monte Carlo comparison for the combined jet b-tag variable is given in Fig. 5.11. In a first stage, events with a high b-quark content are selected from the total three-jet sample. This is done by cutting on the combined event b-tag variable. The efficiency and purity of the heavy flavor selection is shown in Fig. 5.12. After fixing the event b-tag cut, the gluon jets are selected by tagging the two other jets as b-jets. For Y-events the most energetic jet (jet1) is in 98% of the cases a quark jet. The gluon jet is then selected from the remaining two jets in the following way

- $\lambda_2 \geqslant \lambda_{cut}$ AND $\lambda_3 < \lambda_{cut} \Rightarrow$ Jet 3 is the Gluon jet,
- $\lambda_3 \geqslant \lambda_{cut}$ AND $\lambda_2 < \lambda_{cut} \Rightarrow$ Jet 2 is the Gluon jet,

For Mercedes and asymmetric event, jet 1 can not be excluded a priori from being a gluon jet, therefore the gluon jet is tagged as follows

- $\lambda_2 \geqslant \lambda_{cut}$ AND $\lambda_3 \geqslant \lambda_{cut}$ AND $\lambda_1 < \lambda_{cut} \Rightarrow$ Jet 1 is the Gluon jet,
- $\lambda_1 \geqslant \lambda_{cut}$ AND $\lambda_3 \geqslant \lambda_{cut}$ AND $\lambda_2 < \lambda_{cut} \Rightarrow$ Jet 2 is the Gluon jet,
- $\lambda_1 \geqslant \lambda_{cut}$ AND $\lambda_2 \geqslant \lambda_{cut}$ AND $\lambda_3 < \lambda_{cut} \Rightarrow$ Jet 3 is the Gluon jet,

The performance of the gluon identification is shown in Fig. 5.12. The efficiency of selected gluons is not a monotonously increasing function. When the jet-btag cut is high, then all gluon events are selected, but the amount of selected b jets is low. When the cut is low, then all b-quark jets are selected but also a large amount of gluon jets are selected. The working point is chosen at the maximum efficiency point. This maximum is moved along the purity axis to higher purities when the event b-tag is increased. The chosen working point for the gluon selection corresponds to an event btag cut of -0.5 and a jet b-tag cut $\lambda_{cut} = -0.885$. This corresponds to a gluon identification efficiency of 12.6% and a purity of 82.4%.

5.5 Bose-Einstein correlations in quark and gluon jets

Having an enriched sample of gluon jets and a sample of light quark jets, taken from two-jet Z^0 decays, a direct comparison of $R_2(Q)$ between quark and gluon jets is possible. The $R_2(Q)$ distribution for like-sign particle pairs in gluon and quark jets is shown in Fig. 5.13, both for data and a Monte Carlo sample, including BEC between all identical bosons, using the BE_{32} model with PARJ(92)=0.9 and PARJ(93)=0.60 fm. From this figure one can observe strong correlations, both in data and in Monte Carlo, but the large slope in the Q range above 1 GeV/c^2, seen in the data, is not well reproduced by the Monte Carlo Model. The same comparison is shown for quark jets in Fig. 5.14. There, good agreement in shape between data and the BE_{32} model is found.

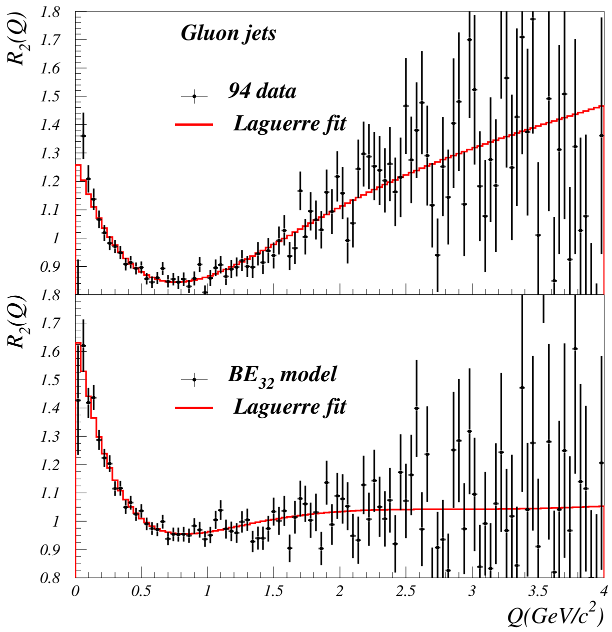

Figure 5.13: The fitted $R_2(Q)$ distribution for like-sign particles inside a gluon jet, for data (top) and a Monte Carlo sample, including BEC, using the BE_{32} model.

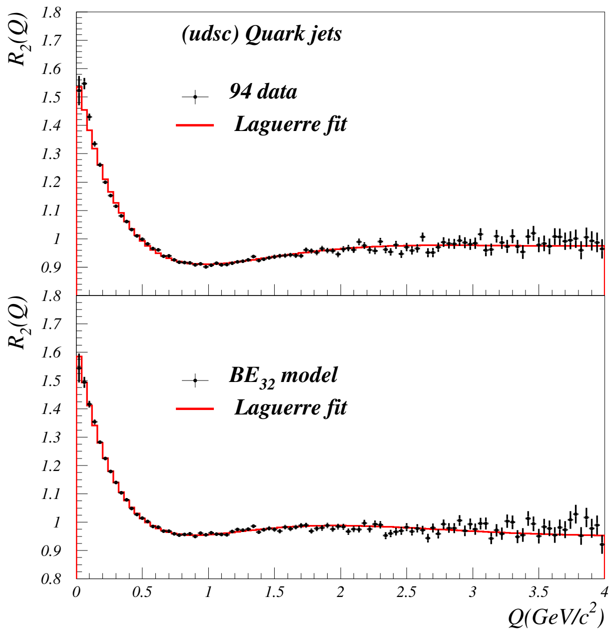

Figure 5.14: The fitted $R_2(Q)$ distribution for like-sign particles inside a light quark jet, for data (top) and a Monte Carlo sample, including BEC, using the BE_{32} model.

It was investigated whether the slope observed in the $R_2(Q)$ distribution for gluon jets in the data can be attributed to any discrepancy in single particle spectra or charge multiplicity difference between the data and the Monte Carlo reference sample. The comparison between data and reference sample for the single particle spectra can be seen in Fig. 5.15. For the majority of the charged particles a good agreement is found in all distributions, except in the large p_t tail. The charge multiplicity in gluon jets is also compared with the Monte Carlo reference sample. This distribution has a mean and RMS of 6.52 and 3.18 in data and 6.60 and 3.01 in Monte Carlo, respectively. The comparison is shown in Fig. 5.16.

Both the data-Monte Carlo comparisons of the charge multiplicity and the single particle spectra do not indicate serious discrepancies between the data and its reference sample. Therefore, the structure seen in the $R_2(Q)$ distribution of gluon jets can not be assigned to a trivial discrepancy between the data and the reference sample.

The $R_2(Q)$ distribution for like-sign particles in gluon jets and quark jets is fitted with the Laguerre expansion from Eq. 5.12, keeping the α and β parameters fixed to 1.120 and 0.597. For comparison, the same fits are performed on $R_2(Q)$ distribution for the BE_{32} model as well. The results of the fits are summarized in Tab. 5.6. From this table it can be deduced that the λ value for gluon jets is large, but that in addition a very large slope, δ is measured, of which the origin is not known. It is clear that it does not arise from Bose-Einstein correlations, since it occurs over a very large range of large Q values. Nevertheless, a large λ is also oberved in Monte Carlo events where BEC are included and where a smaller slope δ is measured. The measured λ values in quark jets are somewhat smaller than in gluon

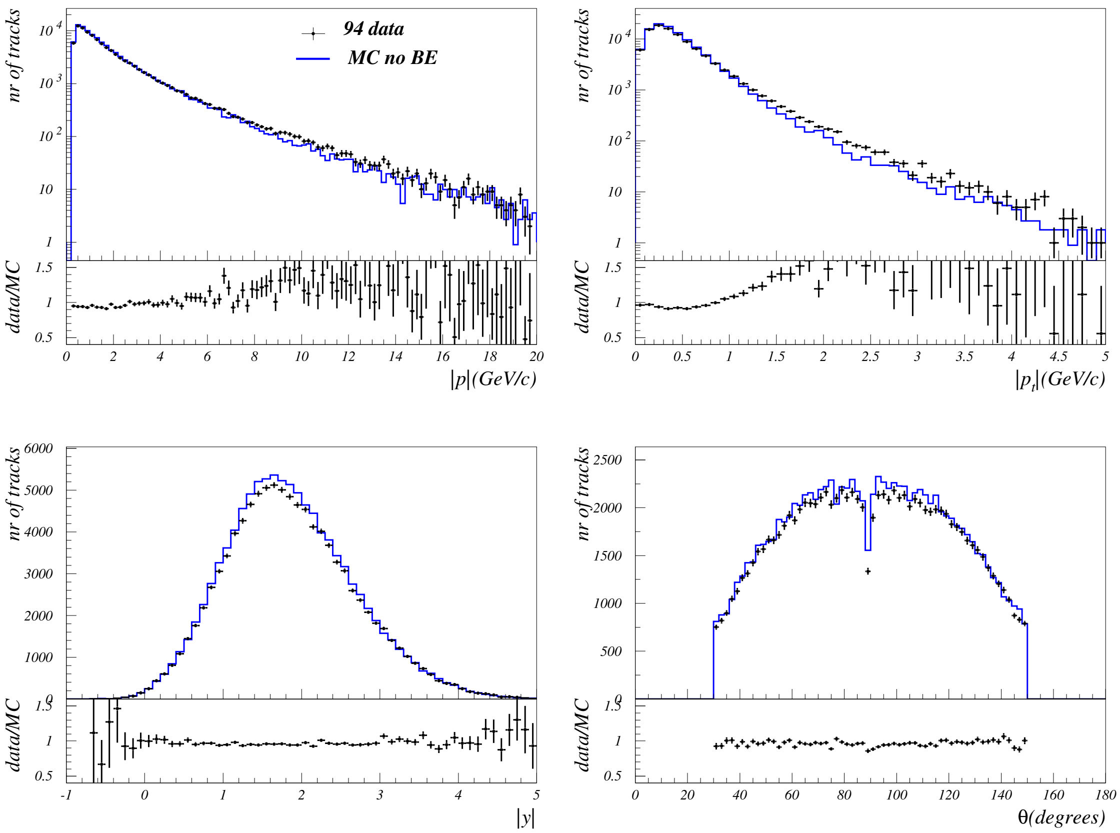

Figure 5.15: A comparison between data and the Monte Carlo reference sample without BEC of single particle spectra for charged particles, assigned to the tagged gluon jet. The plots show respectively the particle momentum, $|p|$, the transverse momentum w.r.t the gluon jet direction, $|p_t|$, the rapidity w.r.t. the gluon jet direction, y, and the polar angle w.r.t. the z axis, θ. Below each figure, the ratio between the data and Monte Carlo distributions is shown.

Parameter/Sample	N	λ	δ	R (fm)	χ^2 (96 NDF)
Gluons data	0.547 $\pm$ 0.024	1.259 $\pm$ 0.098	0.367 $\pm$ 0.038	0.239 $\pm$ 0.012	121.4
Light quarks data	0.783 $\pm$ 0.003	0.947$\pm$ 0.012	0.04 $\pm$ 0.002	0.264 $\pm$ 0.003	168.4
Gluons BE_{32}	0.809 $\pm$ 0.017	1.009 $\pm$ 0.067	0.065 $\pm$ 0.014	0.305 $\pm$ 0.016	106.4
Light quarks BE_{32}	0.851 $\pm$ 0.003	0.859 $\pm$ 0.012	0.022 $\pm$ 0.002	0.306 $\pm$ 0.003	114.1

Table 5.6: A comparison between the parameters of Eq. 5.12 from fits to the $R_2(Q)$ distributions, for like-sign particles coming from a gluon jets and quark jets. For comparison, the results for a Monte Carlo sample, including BEC, using the BE_{32} sample with PARJ(92)=0.9 and PARJ(93)=0.60 fm, are given as well.

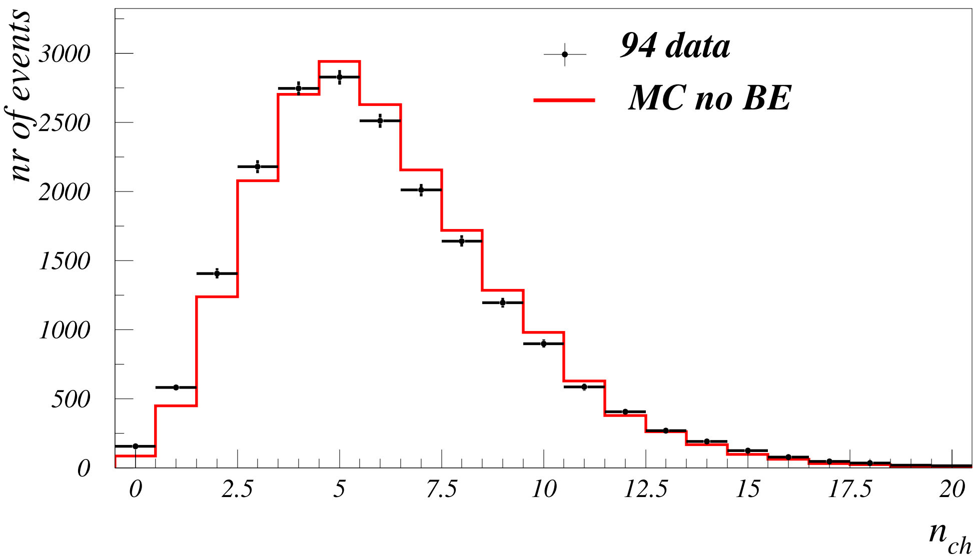

Figure 5.16: A comparison between the data and the Monte Carlo reference sample of the number of charged particles in gluon jets.

jets, both in data and Monte Carlo.

5.6 Conclusion

A semi-quantitative study of Bose-Einstein correlations in three-jet Z^0 events has been presented. According to the Lund string picture, such events consist of two hadronising strings. It was found that the Bose-Einstein correlations in three-jet events are nearly the same as in two-jet events, whereas in the case of independent fragmenting strings less correlations in three-jet events are expected. A comparison with WW decays was made, indicating that the normalised density $R_2(Q)$ in two-jet (udsc) Z^0 events is identical to that of of semi-leptonic WW events.

The $R_2(Q)$ distribution for three-jet (udsc) Z^0 events was found to be very similar to fully-hadronic WW events. This means that, from a string fragmentation point of view, there is no difference between light quark Z^0 decays and hadronic WW decays, even in the case where more than one string fragments.

A first attempt to study Bose-Einstein correlations in a highly enriched gluon jet sample was presented. It was found that the λ values inside gluon jets are very large and larger than in quark jets. However, a very large slope in the tail of the normalised density $R_2(Q)$ for like-sign particle pairs in gluon jets was found in the data. This slope is not reproduced by a Monte Carlo Model including BEC. This slope can not be attributed to BEC, since BEC manifests itself dominantly at low Q values. However, a first check on single particle spectra and the charge multiplicity distribution revealed no major probems in the Monte Carlo reference sample. Other effects, such as the baryon production rates in gluon jets are not verified, but could be on the origin of the slope at large Q values.

Further studies of Bose-Einstein correlations inside gluon jets are needed, including more statistics and a proper study of the systematic uncertainties. Given the large available statistics, the study of BEC in gluon jets possibly offers a promising way to investigate inter-string BEC.

Summary

For more than a decade, LEP has provided particle physicists with a treasure of data. This data allowed a precise measurement of many of the Standard Model parameters, in order to test its consistency and to hunt for the undiscovered Higgs boson. In comparison, little is known about the confinement of quarks inside hadrons. Theoretical calculations in the non-perturbative regime of QCD have proven to be cumbersome and most of the time one has to rely on phenomenological models, which nature is often semi-classical. It is however clear that quantum-mechanics is the proper framework to understand the binding of quarks inside hadrons. The Bose-Einstein effect is a clear and undeniable part of this theory, complicating the statistical description of multi-hadron final states. It states that the wave function, describing a system of identical bosons (particles with integer spin) should be symmetric under permutation of these particles. As a consequence the four-momentum differences between identical bosons in a multi-hadron final state will be smaller than in a world where Bose-Einstein statistics would not apply.

The main question, however, is whether bosons obey this principle if they originate from two different sources, even if the distance between these sources is known to be a factor ten smaller than the distance needed to produce a boson. The hadronic decay of two pair-produced W bosons in the reaction $e^+e^- \to W^+W^-$ provides us with a laboratory to study this question.

If correlations between identical bosons coming from different W's can be attributed to the Bose-Einstein effect, a physical correct implementation in the current hadronisation models will not be straightforward.

In addition, it will add a systematic uncertainty in the precise determination of the mass of the W boson in the fully-hadronic decay channel, since it assumes the two produced W's to decay independently.

In this thesis, the two-particle correlations in the hadronic final states of the reaction $e^+e^- \to W^+W^-$ are extensively studied. These processes, recorded by the DELPHI detector, being one of the four LEP experiments, are separated from a range of other reactions. This is done at several centre-of-mass energies, ranging from 189-209 GeV. Nearly 6000 hadronic WW decays were selected from the total data sample, 55% of which are found to be candidates of the process $e^+e^- \to W^+W^- \to q_1\bar{q}_2q_3\bar{q}_4$, where inter-$W$ Bose-Einstein correlations can take place. The inter-W BEC effect is isolated, using the remaining subset of WW events corresponding to the reaction $e^+e^- \to W^+W^- \to q_1\bar{q}_2l\bar{\nu}_l$. These events are mixed and used as a reference sample where no inter-W BEC can exist.

Using this technique, an indication of inter-W BEC was found. So far, none of the other LEP experiments have reported a similar observation. In order to quantify our result, a quantity Λ, being zero in the absence of inter-W BEC, was extracted from the two particle densities measured from the data. The measured value of this parameter amounts to

$$\Lambda = 0.241 \pm 0.075 \pm 0.038,$$

where the first error is statistical and the second systematic.

Using our measured result, a systematic shift in the measured W mass in the fully-hadronic decay channel, using the DELPHI mass reconstruction method, is deduced. It was found that at 68% confidence level a mass shift of 36.1 MeV/c^2 can not be excluded. This uncertainty will be further reduced if no other LEP experiment finds an indication for inter-W BEC and if the mass information obtained from semi-leptonic decays is added.

In addition to WW decays, three-jet Z^0 decays, produced during the LEP1 period at centre-of-mass energies around 91.2 GeV, can be identified as two hadronizing sources. The three-jet topologies correspond to the reaction $e^+e^- \rightarrow Z^0 \rightarrow q\bar{q}g$, where one of the two quarks radiates a hard gluon.

A semi-quantitative study of this system is made of, in particular, the correlations between particles originating from the gluon. It is found that, concerning two-particle BEC, the hadronic decays of a Z^0 are very similar to hadronic WW decays, provided that only light quark decays are considered.

The correlations inside three-jet Z^0 decays are nearly as strong as those measured in two jet decays, confirming the presence of BEC between two hadronizing sources. Moreover, strong correlations are observed inside gluon jets. The nature of these correlations and the shape of the normalised density distribution in this system needs to be further investigated in order to obtain further insights on the true nature of Bose-Einstein correlations in two hadronizing systems.

Samenvatting

Gedurende meer dan tien jaar verzamelden elementaire deeltjesfysici bij de LEP versneller in Genève een weelde aan gegevens. Deze lieten een precieze meting toe van de meeste parameters van het Standaard Model, met als doel het testen van haar consistentie en de zoektocht naar het Higgs boson. In vergelijking is er weinig bekend over de manier waarop quarks zich binden in hadronen. Theoretische berekeningen in het niet-perturbatieve QCD regime verlopen doorgaans moeizaam en in vele gevallen moet men terugvallen op fenomenologische modellen die vaak semi-klassiek zijn. Het is daarentegen duidelijk dat de kwantummechanica de aangewezen theorie is om de opbouw van hadronen uit quarks te beschrijven. Het Bose-Einstein effect is een niet ontkenbaar onderdeel van deze theorie die de statistische beschrijving van multi-hadron eindtoestanden bemoeilijkt. Het postuleert dat de golffunctie die een systeem van identieke bosonen (deeltjes met heeltallige spin) beschrijft symmetrisch moet zijn onder permutaties van deze deeltjes. Een gevolg hiervan is dat het verschil in vier-impuls tussen identieke bosonen in een multi-hadron eindtoestand kleiner is dan in een wereld zonder Bose-Einstein statistiek.

Daarenboven is het belangrijk te weten of bosonen die van een verschillende productiebron afkomstig zijn aan ditzelfde principe onderworpen zijn, in het bijzonder wanneer de afstand tussen deze bronnen een factor tien kleiner is dan de benodigde afstand om een boson te produceren. Het hadronische verval van twee als paar geproduceerde W bosonen in de reactie $e^+e^- \to W^+W^-$ laat ons toe deze vraag te bestuderen.

Als correlaties tussen identieke bosonen, afkomstig van verschillende W's éénduidig aan het Bose-Einstein effect kunnen worden toegewezen, dan zal dit een correcte implementatie van het hadronisatie-proces in vele modellen bemoeilijken. Bovendien zal het een systematische onzekerheid introduceren in de precieze meting van de massa van het W boson in het volledig hadronische vervalkanaal, waar een onafhankelijk W verval wordt verondersteld.

In deze thesis worden correlaties tussen twee deeltjes in de hadronische eindtoestand van de reactie $e^+e^- \to W^+W^-$ uitgebreid bestudeerd. Deze processen die door de DELPHI detector, één van de vier LEP experimenten, werden geregistreerd, moeten worden gescheiden van andere reacties. Dit is gedaan bij verschillende massamiddelpuntsenergieën, gaande van 189 tot 209 GeV. Bijna 6000 hadronische WW vervallen werden geselecteerd uit het totale staal van gegevens, waarvan 55% kandidaten zijn voor de reactie $e^+e^- \to W^+W^- \to q_1\bar{q}_2q_3\bar{q}_4$, waarbij inter-$W$ Bose-Einstein Correlaties (BEC) zich kunnen manifesteren. Het inter-W BEC effect werd geïsoleerd gebruik makende van de overige reacties van het type $e^+e^- \to W^+W^- \to q_1\bar{q}_2l\bar{\nu}_l$. Deze gebeurtenissen worden "gemengd" en gebruikt als een referentiestaal waarin, bij constructie, geen inter-W BEC optreden.

Met deze techniek werd een indicatie voor het bestaan van het inter-W BEC effect aangetoond. Totnogtoe heeft geen van de andere LEP experimenten eenzelfde aanwijzing gevonden. Om het resultaat te kwantificeren werd de grootheid Λ, die nul is in de afwezigheid van inter-W BEC, berekend uit de twee-deeltjesdichtheden die in de data zijn gemeten. De gemeten waarde van deze parameter bedraagt

$$\Lambda = 0.241 \pm 0.075 \pm 0.038,$$

waarbij de eerste onzekerheid statistisch en de tweede systematisch is.

Gebruik makende van dit resultaat werd de systematische afwijking in de door DELPHI gemeten W massa in het volledig hadronische vervalkanaal afgeleid. Binnen een vertrouwensinterval van 68% kan een afwijking van 36.1 MeV/c^2 niet worden uitgesloten. Deze onzekerheid zal echter worden gereduceerd indien geen andere LEP experiment een aanwijzing voor inter-W BEC vindt en indien de massa, gemeten in het semi-leptonische vervalkanaal wordt gecombineerd met die uit het volledig hadronische vervalkanaal.

Naast WW gebeurtenissen kunnen drie-jet Z^0 vervallen, geproduceerd in het LEP1 stadium bij massamiddelpuntsenergieën rond 91.2 GeV, beschouwd worden als twee hadroniserende bronnen. De drie-jet topologieën corresponderen met het proces $e^+e^- \rightarrow Z^0 \rightarrow q\bar{q}g$, waarbij één van de twee primaire quarks een hard gluon afstraalt.

Deze thesis bevat een semi-kwantitatieve studie van dit fenomeen, in het bijzonder de correlaties tussen twee deeltjes afkomstig van het gluon. Hieruit werd besloten dat, betreffende BEC tussen twee deeltjes, het hadronische Z^0 verval zeer gelijkend is met hadronische WW verval indien alleen het verval naar lichte quarks wordt beschouwd.

De correlaties in drie-jet Z^0 vervallen zijn bijna even sterk als die gemeten in twee-jet vervallen, hetgeen een bevestiging is voor het bestaan van BEC tussen twee hadroniserende bronnen.

Bovendien zijn sterke correlaties gemeten tussen deeltjes afkomstig uit gluon jets. De oorsprong van deze correlaties en de vorm van de genormaliseerde twee-deeltjes dichtheidsverdeling dient verder te worden onderzocht. Hiermee zal verder inzicht worden verworven in de ware oorsprong van Bose-Einstein correlaties in twee hadroniserende systemen.

Dankwoord

Een proefschrift komt nooit tot stand zonder de steun en samenwerking van anderen. Dit is zeker het geval wanneer men in een grote internationale collaboratie samenwerkt. Daarom is dit de aangewezen plaats om een aantal mensen te bedanken. Als eersten wil ik mijn promotor en co-promotor bedanken. Frans Verbeure ben ik erkentelijk omdat ik de kans kreeg in zijn groep te doctoreren. Zijn inspanningen om mij gedurende de eerste jaren van mijn doctoraat op CERN te laten verblijven stel ik zeer op prijs. Bovendien bewonder ik zijn objectiviteit en neutraliteit tijdens de vaak hoog oplopende discussies binnen de Bose-Einstein werkgroep in DELPHI. Eddi De Wolf wil ik bedanken voor de vele discussies over het meten van Bose-Einstein correlaties en alles wat ermee gepaard gaat. Vooral bij het proeflezen van mijn thesis was je een grote steun. Sorry dat ik je op sommige momenten hoofdpijn bezorgde.

For introducing me to the physics analysis in DELPHI I would like to thank Alessandro De Angelis, and in particular Sarka Todorova. Although she sometimes gave me sleepless nights, I am anyway thankful for her practical and moral support. Niels Kjaer deserves a special mention as well for teaching me the gory details of statistics.

Mijn eerste contact met elementair deeltjes onderzoek deed ik op aan de Universiteit Utrecht, waar ik Prof. René Kamermans en Peter Van De Ven als zeer sympathieke begeleiders ervaarde.

Gedurende mijn lange verblijf op CERN leerde ik een boel leuke mensen kennen. Vooral aan de “uitstapjes” met Eelco Schillings, Ivo van Vulpen, Martijn Mulders en Martin Blom heb ik mooie herinneringen. The Liverpool crew with Uli Parzefall as front-man was a pleasure to hang out with as well.

Daarnaast waren er natuurlijk mijn twee DELPHI “amigos”, Thomas Alderweireld en Jorgen D’ Hondt. Wat kan ik meer zeggen dan dat ik me geen fijner kamergenootjes kon voorstellen dan jullie twee.

De collega’s binnen de UIA groep elementaire deeltjes draag ik ook allemaal een warm hart toe. Tinne Anthonis, Filip Moortgat, Pierre Van Mechelen en Tom Beckers bedank ik voor hun tolerantie en geduld die vaak op de proef werden gesteld door mijn energieke gedrag.

Tenslotte wil ik mijn ouders en mijn vriendin Katja bedanken voor hun interesse en steun bij het maken van mijn doctoraat. Katja, bedankt voor je geduld en begrip, vooral in de laatste maanden tijdens het afwerken van mijn thesis.

Appendix A

Errors and biases on fits

In this appendix it will be illustrated how one can be trapped by using standard statistical textbook methods when it comes to the calculation of a statistical estimator and its variance. When the ratio of two numbers is calculated, assuming Poisson statistics, the variance on their ratio correlates strongly with the expectation value of the ratio itself. When several of these ratios are fitted, the expectation values of the fit parameters are always biased towards smaller values. This can be drastically enhanced when the expectation values of these ratios are mutually correlated.

Let us first consider the ratio of two numbers X and Y. The variance on this number is given by standard error propagation:

$$\sigma^2(\frac{X}{Y}) = \frac{dX^2}{Y^2} + \frac{X^2 dY^2}{Y^4}. \tag{A.1}$$

Let us assume that X and Y are Poisson distributed variables: in this case $dX^2 = X$ and $dY^2 = Y$. The variance of the ratio becomes

$$\sigma^2(\frac{X}{Y}) = \frac{X^2}{Y^2} \cdot (\frac{1}{X} + \frac{1}{Y}). \tag{A.2}$$

Now we introduce a small perturbation δ to X and Y and assume for simplicity that $Y = X$. When X and Y are unperturbed, the ratio becomes 1 and the variance equals $2/X$.. Let us perturb both X and Y so that the ratio becomes

$$\begin{aligned}
R = \frac{X+\delta}{X+\delta} &\rightarrow \sigma^2(R) = \frac{2}{X}(1 - \frac{\delta}{X}); \\
R = \frac{X-\delta}{X-\delta} &\rightarrow \sigma^2(R) = \frac{2}{X}(1 + \frac{\delta}{X}); \\
R = \frac{X+\delta}{X-\delta} &\rightarrow \sigma^2(R) = \frac{2}{X}(1 + \frac{4\delta}{X}); \\
R = \frac{X-\delta}{X+\delta} &\rightarrow \sigma^2(R) = \frac{2}{X}(1 - \frac{4\delta}{X}).
\end{aligned} \tag{A.3}$$

The previous exercise indicate that the variance is positively correlated with the result of the ratio. If one would fit this ratio for N measurements, the measurements with a large expectation value will get a larger variance than the measurements with a small expectation value. Due to the fact that, in a least χ^2 method, where each measurement is weighted with the inverse of its variance

$$\chi^2 = \sum_i \frac{(f_i - R_i)^2}{\sigma^2(R_i)}, \tag{A.4}$$

the measurement will be biased towards smaller values. An alternative to avoid this problem would be to define the χ^2 as follows

$$\chi^2 = \sum_i \frac{(f_i - R_i)^2}{f_i}. \tag{A.5}$$

This approach is well known, but not always useful, since it makes the χ^2 minimisation less linear. A more pragmatic solution is to consider the natural logarithm of the observable X/Y. When the same perturbation δ is applied one gets

$$\begin{aligned}
\ln(R) = \ln(\frac{X+\delta}{X+\delta}) &\rightarrow \sigma^2(\ln(R)) = \frac{2}{X}(1-\frac{\delta}{X}); \\
\ln(R) = \ln(\frac{X-\delta}{X-\delta}) &\rightarrow \sigma^2(\ln(R)) = \frac{2}{X}(1+\frac{\delta}{X}); \\
\ln(R) = \ln(\frac{X+\delta}{X-\delta}) &\rightarrow \sigma^2(\ln(R)) = \frac{2}{X}; \\
\ln(R) = \ln(\frac{X-\delta}{X+\delta}) &\rightarrow \sigma^2(\ln(R)) = \frac{2}{X}.
\end{aligned} \tag{A.6}$$

It can be deduced from the example above that, a least χ^2 fit to determine a set of parameters biases the result of a fit towards lower values in the case where measurements above the true value have larger errors than measurements below the true value.

In what follows it will be demonstrated how 2 measurements of the same physical quantity with a common normalisation error can lead to a biased estimator of the physical value when a χ^2 fit is used. The example is adopted from [93]. Although it is not general enough to describe the situation one is dealing with in fitting the $D(Q)$ measurement of BEC between different W's, it is very illustrative and easy to understand. Let us consider the case of two uncorrelated measurements x_1 and x_2 with variances σ_1^2 and σ_2^2 of a physical quantity $\hat{x}$. We will fit these 2 values with a constant k using a least squares fit, i.e the following equation should be solved

$$\frac{\partial\chi^2}{\partial k} = \frac{1}{D}\left[(x_1 - k)^2\sigma_2^2 + (x_2 - k)^2\sigma_1^2\right] = 0, \tag{A.7}$$

where D stands for the determinant of the covariance matrix V of the points x_1 and x_2, which is in this case $\sigma_1^2 \cdot \sigma_2^2$. Solving Eq. A.7 results in an expectation value for k

$$\hat{k} = \frac{x_1 \cdot \sigma_2^2 + x_2 \cdot \sigma_1^2}{\sigma_1^2 + \sigma_2^2}. \tag{A.8}$$

Let us assume the case where x_1 and x_2 are calibrated by means of a multiplicative factor f with an associated uncertainty σ_f. Let us for simplicity assume further that the most probable value of f is 1. The corrected results now take the form of $y_i = f \cdot x_i$. The covariance matrix of the corrected results is given by the transformation:

$$V_{Y_{kl}} = \sum_{ij} \frac{\partial y_k}{\partial x_i} \frac{\partial y_l}{\partial x_j} V_{X_{ij}}, \tag{A.9}$$

where the result looks like

$$V_Y = \begin{pmatrix} \sigma_1^2 + \sigma_f^2 \cdot x_1^2 & \sigma_f^2 \cdot x_1 \cdot x_2 \\ \sigma_f^2 \cdot x_1 \cdot x_2 & \sigma_1^2 + \sigma_f^2 \cdot x_1^2 \end{pmatrix}. \tag{A.10}$$

A fit using this covariance matrix results now in the minimisation of

$$\begin{aligned} \chi^2 = \frac{1}{D}[(x_1 - k)^2 \cdot (\sigma_2^2 + x_2^2 \cdot \sigma_f^2) + (x_2 - k)^2 \cdot (\sigma_1^2 + x_1^2 \cdot \sigma_f^2) \\ - 2 \cdot (x_1 - k) \cdot (x_2 - k) \cdot x_1 \cdot x_2 \cdot \sigma_f^2], \end{aligned} \tag{A.11}$$

which gives as a result for the estimator of k

$$\hat{k} = \frac{x_1 \cdot \sigma_2^2 + x_2 \cdot \sigma_1^2}{\sigma_1^2 + \sigma_2^2 + (x_1 - x_2)^2 \cdot \sigma_f^2}. \tag{A.12}$$

Taking the ratio between $\hat{k}$ and $\bar{x}$, the average weighted with the inverse of the variances, as in the case of uncorrelated measurements

$$r = \frac{\hat{k}}{\bar{x}} = \frac{1}{1 + \frac{(x_1 - x_2)^2}{\sigma_1^2 + \sigma_2^2} \cdot \sigma_f^2}, \tag{A.13}$$

one notes that $\hat{k}$ is always smaller than the simple average value $\bar{x}$, with a dependence on the difference between the two measurements x_i and the normalisation error σ_f.

Appendix B

Details of the WW event selections

B.1 Selection of fully-hadronic events

Fully hadronic events are essentially characterized by a large visible energy and a topology of four or more energetic jets.

A feed-forward neural network is used to select this category of events after some basic pre-cuts. The network is based on the JETNET package [94], uses the standard back-propagation algorithm, and consists of three layers with 13 input nodes, 7 hidden nodes and one output node. The neural network is the same used in the DELPHI standard cross-section analysis [73]. The following input variables are used for the network (for a full description of these variables, see [95, 52]:

1. The difference between the maximum and minimum jet energy after a 4C fit, imposing momentum and energy conservation;
2. the effective center of mass energy $\sqrt{\mathrm{s}'}$;
3. the value of Y_{34} from the DURHAM [70] clustering algorithm;
4. the minimum angle between two jets after the 4C fit, θ_{min};
5. the sphericity [1], S;
6. the thrust value [2], T;
7. the minimum jet broadening B_{min};
8. the minimum jet multiplicity ;

[1]The sphericity tensor is defined as $S^{\alpha\beta} = \frac{\sum_i p_i^\alpha p_i^\beta}{\sum_i |\mathbf{p_i}|}$, where $\alpha, \beta = 1, 2, 3$ corresponds to the x, y and z component. By standard diagonalisation of $S^{\alpha\beta}$ one may find three eigenvalues $\lambda_1 \geq \lambda_2 \geq \lambda_3$. The sphericity is then defined as $S = 3/2(\lambda_2 + \lambda_3)$. Sphericity is essentially a mesure of the summed transverse momentum w.r.t. the event axis.

[2]The thrust, T is defined by $T = \max \frac{\sum_i |\mathbf{n} \cdot \mathbf{p_i}|}{\sum_i |\mathbf{p_i}|}$, where $\mathbf{p_i}$ are the particles three-momenta and $\mathbf{n}$ is the three-vector with length one, over which the maximum value of T is reached. A two-jet topology corresponds to $T \approx 1$ while an isotropic event to $T \approx 1/2$.

9. the Fox-Wolfram moment H3 [96];
10. the Fox-Wolfram moment H4;
11. the goodness of fit, P_{WW}, for all jet pairings, derived from the χ^2 of a 6C fit, requiring the two di-jet systems to have the same mass, equal to the nominal W mass.
12. the total transverse energy, E_{trans};
13. the total charged energy, E_{char};

A data-Monte Carlo comparison for all input variables and the output variable is shown in Figs. B.1- B.3 for the combined data set. They are shown in the same order as they are listed above. In general, a very good agreement between data and Monte-Carlo is found for all variables.

The number of observed data events, the expectation from the MC simulation and the purities and efficiencies for several neural network output cuts are given in Table B.1 for all energies analysed in this work.

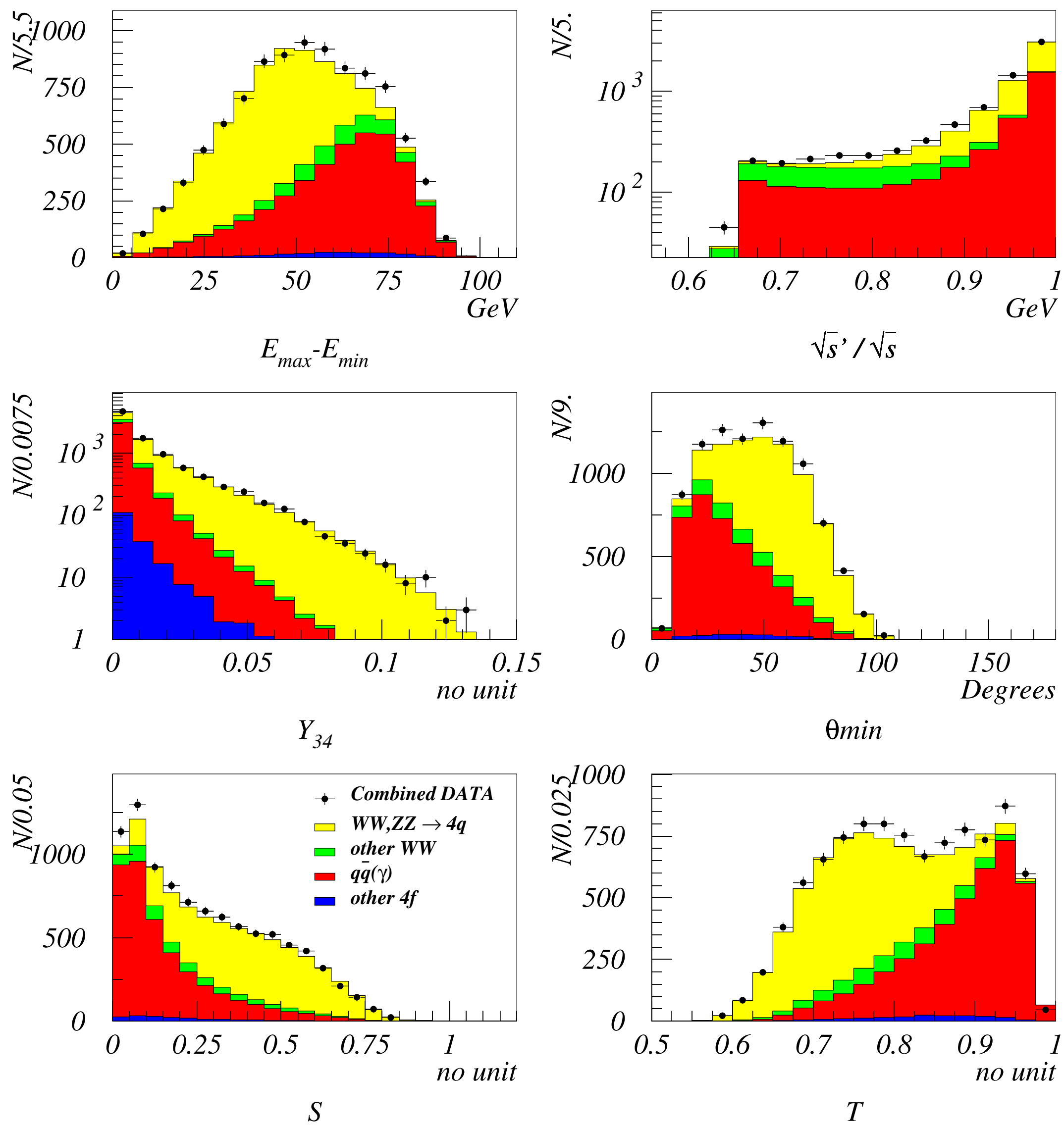

Figure B.1: Comparison of data with Monte carlo predictions for all 4q neural network input variables, after preselections.

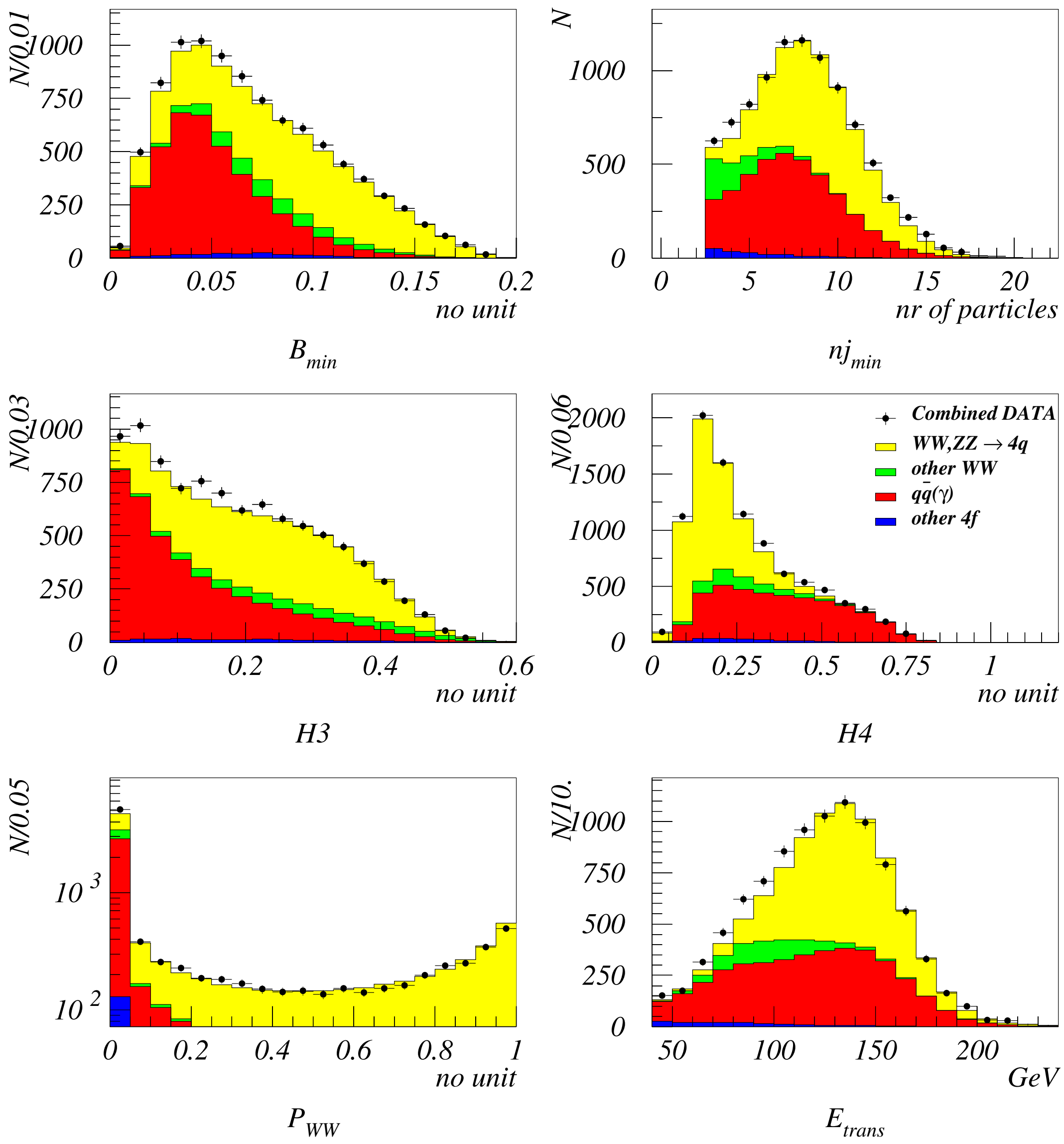

Figure B.2: Comparison for all 4q neural network input variables after preselections, continued.

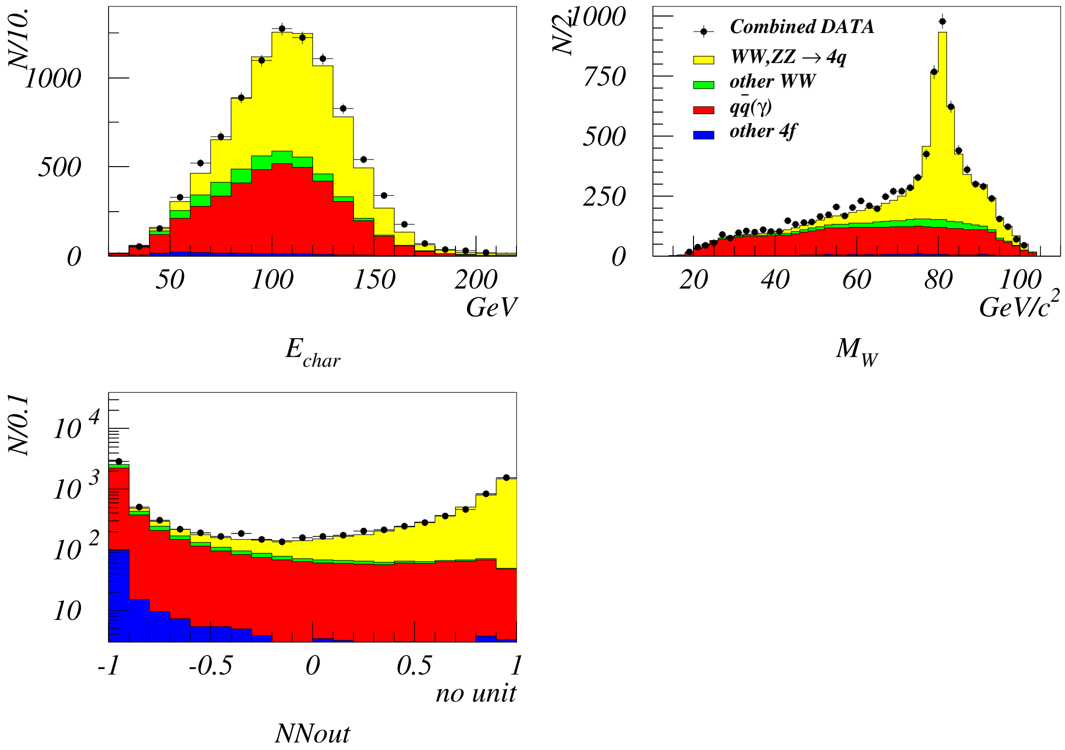

Figure B.3: Comparison for all 4q neural network input variables after preselections, continued. The last two plots show the reconstructed W mass using a 5C constrained fit and the neural network output variable, respectively.

B.2 Selection of semi-leptonic events

The decay channel $WW \to q\bar{q}l\nu$ is characterized by the presence of two or more hadronic jets, an isolated, energetic lepton or a narrow jet in the case of hadronic τ decays, and missing energy and momentum due to undetected neutrino(s). The selection procedure is adopted from [74]. All events are subjected to a first set of preselection cuts:

- more than 6 charged tracks;
- transverse energy larger than 0.25 $\sqrt{s}$;
- total energy in a cone of $30°$ around the beam pipe less than 30 GeV;
- absence of 2 isolated leptons of the same flavor;
- polar angle of the missing momentum between $10°$ and $170°$;
- the total energy of all neutral particles in the event less than 0.2 $\sqrt{s}$;
- a minimum of 4 particles of which at least 1 charged particle in each jet of the hadronic system.

After the pre-selection all events are subjected to a neural network selection, based on the MLPFIT package using a hybrid-linear BFGS method [97]. Events are passed sequentially through the muon, electron and tau selections. Each event failing a previous selection is still a candidate for the following one.

The semi-leptonic event selections, including the input parameters for the neural network, are given below. The efficiencies, purities, numbers of observed and expected events, are given in Table B.1.

1. **Muon events** After requiring the presence of a tagged muon, the following preselections were applied before subjecting the event to the neural network selection:

   - the momentum of the muon cannot be lower than $0.15\sqrt{s}$ if simultaneously the invariant mass of the lepton-neutrino system is lower than 60 $\mathrm{GeV/c^2}$;
   - the invariant mass of the $q\bar{q}$ and of the $l\nu$ system has to be bigger than 10 $\mathrm{GeV/c^2}$;
   - $p \cdot \theta_{iso} > 250°\mathrm{GeV/c}$.

   The 9 input variables to the neural network are then:

   (a) the muon momentum;
   (b) the muon isolation angle;
   (c) the missing momentum;
   (d) $|\cos(\theta_{\mathrm{miss}})|$;
   (e) the opening angle between the muon and the missing momentum direction;
   (f) the transverse energy;

(g) the total visible energy;

(h) $\sqrt{s'}/\sqrt{s}$, where $\sqrt{s'}$ is the effective center-of-mass energy;

(i) the angle between the muon and the combined di-jet momentum

The final network output is required to be bigger than 0.4. The neural network output variable for the muon selection, together with all input variables are shown in Figs. B.4 and B.5 . In general an excellent agreement between data and Monte Carlo simulation was found in all variables.

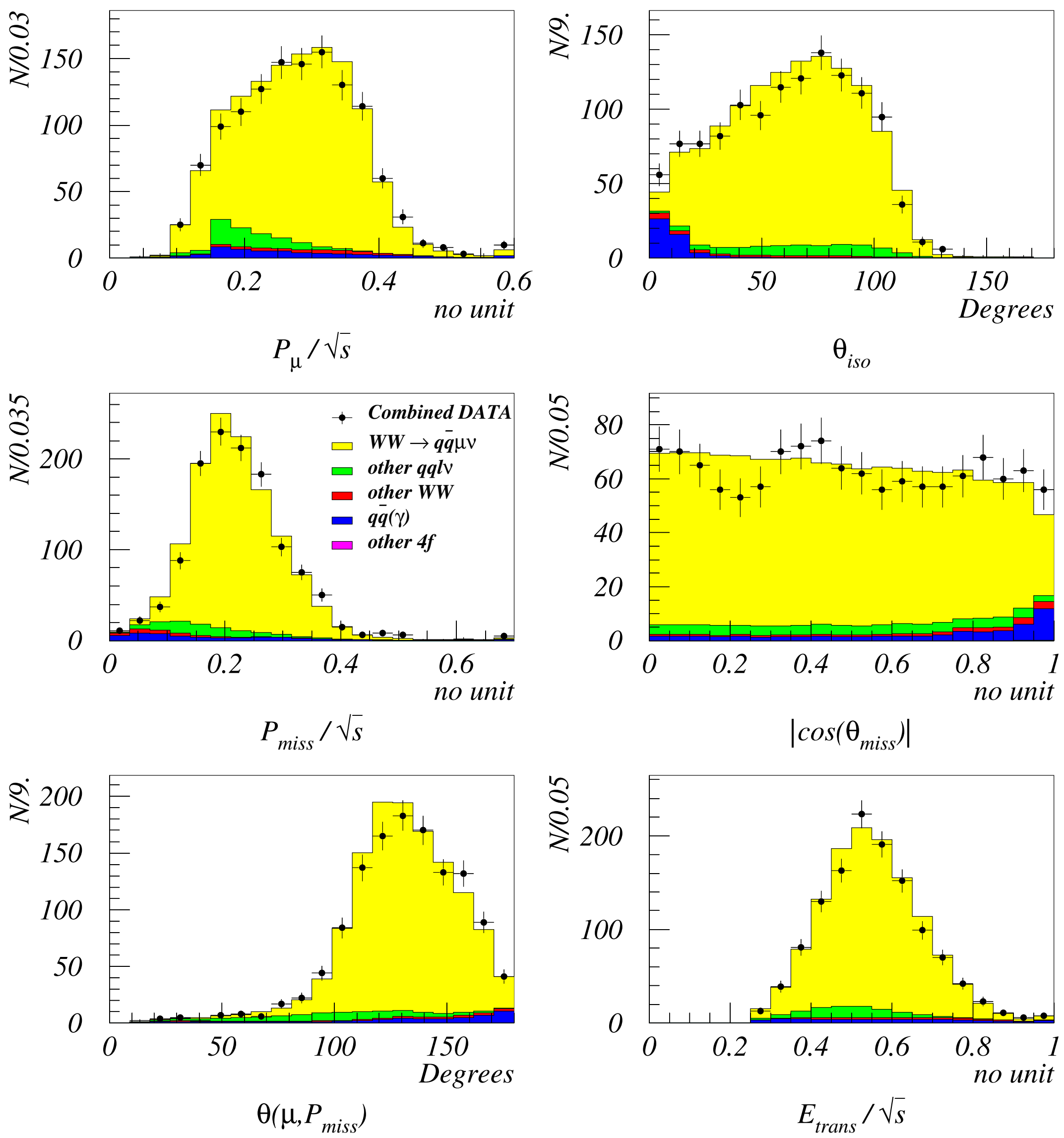

Figure B.4: Comparison between data and Monte Carlo predictions for all $qq\mu\nu$ neural network input variables, after preselections.

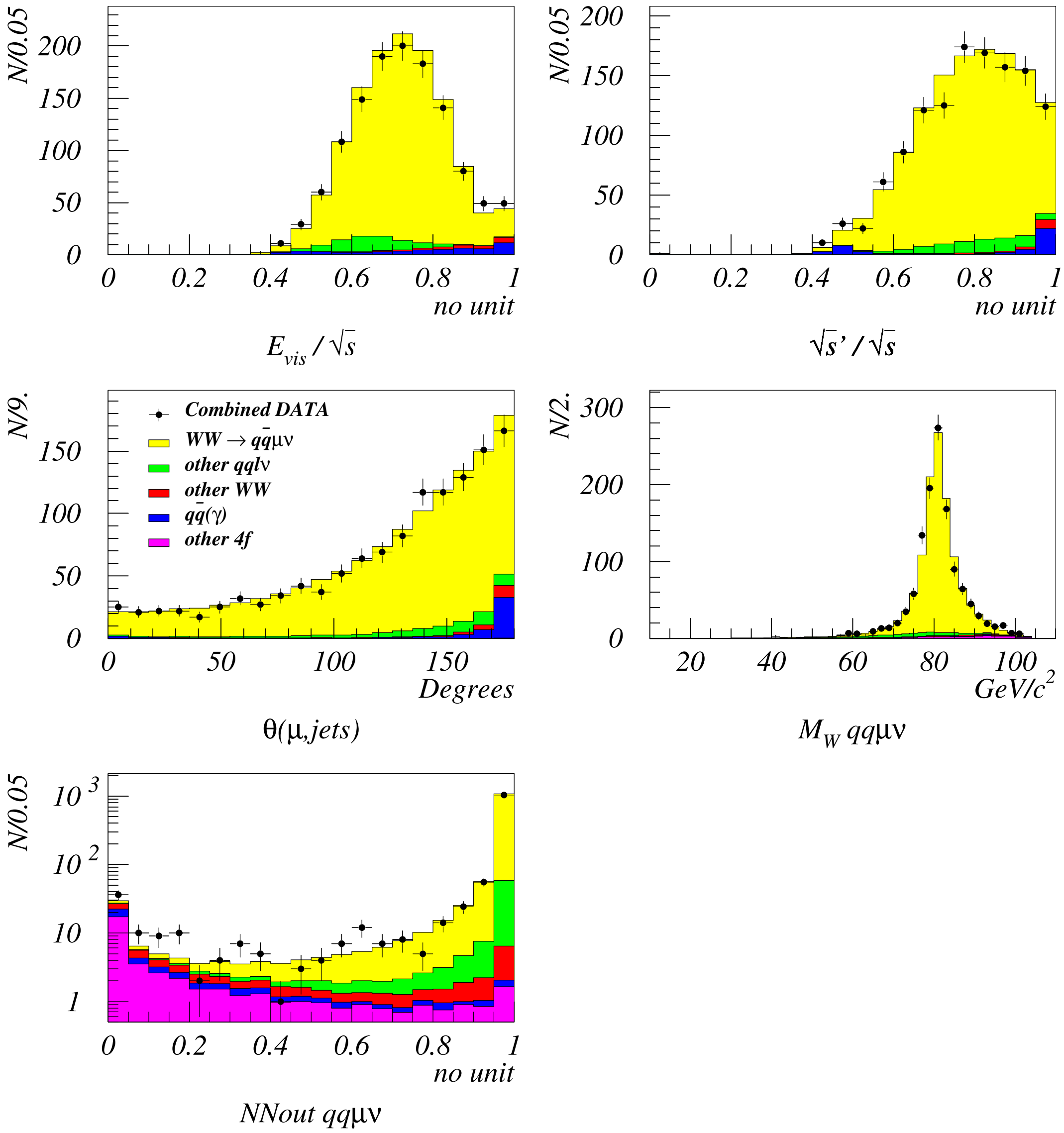

Figure B.5: Comparison for all $qq\mu\nu$ neural network input variables after preselections, continued. The last two plots show the reconstructed W mass using a 5C constrained fit and the neural network output variable respectively.

2. **Electron events** An event is considered as an electron event if a tagged electron is detected. The same pre-cuts are applied to the electron candidate events, including the additional requirement that the polar angle of the electron lies between 20° and 160°. The final cut on the neural network output amounts to 0.4 as well. A very good agreement between the data and the predictions from Monte carlo simulation can be observed in Figs. B.6 and B.7.

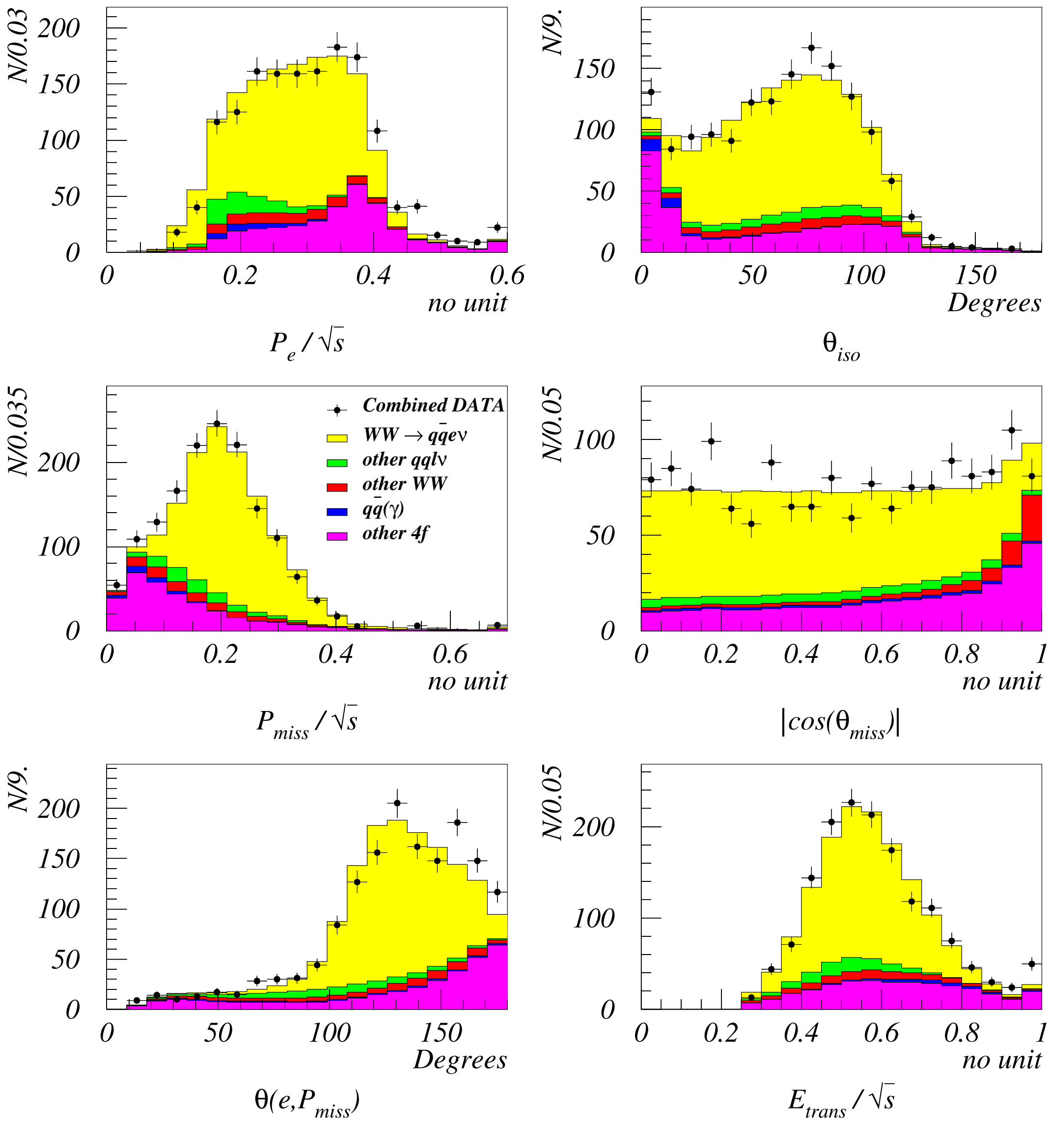

Figure B.6: Comparison for all $qqe\nu$ neural network input variables after preselections.

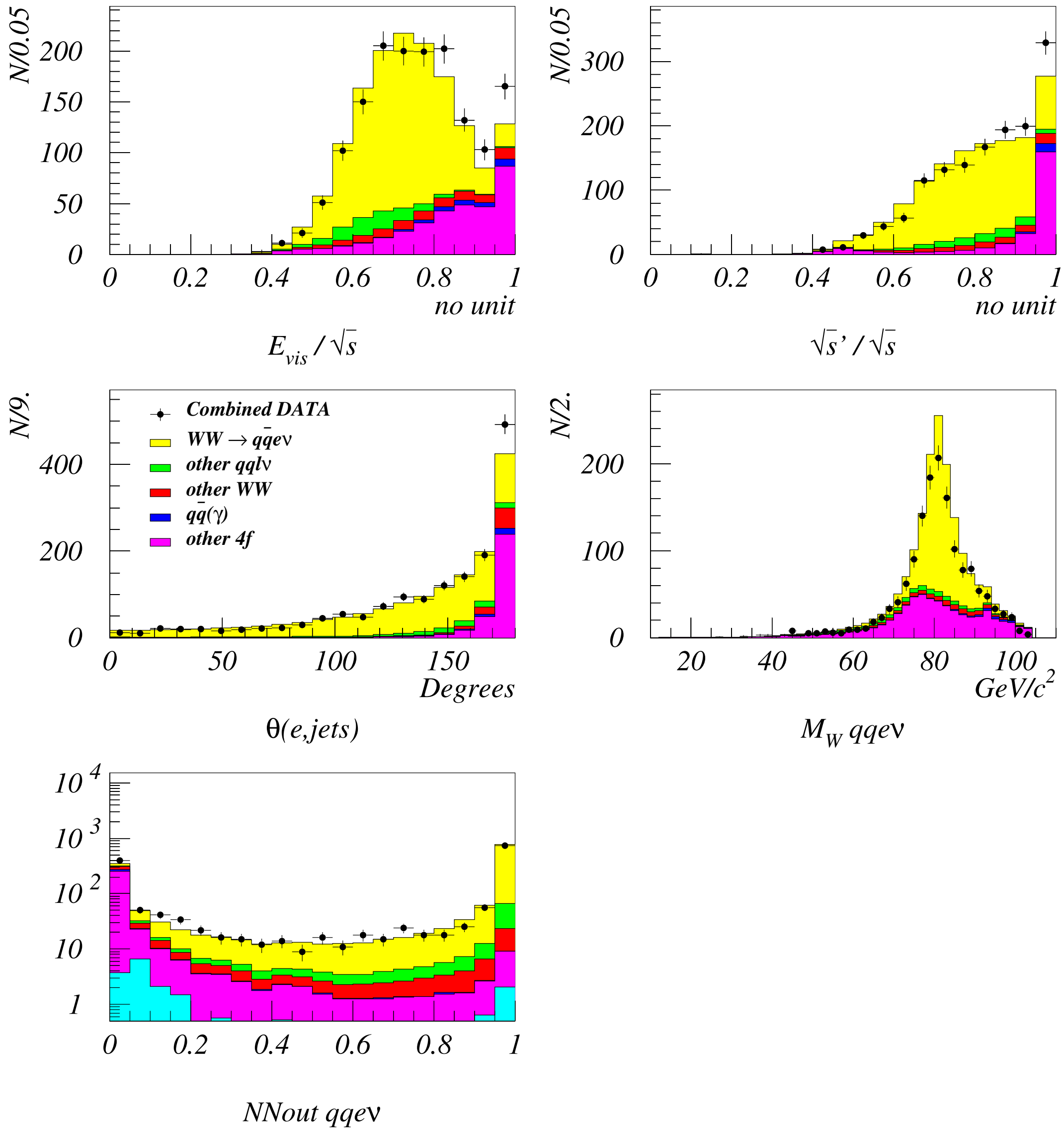

Figure B.7: Comparison for all $qqe\nu$ neural network input variables after preselections, continued. The last two plots show the reconstruced W mass using a 5C constrained fit and the neural network output variable respctively.

3. **Tau events** The following pre-cuts are common to both one prong tau and multi-prong tau categories:
   (a) the total visible energy less than 0.85 $\sqrt{s}$;
   (b) the effective center of mass energy $\sqrt{s'} < \sqrt{s}-$ 10 GeV;
   (c) the polar angle of the missing momentum between $15°$ and $165°$;
   (d) the jet separation variable y_{34} of the Durham clustering algorithm [70] has to be lower than 0.03
   (e) the $\sqrt{s'}$ value cannot be lower than 105 GeV or be smaller than $\sqrt{s}-$ 25 GeV if simultaneously the missing momentum has a polar angle between $35°$ and $145°$.
4. **Single isolated track** If a single isolated track is tagged, the event is rejected if the azimuthal angle between the 2 hadronic jets is bigger than $165°$ and if simultaneously the angle between the track and the hadronic event plane is between $83°$ and $97°$. If the isolated track is identified as a muon or an electron the sum of the energies of all neutral tracks in a cone of $15°$ around the lepton can not exceed 10 GeV, otherwise it is classified in the narrow tau jet category. In addition the number of neutrals in this cone was calculated to make a further classification. If the sum of the energy of the isolated track and its surrounding neutrals is bigger than 5 GeV and if the product of this energy with the isolation angle of the track is bigger than $150°\mathrm{GeV}$ a first classification is made:
   (a) tau type = 1 if the isolated track is identified as an electron
   (b) tau type = 2 if the isolated track is identified as a muon
   (c) tau type = 3 if the isolated track is not identified and had no surrounding neutrals
   (d) tau type = 4 if the isolated track is not identified and had one or more surrounding neutrals
5. **Narrow tau jet** If a narrow tau jet is found, its energy spread (angle that contains 75% of the jet energy) could not be bigger than $10°$. The same requirements on azimuthal angles and aplanarities are imposed on the tau jet candidate as on a single isolated track. After a search for the charged track with the biggest energy in the tau jet, all charged and neutral tracks surrounding it in a cone of $15°$ are searched for. All the energies of these particles are added to the energy of the 'main' tau track. This energy has to exceed 5 GeV, while its product with the isolation angle of the tau jet has to be bigger than $150°\mathrm{GeV}$. Again a classification is made:
   (a) tau type = 3 if only one charged track and no neutral tracks are surrounding the main track
   (b) tau type = 4 if only one charged track and one or more neutrals are surrounding the main track
   (c) tau type = 5 if three charged tracks and no neutrals are surrounding the main track
   (d) tau type = 6 in all other cases

6. **Neural network inputs for tau events** For all categories of tau events the same 14 neural network inputs are chosen:

   (a) the thrust value of the event;

   (b) the polar angle of the hadronic di-jet system;

   (c) the polar angle of the W^-;

   (d) the angle between the 2 hadronic jets;

   (e) the azimuthal angle between the 2 hadronic jets;

   (f) the minimum angle between the lepton or leptonic jet and the 2 hadronic jets;

   (g) the energy of the lepton and its surrounding particles in a cone of $15°$.

   (h) $|\cos(\theta_{\mathrm{miss}})|$;

   (i) the category to which the tau event is classified;

   (j) the total transverse momentum;

   (k) the angle between the lepton or leptonic jet and the combined di-jet momentum;

   (l) the effective center of mass energy $\sqrt{\mathrm{s}'}$;

   (m) the isolation angle of the lepton or leptonic jet;

   (n) the angle between the lepton or leptonic jet and the hadronic event plane.

   Since the tau selection has more contamination from background events, it was chosen to cut harder on its neural network output variable. The final neural network output is required to be bigger than 0.9, while only tau events of category 1 to 3 are used in the analysis in order to increase further the purity. All neural network input variables and the output variable for the tau selection are shown in Figs. B.8- B.10, showing an excellent agreement between data and Monte Carlo. The overall selection efficiency and purity for all lepton flavors is shown in Table B.1 as a function of the center-of-mass energy.

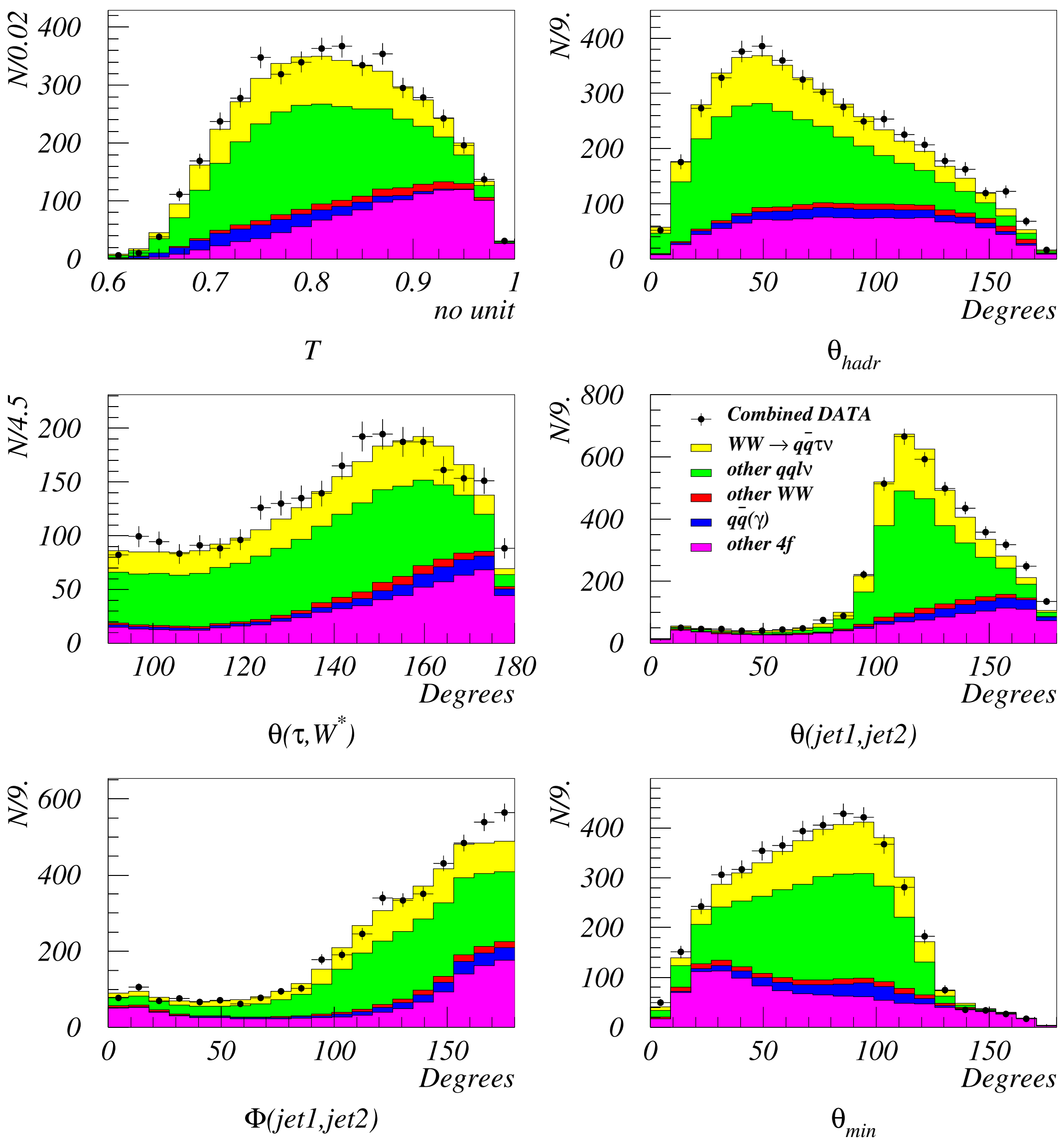

Figure B.8: Comparison for all $qq\tau\nu$ neural network input variables after preselections.

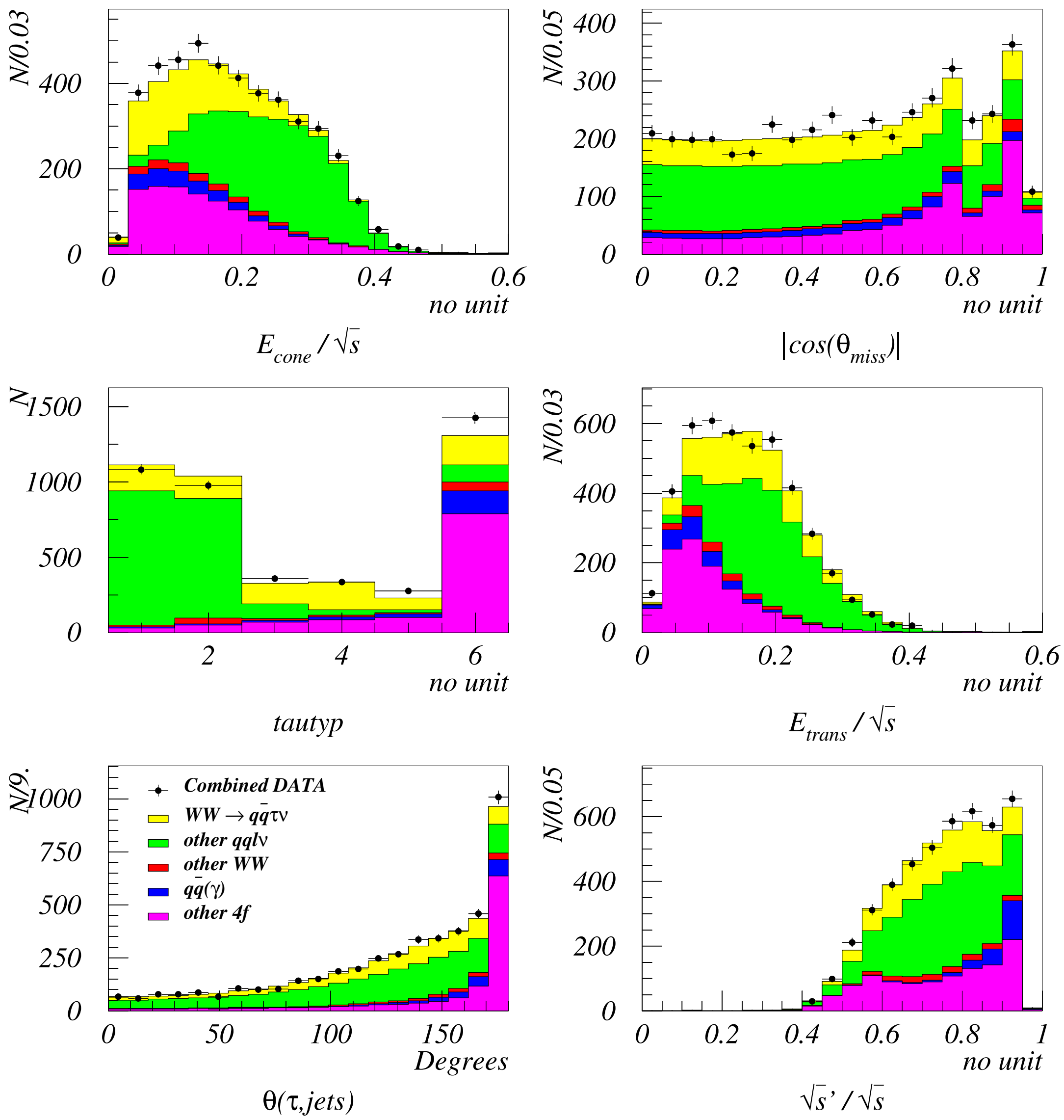

Figure B.9: Comparison for all $qq\tau\nu$ neural network input variables after preselections, continued.

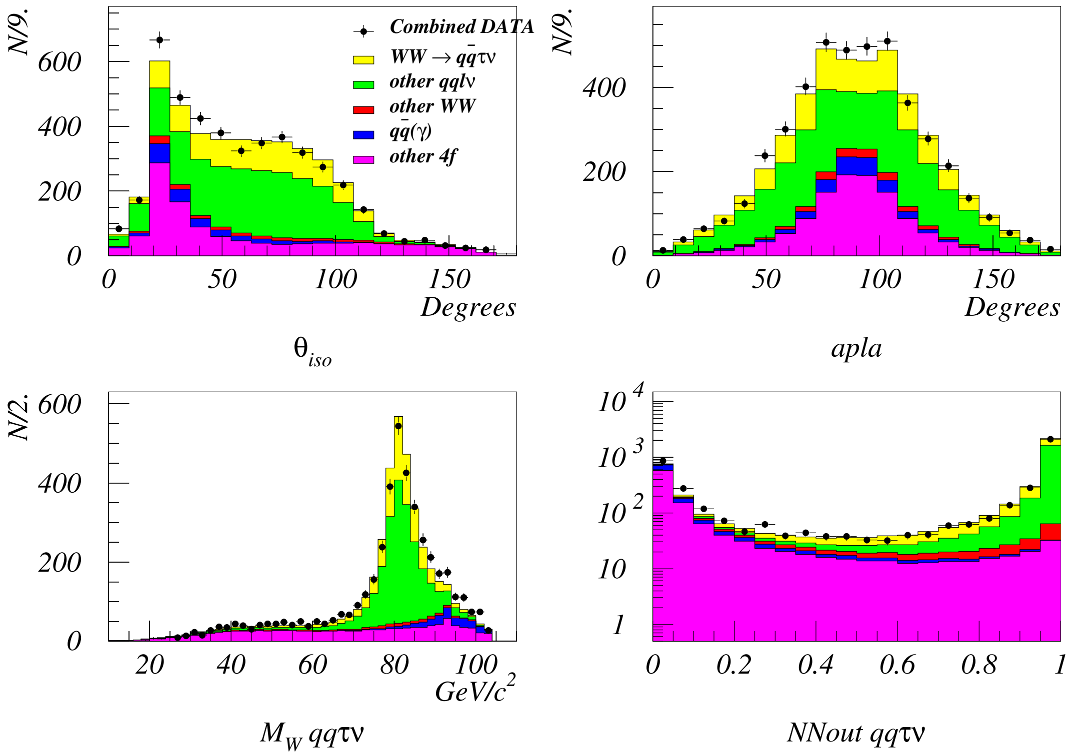

Figure B.10: Comparison for all $qq\tau\nu$ neural network input variables after preselections, continued. The last two plots show the reconstruced W mass using a 5C constrained fit and the neural network output variable respctively.

Energy	nnout cut	-0.3	0.0	0.3	0.6	0.9	$q\bar{q}l\nu$
189 GeV	eff	0.84	0.81	0.75	0.66	0.32	0.61
	pur	0.81	0.84	0.88	0.91	0.96	0.96
	obs	1346	1250	1120	975	447	733
	exp	1369	1256	1135	960	439	768
192 GeV	eff	0.84	0.80	0.74	0.64	0.35	0.61
	pur	0.83	0.86	0.89	0.92	0.96	0.95
	obs	228	208	184	152	69	116
	exp	221	203	182	153	80	124
196 GeV	eff	0.82	0.77	0.69	0.57	0.25	0.61
	pur	0.85	0.88	0.90	0.93	0.97	0.96
	obs	681	602	505	412	167	385
	exp	657	592	520	418	172	370
200 GeV	eff	0.85	0.81	0.75	0.64	0.33	0.61
	pur	0.82	0.86	0.89	0.92	0.97	0.96
	obs	763	696	626	506	257	418
	exp	769	705	631	515	252	426
202 GeV	eff	0.83	0.79	0.73	0.63	0.38	0.60
	pur	0.83	0.86	0.89	0.92	0.96	0.96
	obs	371	339	301	247	135	206
	exp	365	334	300	251	144	207
> 202 GeV	eff	0.85	0.81	0.74	0.61	0.33	0.60
	pur	0.81	0.85	0.89	0.93	0.97	0.96
	obs	1569	1421	1240	960	495	709
	exp	1541	1404	1234	973	506	775
Total number observed		4958	4516	3976	3252	1570	2567
Total number expected		4922	4494	4002	3270	1593	2670

Table B.1: Efficiencies, purities, number of observed data events and the expectation from the MC simulation. The signal and background events were all simulated using the WPHACT event generator, hadronized with JETSET, except for the $q\bar{q}(\gamma)$ background which was simulated with KK2f. The last column gives the overall selection performance for semi-leptonic events, the other columns give the performance of the fully-hadronic slection for various neural network output cuts.

Appendix C

Comparison between event shapes for mixed and real 4q events

The following plots give a comparison of all fully-hadronic neural network input distributions between fully-hadronic events and "mixed" events. To these variables, a set of seven other useful variables was added:

1. the number of charged particles in the event;
2. the amount of missing momentum;
3. the $D_{4C} = \frac{E_{min}}{E_{max}} \frac{\theta_{min}}{E_{max} - E_{min}}$ variable;
4. the number of natural jets, clustered with LUCLUS, using a resolution variable $y_{ij} = 6.5$;
5. the neural net output variable;
6. the W mass after a 5C constrained fit;
7. the polar angle of the fitted W momenta.

In Figs. C.1–C.5 a comparison between fully-hadronic and mixed events is made for the real data. The $q\bar{q}$ background contribution is also shown by the dark shaded histogram. The same comparison is made for Monte Carlo events in Figs. C.6–C.10. Finally, in Figs. C.11 and C.12, four relevant single-particle spectra, are compared for mixed and real fully-hadronic events, using real data and Monte Carlo events respectively. These spectra consist of the momentum, $|p|$ of the particles, their transverse momentum w.r.t the W momentum direction, p_t, the rapidity w.r.t. the W momentum, y, and the polar angle w.r.t. the z axis. The p and p_t spectra are in dimensionless units, since they are normalised to the centre-of-mass energy.

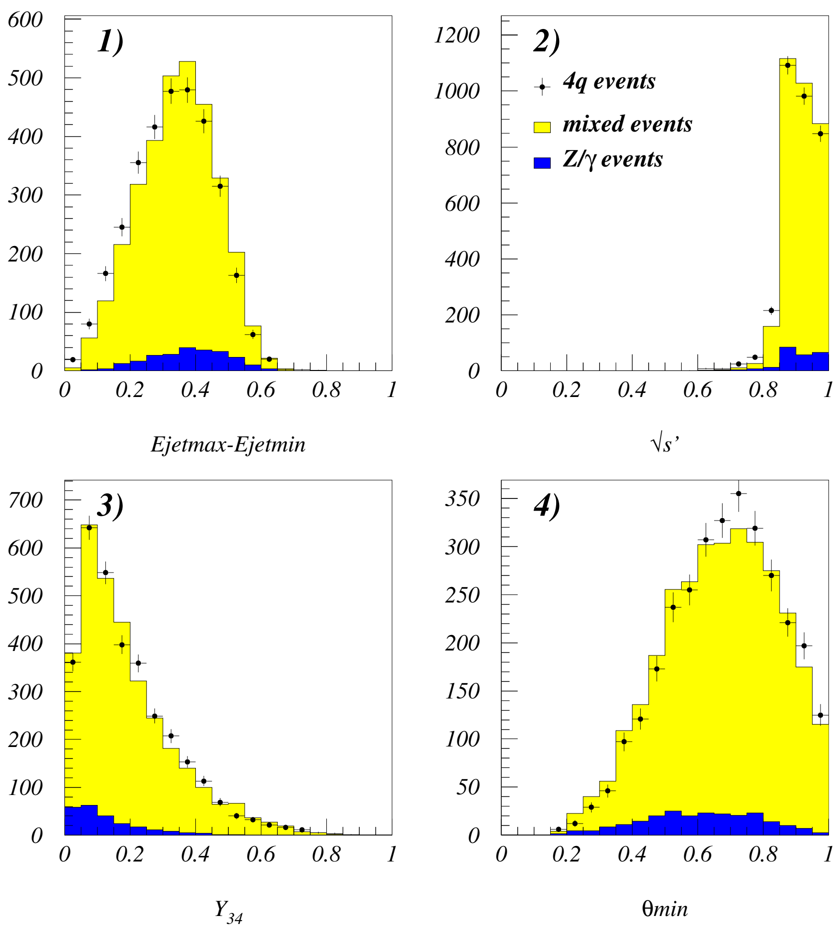

Figure C.1: Comparison of the neural network input variables (numbered 1 to 13 in section 7.2.1) between the real $(4q)$ combined data (full dots), the mixed events (histogram) and background (dark coloured) on this and the next four pages. The quantities on the x-axis are normalized to the interval (0., 1.). Seven extra quantities, described above, are also shown.

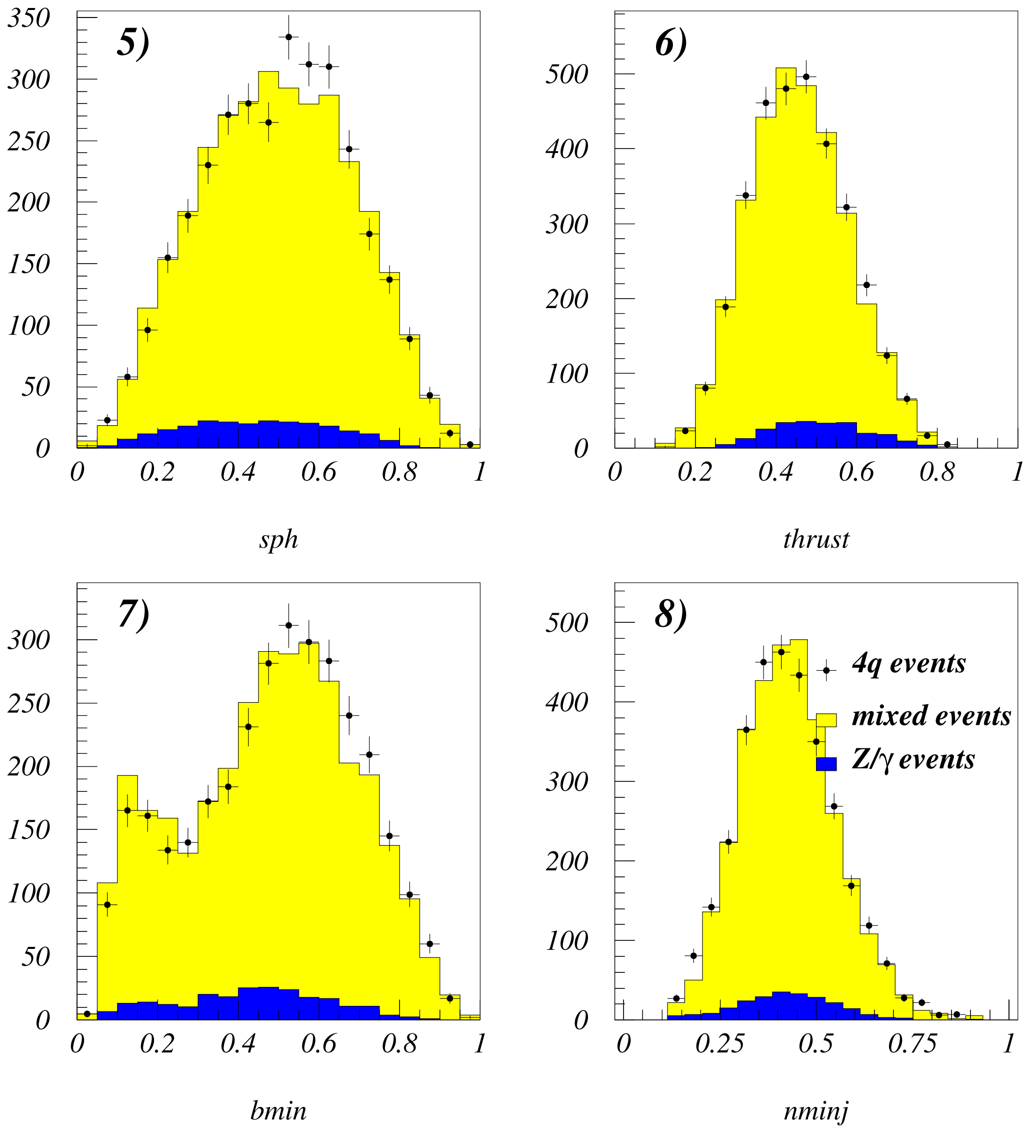

Figure C.2: Fig. C.1 continued.

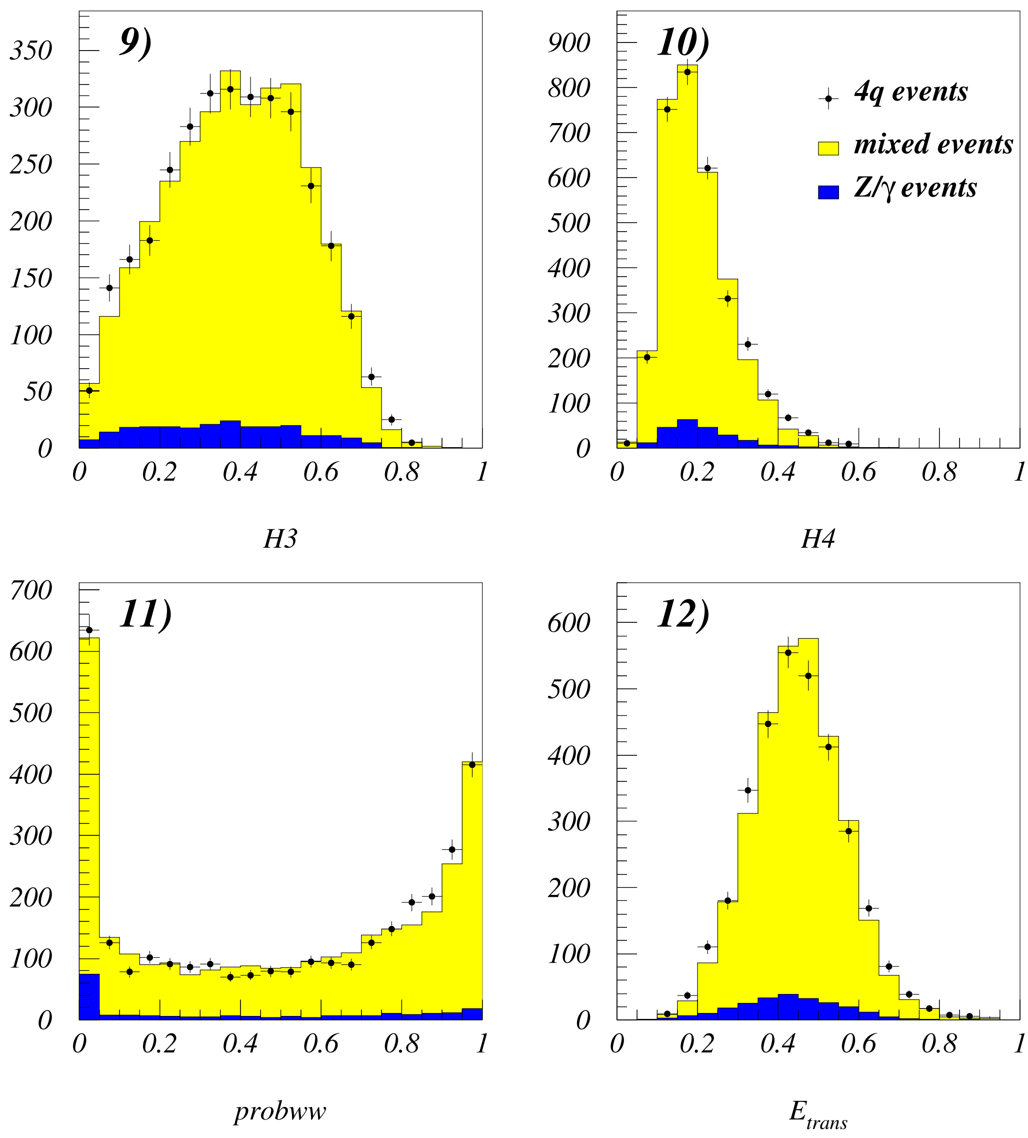

Figure C.3: Fig. C.1 continued.

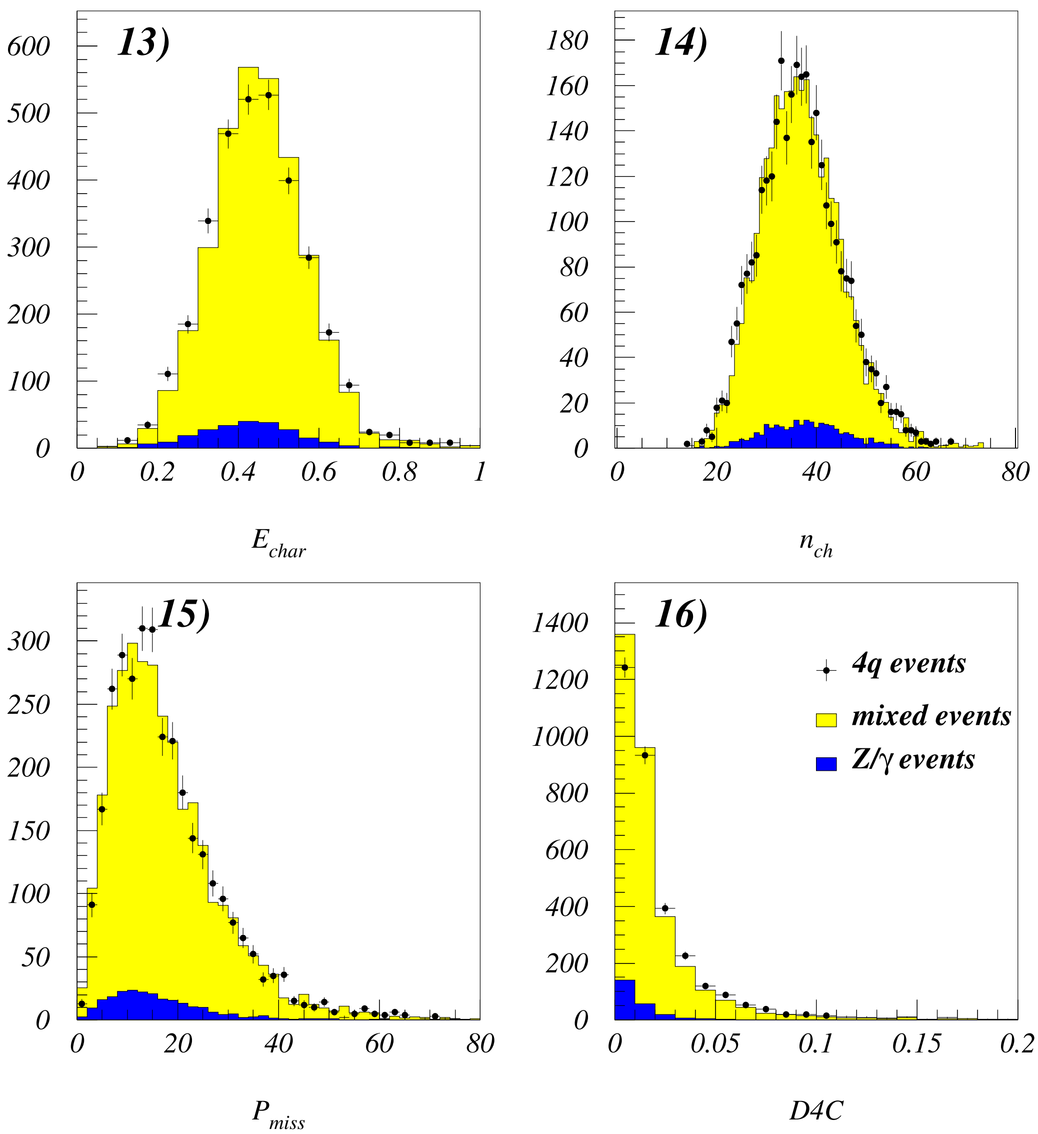

Figure C.4: Fig. C.1 continued.

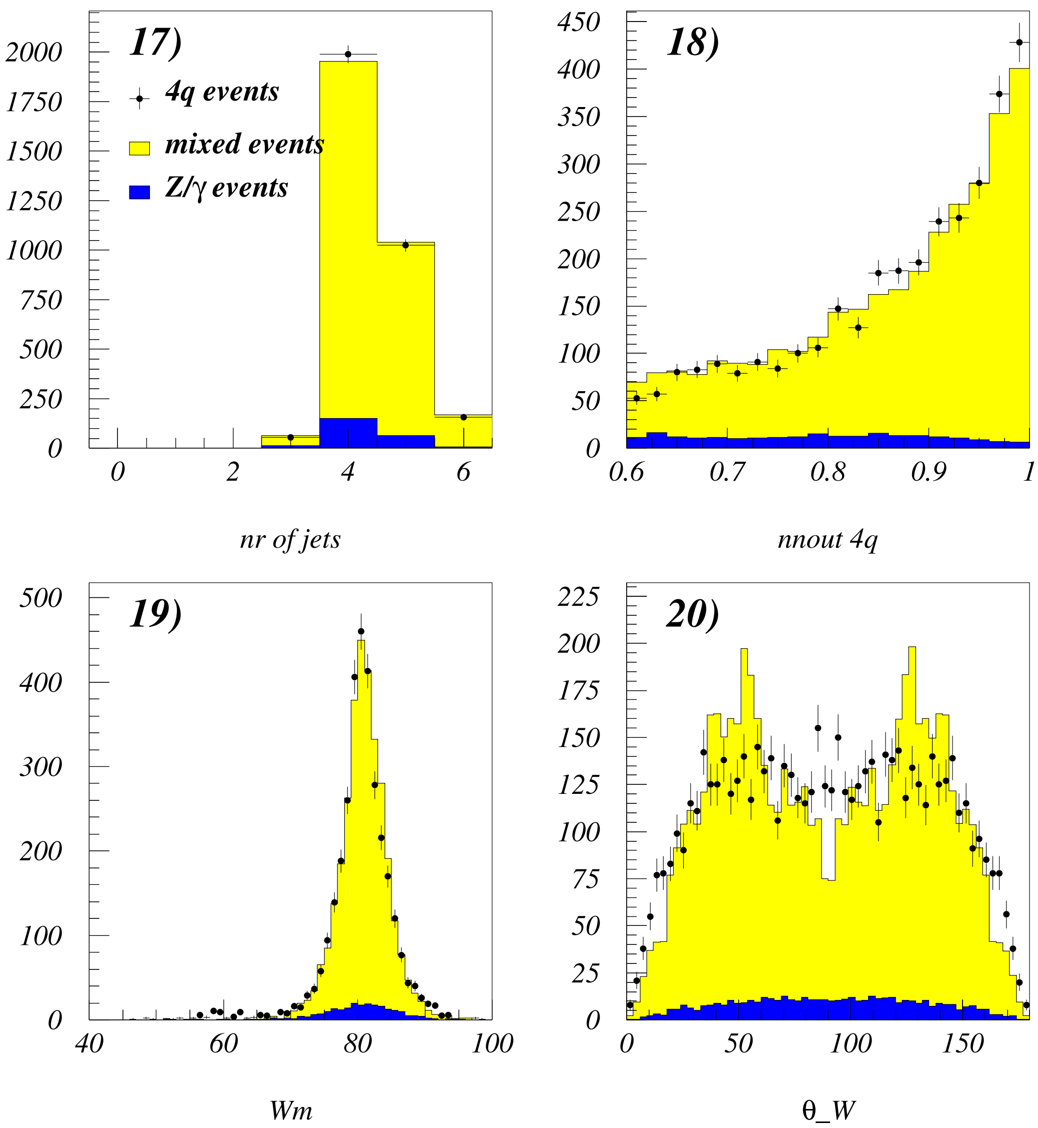

Figure C.5: Fig. C.1 continued.

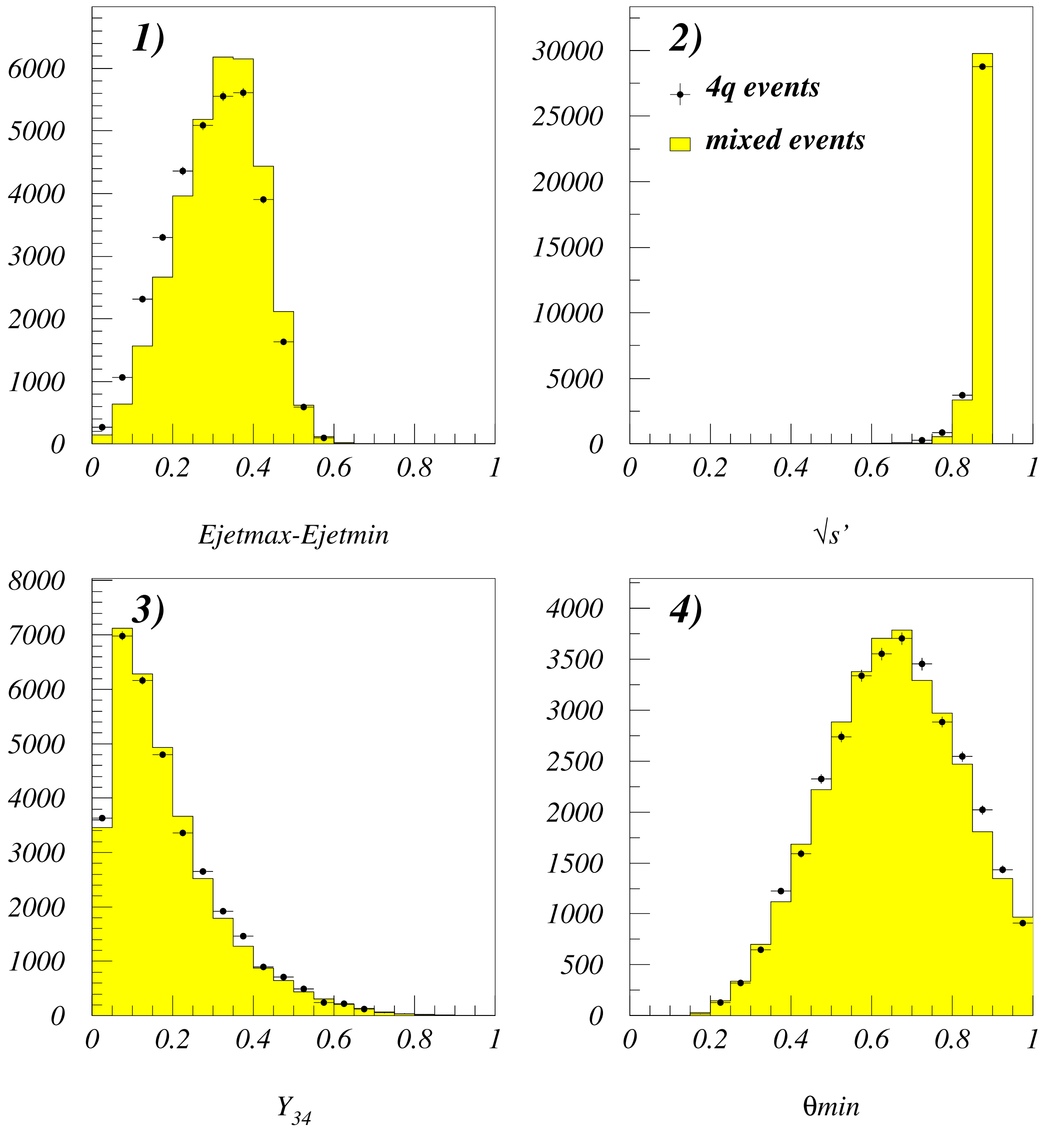

Figure C.6: Same as in previous figure with $(4q)$ events obtained from a BEins MC (full points), and mixed MC events (histogram).

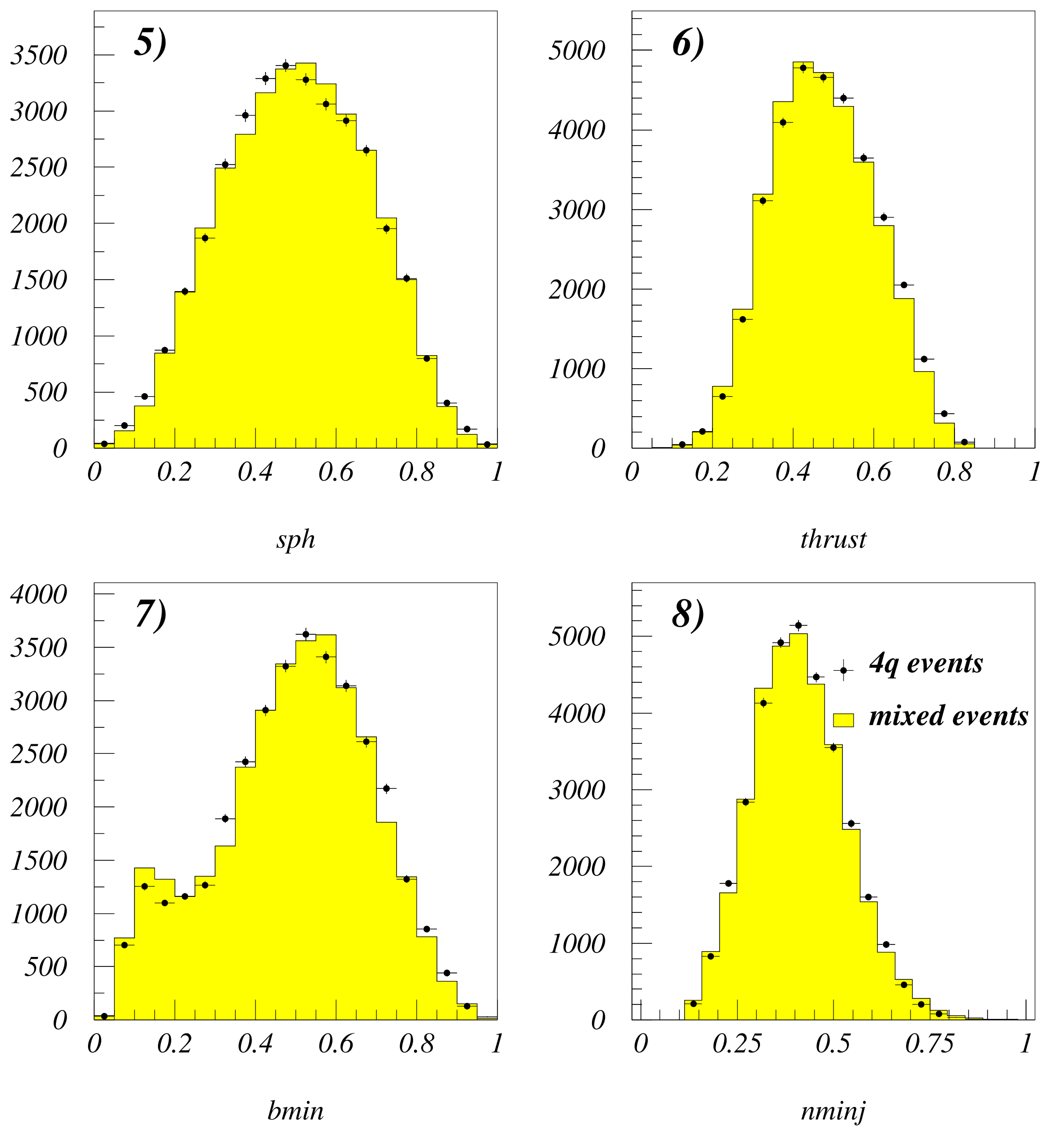

Figure C.7: Fig. C.6, continued.

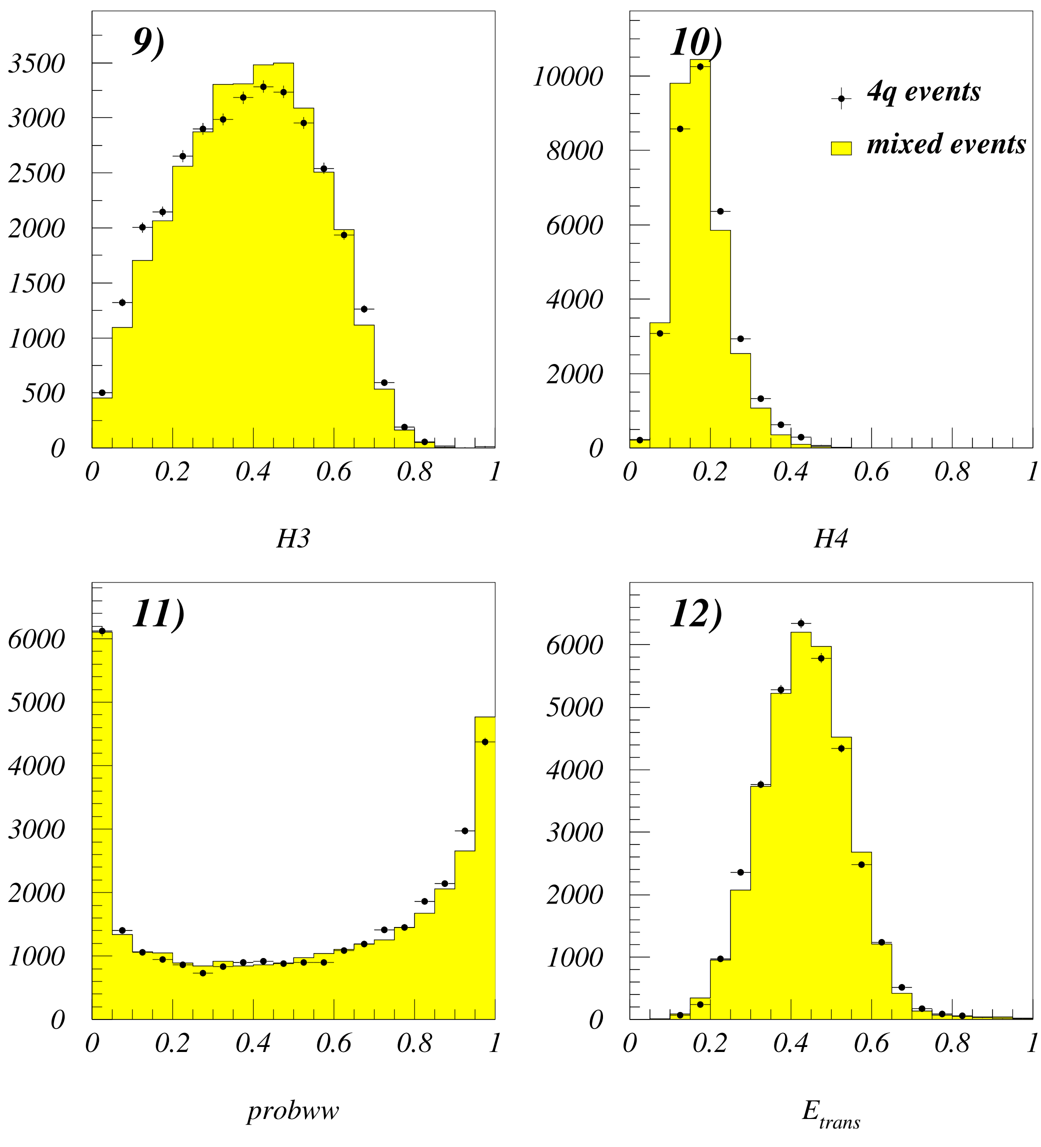

Figure C.8: Fig. C.6, continued.

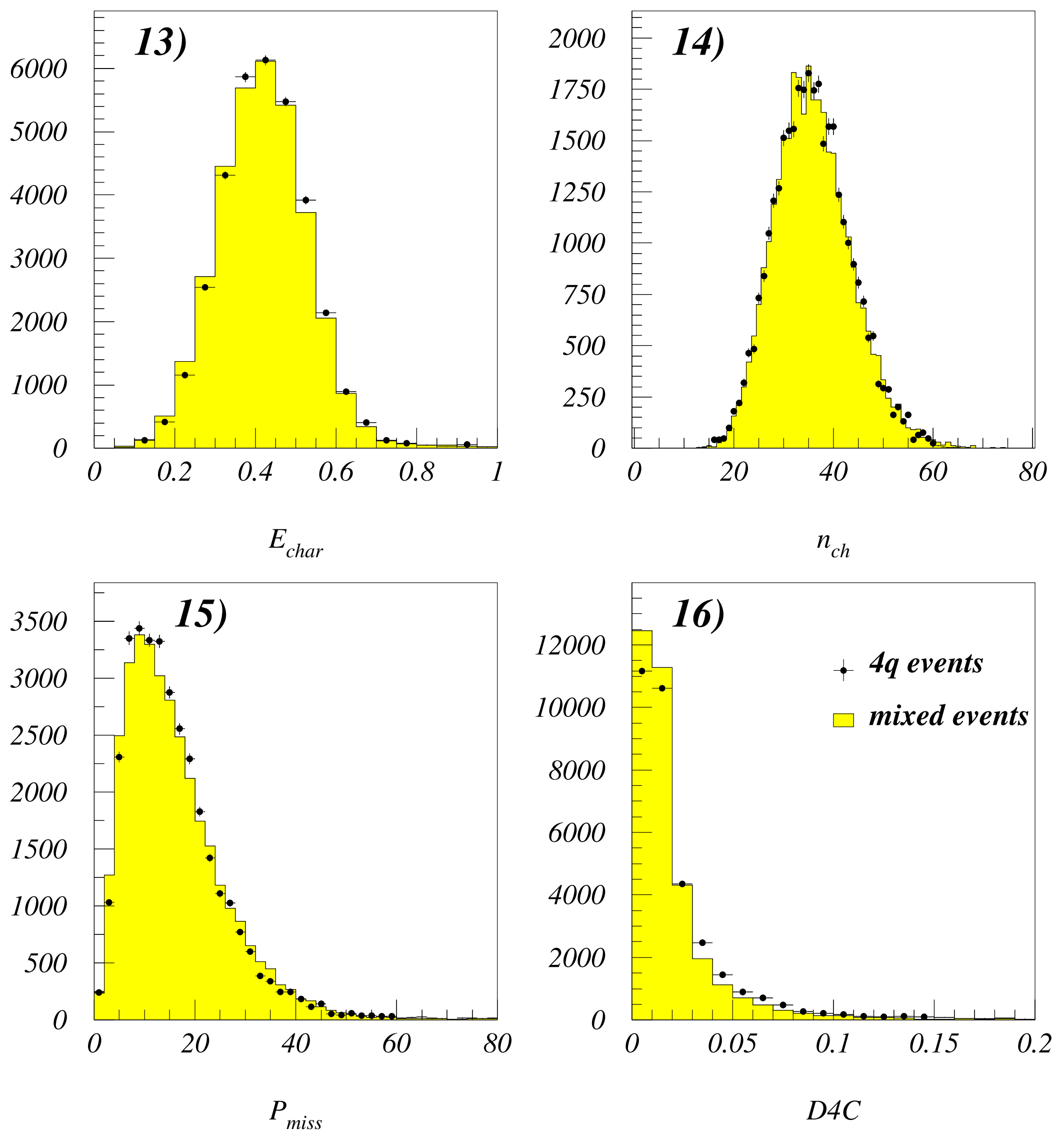

Figure C.9: Fig. C.6, continued.

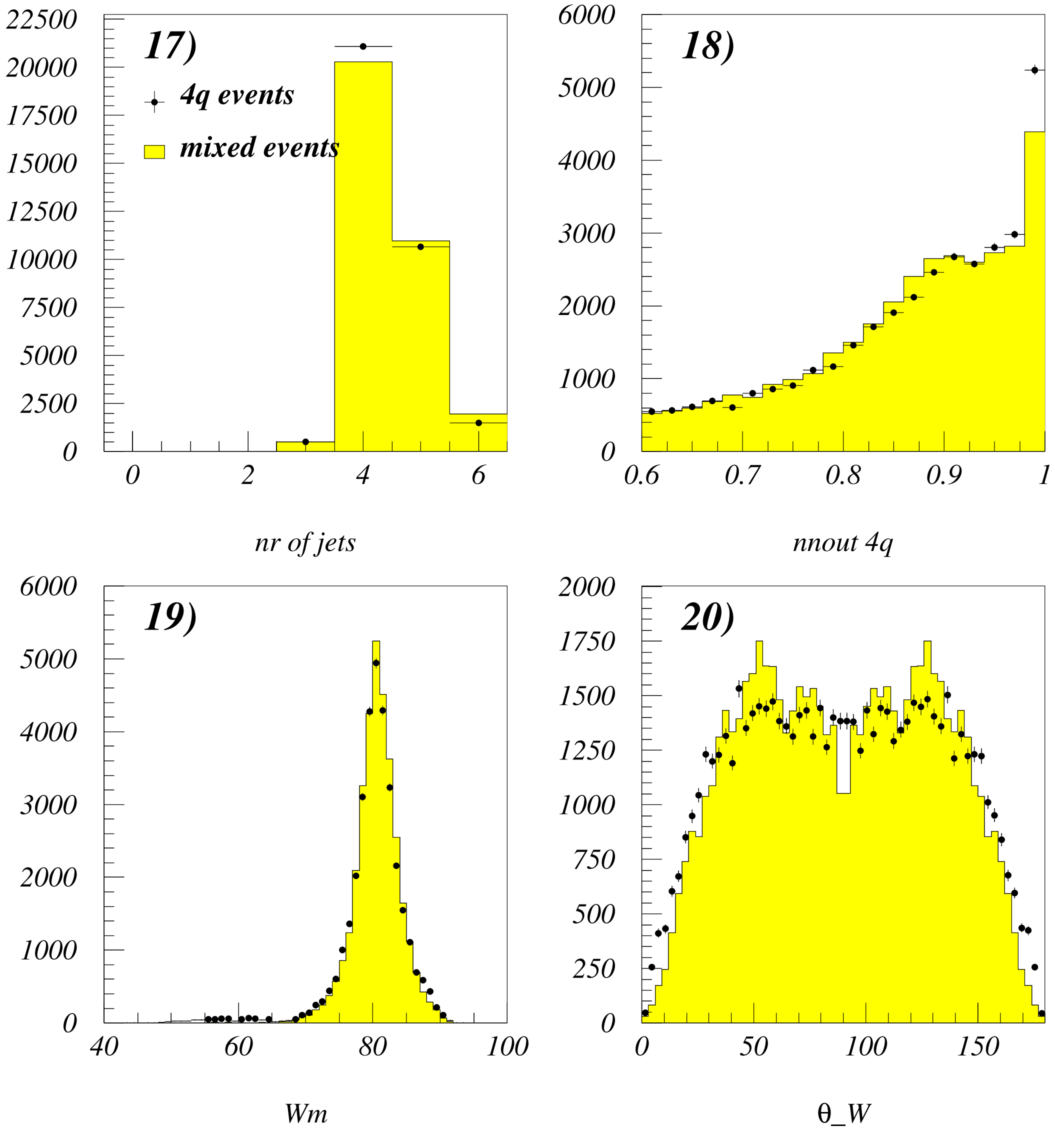

Figure C.10: Fig. C.6, continued.

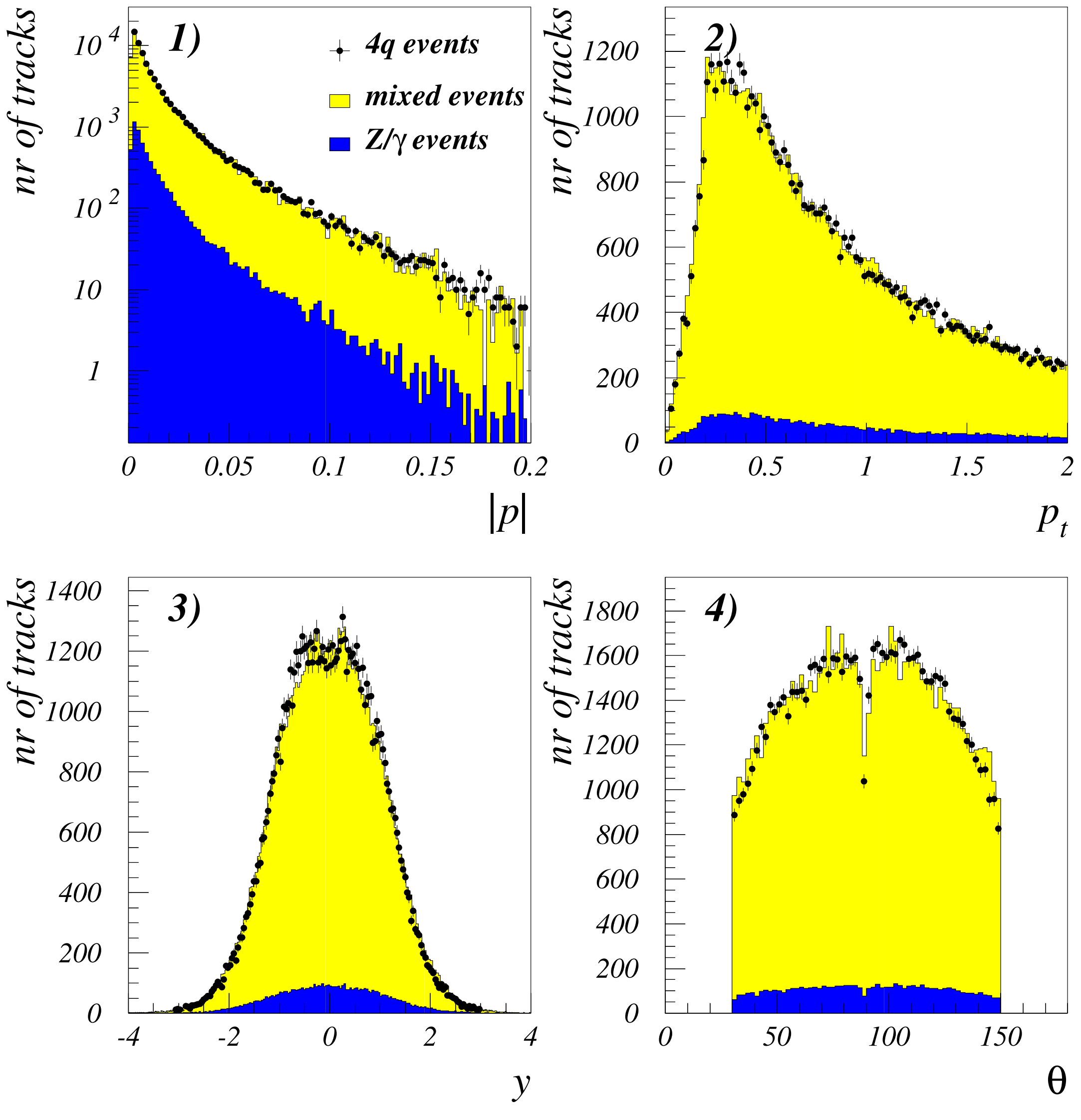

Figure C.11: Distribution of the momentum (1), the transverse momentum wrt. the W direction (2), rapidity wrt the W direction (3) and polar angle (4) of real $(4q)$ combined data events (data points), mixed events (histogram) and background events (coloured histogram).

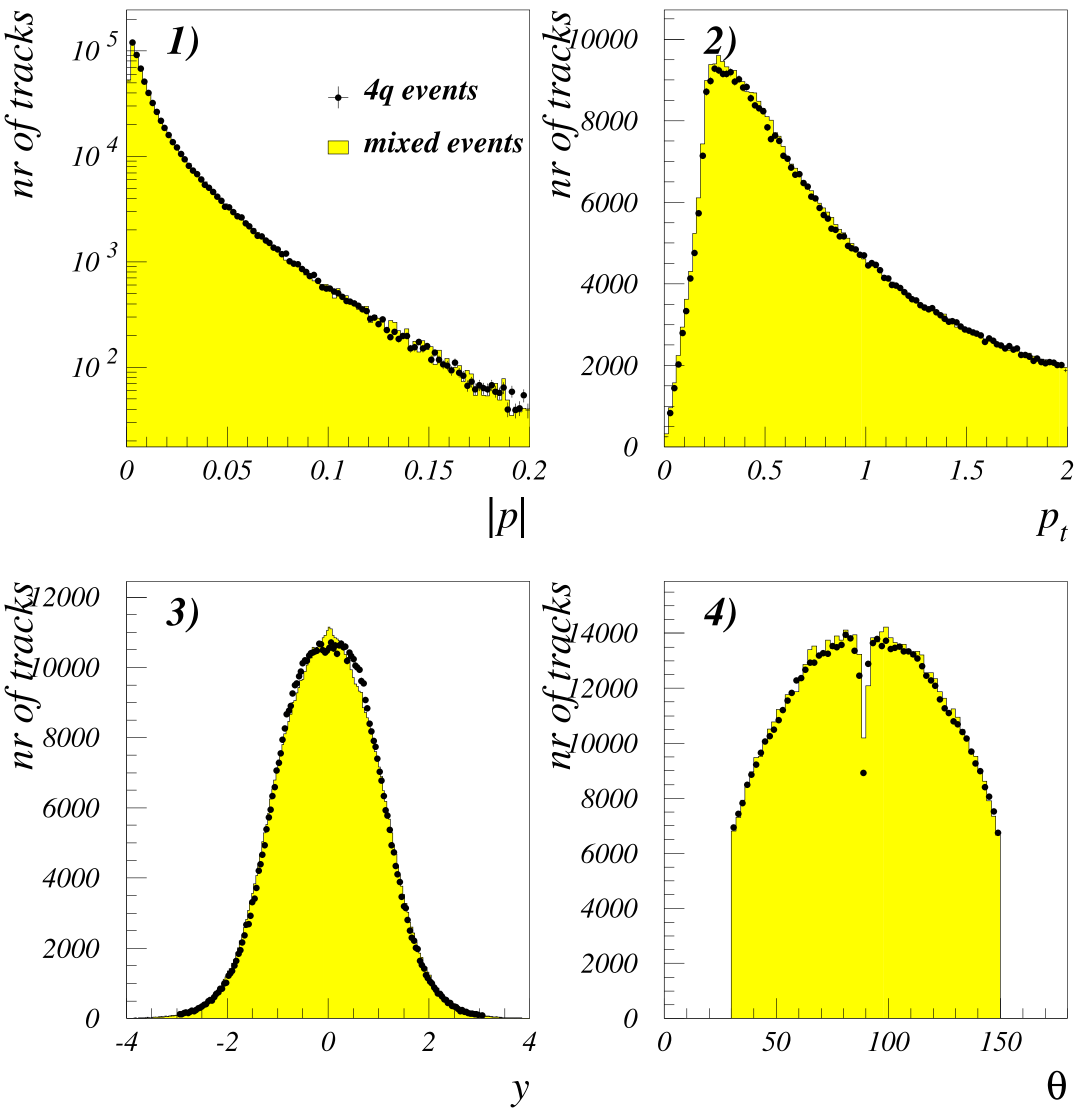

Figure C.12: As in previous figure for $(4q)$ events and mixed events obtained from a BEins MC simulation.

Bibliography

[1] A. Pais, *Inward Bound,* Oxford University Press (1986) 666 p.

[2] W. Pauli, Phys. Rev. 58 (1940) 716.

[3] R. Jost, Helv. Phys. Acta 30 (1957) 409.

[4] N. Burgoyne, Il Nuovo Cimento VIII 4 (1958) 607.

[5] E.A. De Wolf, I.M. Dremin and W. Kittel, Phys. Rept. **270** (1996) 1.

[6] B. Lörstad, Int. J. Mod. Phys. **A12** (1989) 2861.

[7] see e.g. B. Saleh, *Photoelectron Statistics* Springer Series in optical sciences, vol. 6, Springer, Berlin, 1978.

[8] R. Hanbury Brown and R.Q. Twiss, Nature **178** (1956) 1046.

[9] G. Goldhaber et al., Phys. Rev. Lett. **3** (1959) 181.

[10] G. Goldhaber et al., Phys. Rev. **120** (1960) 300.

[11] R.M. Weiner, *Introduction to Bose-Einstein correlations and subatomic interferometry,* Wiley & Sons (2000) 244p.

[12] [L3 Coll.], P. Achard et al., Phys. Lett. **B524** (2002) 55.

[13] S. Pratt, T. Csörgo and J. Zimányi, Phys. Rev. **C 42** (1990) 2646.

[14] S. Chapman and U. Heinz, Phys. Lett. **B340** (1994) 250.

[15] M. Gyulassy, S. K. Kauffmann and L. W. Wilson, Phys. Rev. **C20** (1979) 2267.

[16] B. Andersson, *The Lund model,* Cambridge, UK: Univ. Pr. (1998) 471 p.

[17] B. Andersson, G. Gustafson, G. Ingelman, and T. Sjostrand, Phys. Rept. **97** (1983) 31.

[18] B. Andersson, *Coherence and incoherence in Bose-Einstein correlations,* Proc. XXXth Int. Symp. on Multiparticle Dynamics, edts. T. Csörgo et al.(World Scientific Singapore, 2001).

[19] L. Landau and E. Lifshitz, *Théorie quantique relativiste,* Vol. 1 (Ed. Mir, Moskow, 1982) p.475.

[20] B. Andersson and W. Hofmann, Phys. Lett. **B169** (1986) 364.

[21] B. Andersson and M. Ringnér, Nucl. Phys. **B513** (1998) 627;
B. Andersson and M. Ringnér, Phys. Lett. **B421** (1998) 283;
J. Hakkinen and M. Ringnér, Eur. Phys. J. **C5** (1998) 275.

[22] E.A. De Wolf, *Correlations in $e^+e^- \to W^+W^-$ hadronic decays,* hep-ph/0101243.

[23] G. Alexander, *Bose-Einsein and Fermi-Dirac Interferometry in Particle Physics,* hep-ph/0302130.

[24] W. Kittel, Acta Phys. Polon. **B32** (2001) 3927.

[25] [ZEUS Coll.], S. Chekanov et al., Contributed paper to ICHEP 2002, abs.839.

[26] G. I. Kopylov and M. I. Podogretskii, Sov. J. Nucl. Phys. **15** (1972) 219.

[27] G. I. Kopylov and M. I. Podogretskii, Sov. J. Nucl. Phys. **18** (1973) 336.

[28] G. I. Kopylov, Phys. Lett. **B50** (1974) 472.

[29] [MARKII Coll.], I. Juricic et al., Phys. Rev. **D39** (1989) 1.

[30] [TASSO Coll.], M. Althoff et al., Z. Phys. **C30** (1986) 355.

[31] [DELPHI Coll.], P. Abreu et al., Phys. Lett. **B286** (1992) 201.

[32] [EMC Coll.], M. Arneodo et al., Z. Phys. **C32** (1986) 1.

[33] [NA22 Coll.], M. Adamus et al., Z. Phys. **C37** (1988) 347.

[34] [UA1 Coll.], C. Albajar et al., Phys. Lett. **B226** (1989) 410.

[35] [ZEUS Coll.], M. Derrick Acta Phys. Polon. **B33** (2002) 3281.

[36] [DELPHI Coll.], P. Abreu et al., Phys. Lett. **B379** (1996) 330.

[37] [ALEPH Coll.], D. Buskulic et al., Z. Phys. **C64** (1994) 361.

[38] [OPAL Coll.], G. Abbiendi et al., *Fermi-Dirac Correlations Between Antiprotons in Hadronic Z^0 Decays* OPAL Physics note PN486, 2002.

[39] [OPAL Coll.], G. Alexander et al., Phys. Lett. **B384** (1996) 377.

[40] [L3 Coll.], P. Achard et al., Phys. Lett. **B540** (2002) 185.

[41] J. A. van Dalen, *Bose-Einstein correlations in e^-e^- events,* Ph.D. Thesis, University of Nijmegen, 9/01/2002.

[42] [DELPHI Coll.], P. Abreu et al., Phys. Lett. **B471** (2000) 460.

[43] [L3 Coll.], M. Acciarri et al., Phys. Lett. **B458** (1999) 517.

[44] [DELPHI Coll.], P. Abreu et al., Z. Phys. **C63** (1994) 17.

[45] [STAR Coll.], C. Adler et al., Phys. Rev. Lett. **87** (2001) 082301.

[46] R.K. Ellis, W.J. Stirling and B.R. Webber, *QCD and collider physics,* Cambridge Monogr. Part. Phys. Nucl. Phys. Cosmol., 1996.

[47] T. Sjöstrand et al., *High-energy-physics event generation with PYTHIA 6.1,* Comp. Phys. Comm. **135** (2001) 238.

[48] C. Peterson, D. Sclatter, I. Schmitt and P. Zerwas, Phys. Rev. **D27** (1983) 105.

[49] L. Lönnblad and T. Sjöstrand, Eur. Phys. J. **C2** (1998) 165.

[50] A. Bialass and A. Krzywicki, Phys. Lett. **B354** (1995) 134;
T. Wibig, Phys. Rev. **D53** (1996) 3586;
S. jadach and K. Zalewski, Acta Phys. Polon. **B28** (1997) 1363;
F. Fialkowski and R. Wit, Eur. Phys. J. **C13** (2000) 133;
V. Kartvelishvili and R. Kvatadze, Phys. Lett. **B514** (2001) 7.

[51] L. Lönnblad and T. Sjöstrand, Phys. Lett. **B351** (1995) 293.

[52] [DELPHI Coll.], P. Abreu et al., Z. Phys. **C73** (1996) 11.

[53] [DELPHI Coll.], P. Abreu et al., Phys. Lett. **B286** (1992) 201.

[54] G. Marchenisi and B. R. Webber, Nucl. Phys. **B238** (1984) 1.

[55] B. R. Webber, Nucl. Phys. **B238** (1984) 492.

[56] L. Lönnblad, Comp. Phys. Comm. **71** (1992) 15.

[57] [DELPHI Coll.], P. Aarnio et al., Nucl. Instr. and Meth. **A303** (1991) 233.

[58] [DELPHI Coll.], P. Abreu et al., Nucl. Instr. and Meth. **A378** (1996) 57.

[59] [DELPHI Coll.], *DELPHI data analysis program (DELANA) User's Guide,* DELPHI 98-44 PROG 137 (1989).

[60] V. Perevozchikov and N. Smirnov, *PHDST Package Description V.3 VZD - Viewer of Zebra Data for DELPHI user's manual,* DELPHI 92-118 PROG 189.

[61] F. Cossutti et al., *Improvements to SKELANA for Version 2.0,* DELPHI 99-175 PROG 239.

[62] [DELPHI Coll.], *DELPHI event generation and detector simulation - User Guide,* DELPHI 89-67 PROG 142 (1989).

[63] T. Sjöstrand and V. A.Khoze, Z. Phys. **C62** (1994) 281.

[64] L. Lönnblad, Z. Phys. **C70** (1996) 107.

[65] [The LEP collaborations, The LEP Electroweak Working Group, and the SLD Heavy Flavour Group], *A Combination of Preliminary Electroweak Measurements and Constraints on the Standard Model,* CERN-EP-2002-091.

[66] G. Altarelli,T. Sjöstrand and F. Zwirner, *Physics at LEP2* CERN yellow report, CERN 96-01.

[67] A. Ballestrero et al., *Four-fermion simulation at LEP2 in DELPHI* CERN EP 2002-069 (28 June 2002), Accepted by Comp. Phys. Commun.

[68] S. Jadach, B. F. Ward and Z. Was, Comp. Phys. Comm. **130** (2000) 260.

[69] S.V. Chekanov, E.A. De Wolf and W. Kittel, Eur. Phys. J. **C6** (1999) 403.

[70] S. Catani et al., Phys. Lett. **B269** (1991) 432.

[71] N. Kjaer and M. Mulders, *PUFITC+: DELPHI constrained fitting package*.

[72] M. Mulders, *Direct measurement of the W boson mass in e^+ e^- collisions at LEP,* Ph.D. thesis, University of Amsterdam, 2001.

[73] [DELPHI Coll.], P. Abreu et al., Phys. Lett. **B479** (2000) 89.

[74] G. Gomez Ceballos Ph.D. thesis, Instituto de Fisica de Cantabria (CSIC-Universidad de Cantabria) 25/06/2001.

[75] A. De Angelis and L. Vitale, Nucl. Instr. and Meth. **A423** (1999) 446.

[76] V. Perevoztchikov, M. Tabidze and A. Tomaradze, *Influence of the bin-to-bin and inside-bin correlations on measured quantities,* DELPHI 2000 - 027 CONF 346.

[77] [L3 Coll.], P. Achard et al., Phys. Lett. **B547** (2002) 139.

[78] Wolfram Kittel, private communications.

[79] S. Todorova-Nová, *Colour reconnection in string model,* DELPHI 96-158 PHYS 651.

[80] P. Abreu et al., *Correlations between particles in $e^+e^- - \rightarrow W^+W^-$ events,* DELPHI note 2000-115 OSAKA CONF 414.

[81] N. van Remortel et al. *Bose-Einstein correlations in $e^+e^- - \rightarrow W^+W^-$ events,* DELPHI note 2002-032 CONF 566.

[82] S. Todorova-Nova, N. van Remortel, F. Verbeure and L. Vitale, *Particle correlations in $e^+e^- \rightarrow W^+W^-$ events with the DELPHI detector,* DELPHI note 2001-107 CONF 534.

[83] [ALEPH Coll.], R. Barate et al., Phys. Lett. **B478** (2000) 50.

[84] [ALEPH Coll.], R. Barate et al., *Further studies on Bose-Einstein correlations in W-pair decays,* ALEPH notes: ALEPH-2000-039 CONF 2000-059 (2000), ALEPH-2001-64 CONF 2001-044 (2001).

[85] [OPAL Coll.], G. Abbiendi et al., Eur. Phys. J. **C8** (1999) 559.

[86] [OPAL Coll.], G. Abbiendi et al., *Bose-Einstein Correlations in* $e^+e^- \rightarrow W^+W^-$ *events at 172, 183 and 189 GeV,* OPAL note PN393 (1999).

[87] O. Klapp, *Eine umfassende Studie der Eigenschaften von Gluon- und Quark-Jets,* Ph.D. thesis, University of Wuppertal, 1999, WUB-DIS 99-16.

[88] S. Bentvelsen and I. Meyer, Eur. Phys. J. **C4** (1998) 623.

[89] [DELPHI Coll.], J. Abdallah et al., *b-tagging in DELPHI at LEP,* CERN-EP 2002-089, Submitted to Eur. Phys. J. C.

[90] G. Borisov, *Combined b-tagging,* DELPHI 97-94 PHYS 716.

[91] I. van Vulpen, *Measurement of Z boson pair production and a search for the Higgs boson in* e^+ e^- *collisions at LEP,* Ph.D. thesis, University of Amsterdam, 2002.

[92] T. Csörgö, *Particle interferometry, binary sources and oscillations in two-particle correlations,* hep-ph/0011320.

[93] G. D'Agostini, Nucl. Instr. and Meth. **A346** (1994) 306.

[94] C. Peterson, T. Rognvaldsson and L. Lonnblad, Comp. Phys. Comm. **81** (1994) 185.

[95] DELPHI Coll., P. Abreu et al., Phys. Lett. **B479** (2000) 89.

[96] G.C. Fox and S. Wolfram, Phys. Rev. Lett. **41** (1978) 1581.

[97] J. Schwindling, B. Mansouié and O. Couet,
MLPFIT, http://home.cern.ch/schwing/MLPfit.html.